Seismo-volcanic source mechanisms in hydrothermal systems

Dinko Šindija

Submitted in accordance with the requirements for the degree of Doctor of Philosophy

The University of Leeds
School of Earth and Environment

February 2022

The candidate confirms that the work submitted is his own, except where work which has formed a pert of jointly authored publication has been included, and that appropriate credit has been given where reference has been made to the work of others.

In Chapter 3, the moment tensor inversion part is part of a publication published under the title "The complex, static displacement of a very long period seismic signal observed at Soufrière Hills volcano, Montserrat, WI" in Journal of Volcanology and Geothermal Research (413) as jointly-authored publication by Dinko Sindija, Jurgen Neuberg, and Patrick Smith. In the jointly-authored publication I processed the data, performed the restitution process, created the synthetic 2-step function that models the resolved displacement seismograms. I performed the moment tensor inversion, calculated the Green's functions, analysed the results, wrote the manuscript and created all of the figures (except Figure 9 as mentioned in the text). Jurgen Neuberg provided comments and suggestions which improved the analysis and manuscript. Patrick Smith procured the original data and has given comments on the early versions of the manuscript.

Acknowledgements

First and foremost, I would like to thank my supervisor Jürgen Neuberg for the guidance throughout my research, constructive comments, great relationship, and especially, always being available for meetings during the stressful COVID-19 time when I moved back to Croatia and worked on my PhD remotely. It's been an honour and a pleasure to work with him for all these years, I've learned so much and I hope our research journey does not stop here. Thank you Locko.

Secondly, thanks to my fellow PGR colleagues for making my PhD experience in Leeds great. Special thanks to Rodrigo Contreras Arratia for great and inspiring discussions about (volcano) seismology. Thanks Emma Pearce for all your questions. My PhD days would've been much more boring if it weren't for them.

Thanks to all the staff at the Institute of Geophysics and Tectonics for all the interesting discussions and creating encouraging environment.

Thanks to everyone who attended IGT Beers as you made Fridays better and finally, special thanks to the BFG group.

Contents

List of Figures

List of Tables

Abstract

The observation of a unique very long period (VLP) seismic signal on 23 March 2012 at Soufrière Hills volcano, Montserrat triggered this research. This event, observed on a sparse seismic network, showed the limitations of routine processing steps to estimate correct source location and source mechanism. Firstly, it shows the absolute necessity to perform a proper restitution process where one has to consider spectral components of the lowest possible signal frequencies, as the interpretation of the ground displacement, and therefore, the deformation at the source changes drastically, in this case, from oscillatory behaviour to a static displacement.

Further, it emphasises the often neglected influence of a seismic network configuration on our ability to correctly resolve the source mechanism when performing moment tensor inversion. Using numerical tests, it is shown that the moment tensor inversions using a low number of stations with poor azimuthal coverage can still produce an acceptable waveform fit at the surface, however, the time-histories of source components are not resolved. Volcano observatories can use this approach to improve their monitoring capabilities.

In contrast to the Montserrat event, the VLP signals observed in a hydrothermal environment at Whakaari, New Zealand show an oscillatory waveform entirely produced by the source. Two source mechanisms are investigated: the effect of poroelastic wave propagation and a coupled fluid-solid system. By testing these two hypotheses we gain an interesting insight in how different characteristics of poroelastic media affect seismic waves in the frequency band typical in volcano seismology.

Chapter 1

Introduction

Volcanogenic seismic signals cover a broad frequency range and fall into three main categories; Volcano-Tectonic (VT) earthquakes, Low-frequency (LF) events, and Very-Long Period (VLP) events. Their interpretation and modelling are at the core of any attempt to forecast volcanic eruptions. Volcano-tectonic (VT)

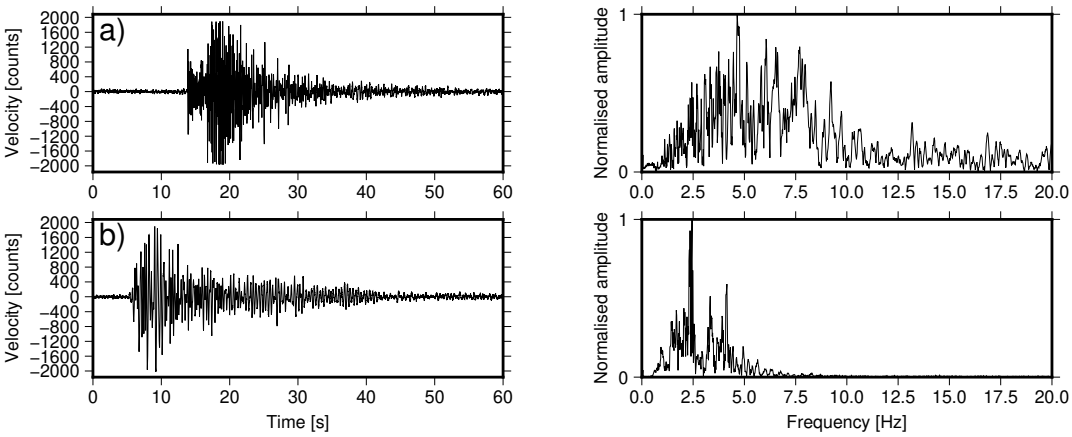

Figure 1.1. VT and LF events and their amplitude spectra. a) VT earthquakes exhibit a clear P- and S-wave onsets and have frequency content of 1-20 Hz. b) LF events have a spectral range between 0.2 and 10 Hz.

earthquakes (Figure 1.1a) have the same source mechanism as tectonic earthquakes. They are generated by the brittle failure of rocks at a fault plane due to the stress changes of magmatic emplacement or due to stress changes as a result of water-magma interaction in hydrothermal systems (Neuberg, 2021). They have similar waveform characteristics as tectonic earthquakes: clear P- and S-wave onsets and a frequency content of 1-20 Hz. The hypocentre locations of the VT earthquakes indicate changes in the volcanic system rather than

inside the magma chamber itself as they map the emplacement or withdrawal of fresh magma (Neuberg, 2021). Due to their frequency content, they are also sometimes referred to as High-Frequency (HF) events.

A pivotal moment in modern volcano seismology was the discovery of Low-frequency (LF) earthquakes (Figure 1.1b) as they have been successfully used in forecasting volcanic eruptions (Chouet, 1996a). LF earthquakes have a spectral range between 0.2 and 10 Hz, with end members of the continuum being Long-Period (LP) events and hybrid events, which are similar to LP events but have additional high frequency content (Neuberg, 2021). Their source processes differ significantly from VTs. LF events originate at the boundary between magmatic fluid and solid surrounding rock (e.g. Chouet, 1988; Neuberg et al., 2000). What is recorded at the surface is the small part of the seismic energy that escapes the conduit and propagates through solid medium, while most of the seismic energy is trapped in the fluid-filled conduit and resonates within (Neuberg et al., 2000). These seismic waves are dispersive and it is that property that describes their low-frequency content (Ferrazzini and Aki, 1987). Modelling of LF events is usually done in two ways; either the LF events are modelled as abrupt pressure changes in resonating cracks of only few centimetres width (Chouet, 1996a) or as a resonating section of the conduit of approximate size of a few tens of meters width and up to hundred meters length, where the properties of magma are dependent on depth and time (Neuberg et al., 2000). However, using the very-high-resolution seismic data from three different volcanoes - Mount Etna in Italy, Turrialba Volcano in Costa Rica and Ubinas Volcano in Peru, Bean et al. (2014) show how LP swarms can be caused by slow, quasi-brittle low stress-drop failure driven by short-lived upper-edifice deformation. The observations of LF earthquakes usually include these characteristics (Neuberg, 2021): (a) they occur in swarms, (b) their waveforms are very similar, (c) their occurrence can be highly regular, (d) the LF swarms can merge into continuous tremor. Major dome collapses and other eruptive phases are preceded by LF swarms (Miller et al., 1998), however existence of LF swarms does not guarantee a dome collapse or eruption (Neuberg, 2021).

1.1 Very-long period (VLP) seismic signals

The deployment and widespread use of broadband seismic networks in the 1990s made studies of very-long period (VLP) signals possible (Kawakatsu et al., 1992; Neuberg et al., 1994) and this thesis mainly focuses on them. VLP signals, whose periods range from several seconds to several minutes, have been observed on almost every type of volcano around the world (Chouet and Matoza, 2013a, Table 1.1). The studies of VLP seismicity have resulted, in this relatively short period of time, in great comprehension of the shallow magma conduit geometry, of the way magma moves through shallow volcanic systems, and the interaction between magma and magmatic gasses and the host rock (Waite, 2014).

Unlike LP signals, which are generally interpreted as a resonance inside the fluid-filled conduit, VLP source processes are usually attributed to fluid-rock interactions such as mass movement of volcanic fluids (e.g. Chouet and Dawson, 2011) that generate abrupt pressure changes inside the volcanic edifice. As VLPs have been observed prior to caldera collapse (Kumagai et al., 2001a; Michon et al., 2009) and prior to phreatic eruptions (Kawakatsu et al., 2000; Jolly et al., 2017) the need to study them is of great importance for understanding the underlying physical processes and estimate hazard.

The description of types of VLP sources is usually organised by fluid type and volcano environment they are observed in. This is because the models of VLP sources related to the fluid viscosity which depends on magma composition and temperature.

In the case of low-viscosity magma systems, such as Stromboli volcano, Italy and Kilauea Volcano, Hawaii, VLP seismicity is linked to the unsteady movement of magma and gasses through the conduits. In such systems, gas bubbles can ascend through the magma more buoyantly, thus making the eruptions less violent compared to more viscous volcano systems which are capable of trapping bubbles at higher pressures (Waite, 2014). Two main processes of bubble growth are coalescence of smaller bubbles and diffusion of volatiles out of solution. Another cause of bubble growth is the pressure difference between shallow and deeper depths. Thus, under specific conditions bubble diameter can become as wide as the conduit and in combination with a large gas volume it can occupy an elongated region within the conduit (Waite, 2014).

Table 1.1. List of volcanoes where VLPs have been observed

Country	Volcano	Studies
Japan	Sakurajima	Kawakatsu et al. (1992, 1994); Uhira and Takeo (1994)
	Unzen	Uhira et al. (1994)
	Aso	Kaneshima et al. (1996); Legrand et al. (2000); Kawakatsu et al. (2000)
	Satsuma-Iwojima	Ohminato and Ereditato (1997); Ohminato (2006a)
	Iwate	Nishimura et al. (2000)
	Miyakejima	Kumagai et al. (2001b); Fujita et al. (2004)
	Usu	Yamamoto et al. (2002)
	Bandai	Nishimura et al. (2003)
	Hechijo	Kumagai et al. (2003); Kumagai (2006)
	Ontake	Nakamichi et al. (2009)
	Asama	Ohminato et al. (2006a); Kazahaya et al. (2011); Maeda and Takeo (2011)
Indonesia	Merapi	Hidayat et al. (2002)
New Zealand	White Island/Whakaari	Jolly et al. (2017); Caudron et al. (2018); Jolly et al. (2018)
Italy	Stromboli	Neuberg et al. (1994); Neuberg and Luckett (1996a); Auger et al. (2006)
Hawaii (U.S.)	Kilauea	Dawson et al. (2010); Chouet et al. (2010); Dawson and Chouet (2014)
California (U.S.)	Mammoth Mountain	Hill et al. (2002)
Washington (U.S.)	Mt. St Helens	Waite et al. (2008)
Alaska (U.S.)	Okmok	Haney (2010)
Antarctica	Erebus	Rowe et al. (1998); Aster et al. (2008)
Mexico	Popocatepetl	Chouet et al. (2005)
Guatemala	Santiaguito	Sanderson et al. (2010)
Montserrat	Soufrière Hills	Green and Neuberg (2005); Sindija et al. (2021)

As this gas slug ascends, the surrounding magma must descend around it. Where the conduit changes diameter and/or orientation the centre of mass suddenly accelerates and these accelerations can cause VLP seismicity. James et al. (2006) created a laboratory experiment which investigates the ascent of a gas slug through a conduit with changes in its diameter. They show that the gas slug ascends slowly as it goes through the lower parts of the conduit due to the gradual decrease in pressure of the overlying fluid. As the gas slug enters the upper, wider, part of the conduit, it rapidly expands and accelerates. The acceleration of the slug does not act as a significant force as the mass of the gas slug is low. However the acceleration of the slug does require a downward acceleration of the surrounding fluid and it has a large enough mass to produce a strong enough force which can couple to the conduit at the location of the change in diameter (Waite, 2014). The pressure change at this location can act as a source for the VLP signal and is often interpreted as such for VLP events in low-viscosity systems. This problem is revisited by O'Brien and Bean (2008) where they used numerical modelling of multi-phase fluid dynamics and the associated elastodynamic waves to also show how gas slug ascent can be responsible for producing VLP signals. Chouet et al. (2008) for Stromboli, Chouet et al. (2010) for Kilauea, and Aster et al. (2008) for Erebus volcano, all associate VLP seismicity prior/during strombolian style eruptions to be due to the inflation and deflation of crack-like portions of the conduit to accommodate the ascents of a gas slug.

In high-viscosity volcanoes, VLP source mechanisms are unlikely to involve gas slug movement as magma is too viscous to allow gas slug ascent. The usual source mechanism of VLP signals in this environment is related to crack-like and pipe-like geometries representing changes in conduit shape, however the inflation or deflation mechanisms of the source volume are not linked to gas slugs, rather, the deflation may be related with the explosion and the eruption of material from the conduit. Examples of such environment include Potocatépetl Volcano, Mexico (Chouet et al., 2005), Augustine Volcano, Alaska (Dawson et al., 2011), and Soufrière Hills volcano, Montserrat. Chouet et al. (2005) interpret the VLP source time histories at Potocatépetl as a source process that begins with inflation (pressurisation) which is then followed by 2-3 cycles of deflation-reinflation (depressurisation-repressurisation) within a time interval of 3–5 min. The source deflation is interpreted as an opening of a crack with

addition of gas escape which causes a pressure drop and acts as a source of the VLP signal. The pressure recovery in the source region is interpreted as the influx of new magma and gas exsolution. Similarly, Dawson et al. (2011) interpret the source process of VLP signals at Augustine as inflation-deflation-reinflation of the sill over a period of 1 minute. They suggest that the inferred pressure recovery can be explained by the same model of diffusive bubble growth as at Potocatépetl.

VLP signals associated with hydrothermal processes have been observed and analysed on several volcanoes, among others: White Island volcano, New Zealand (Jolly et al., 2017); Aso volcano, Japan (Kawakatsu et al., 2000); Satsuma-Iwojima volcano, Japan (Ohminato, 2006b); Mayon Volcano, Philippines (Maeda et al., 2015). For Aso volcano, Kawakatsu et al. (2000) interpret the VLPs associated with the phreatic eruption in 1994 as a gradual inflation of the water-filled cracks and the aquifer which occurs due to heat flow from a magma chamber below. Additionally, they observe the VLPs preceding eruptions by a few minutes which they interpret as a potential case for issuing immediate warnings for phreatic eruptions. Ohminato (2006b) analyses VLPs recorded at the Satsuma-Iwojima volcano, modelling the driving part of the source as a sudden vaporisation of water in a water-filled pocket which is supplied from a nearby aquifer through low permeability bedrock. The heating from the magma or high temperature gas causes the superheated water in the pocket to vaporise causing a pressure jump observed as the VLP signal.
Maeda et al. (2015) analyse a VLP signal observed during a phreatic explosion at Mayon Volcano, Philippines. They attribute their waveform inversion solutions to the inflation of the crack, while boiling the underwater, and deflation as a discharge of the water vapour. The aforementioned studies describe the events as a sudden vaporisation of water-filled cracks caused by heat flow from the underlying magma body, however, they all picture a pure water-water system.

1.2 Study sites

1.2.1 Soufrière Hills volcano - high-viscosity volcanic system

Data for the first study site come from Soufrière Hills volcano (SHV). SHV is situated on the island of Montserrat, West Indies. The island itself is part of the 800 km-long Lesser Antilles volcanic arc and is located at the northern part of the volcanic arc. This volcanic arc is a result of the subduction of the North American plate beneath the Caribbean plate at the rate of $\sim$ 2cm/year (Smith, 2015). It is an andesitic volcano located on the southern part of the island. SHV is the youngest and only active volcanic system out of three volcanic complexes at the island of Montserrat, the other two being Silver Hills (c. 2.6 - 1.2 Ma) and Centre Hills (c. 950-550 ka) (Smith, 2015). It has been in state of activity since 1995 and the eruption has consisted of five extrusive phases with quiet periods between them (Figure 1.2). The current eruption started on 18 July 1995 after a period of 3 years of increased seismic activity (Smith, 2015). During each of the five phases, a major dome or sector collapse event has occurred, notably in December 1997, March 2000, July 2003, May 2006, and February 2010 (Smith, 2015). VLP seismicity at SHV has only been observed three times; in 2004 (Green and Neuberg, 2005), 2012 (Sindija et al., 2021), and 2014. Green and Neuberg (2005) interpret the 2004 VLP event as a collapse of a gas-charged region within the upper edifice. The 2012 VLP is described in Chapter 3, while the 2014 event has not been studied in detail and has only been observed on few stations of the local network.

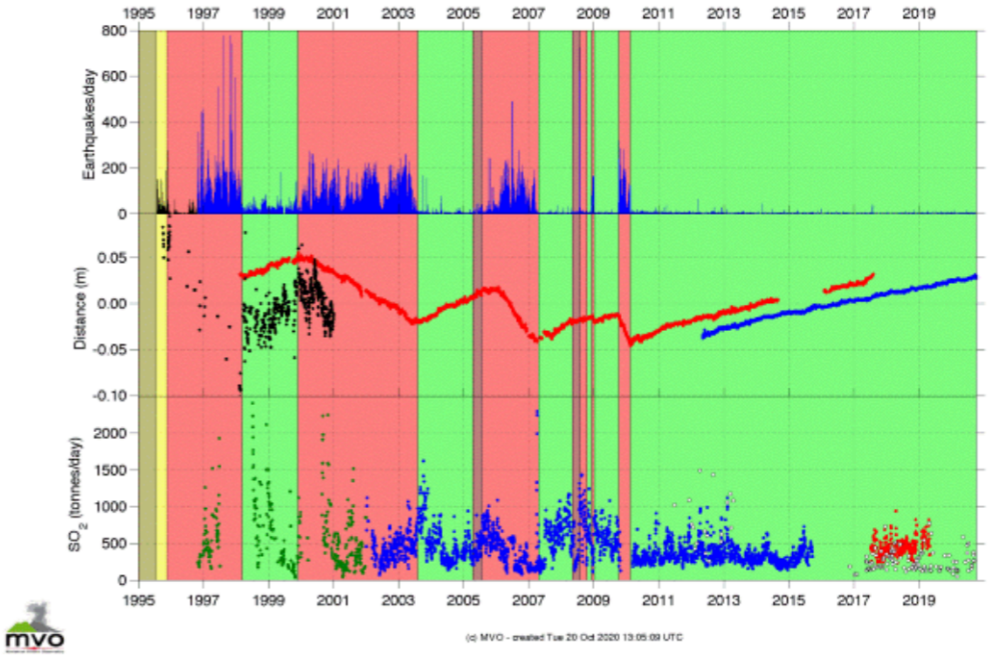

Figure 1.2. Monitoring data from Montserrat since the start of the eruption. (top) number of events per day; (middle) vertical displacement for HARR station (black) and horizontal ground motion at MVO1 (red) and GERD (blue) stations relative to the dome centre; (bottom) SO_2 outgassing in tons per day. Adopted from Stinton et al. (2020).

1.2.2 Whakaari (White Island) - a hydrothermal volcanic system

Whakaari is an andesitic cone volcano located 48 km north of New Zealand's North Island. The active horseshoe-shaped crater contains a crater lake, a large lake of boiling acidic waters which varies in volume due to meteorological conditions and changing levels of hydrothermal activity (Heap et al., 2017). Whakaari is one of New Zealand's most active volcanoes and it has been a popular tourist destination. Since broadband seismic monitoring has been established in 2007 it experienced two unrest episodes - in 2011–2016 and in 2019. In this period it has produced seven hazardous eruptions (Park et al., 2020). The most recent one, in December 2019, resulted in 21 fatalities. As it is a hydrothermal environment, most common eruptions are phreatic and phreatomagmatic. These types of eruptions are often accompanied and/or preceded by VLP signals. Therefore, there is a great need for continuous monitoring and research

on Whakaari volcanic activity.

The location of the observed VLP events has been well established. Jolly et al. (2017) studied a swarm of mixed frequency events including VTs, LPs, and VLPs during the 19-21 August 2011 eruption observed on a temporary seismic array. They placed the origin of VLPs at 0.8-1.5 km depth, while the associated high-frequency (VT) and LP events were reported to occur at shallower depths ($<$ 1 km). They interpret this series of events as a migration of fluid into the shallower parts of the hydrothermal system. Their results suggest a most likely source mechanism for the VLPs to be an opening of a tensile crack with significant shear movement in the dipping direction. The 2013 eruption episode was studied by Caudron et al. (2018) where they located the VLP sources at similar depths as the 2011 episode, at 0.8-1 km depth. Further, study by Jolly et al. (2018) that also looked at the 2016 data put the VLP source at 0.8-1 km depth. Park et al. (2020) gathered all the studies before and showed that there are two families of VLPs observed - F1 type (e.g. Caudron et al., 2018; Jolly et al., 2018) and F2 type (e.g. Jolly et al., 2017). The F1 family has been observed throughout the studied period (2007-2019) while the F2 family bas been closely to the onset of volcanic unrest. However, high amplitude F1 type VLPs have been observed prior to phreatic eruptions in 2013 (Caudron et al., 2018) and 2016 (Jolly et al., 2018). The waveform difference between the two families is seen in Figure 1.3 with the main difference being the opposite polarity of the first motion and an additional oscillation for F2 type.

Previous models explain the oscillatory motion and the opposite polarities as the excitation of the same oriented crack but with an opposite slip direction and volumetric change (Park et al., 2020). However, there could be a different explanation for the oscillatory waveforms, other than inflation/deflation source mechanism, which is explored in Chapter 4.

1.3 Restitution of the VLP ground displacement

The major advantage VLP signals offer is direct insight in the deformation of the source process. This fact was recognised and studied by Legrand et al. (2000, 2005). As VLP signals have wavelengths of tens to hundreds of km, it places most seismic stations of a volcanic monitoring network in the so-called

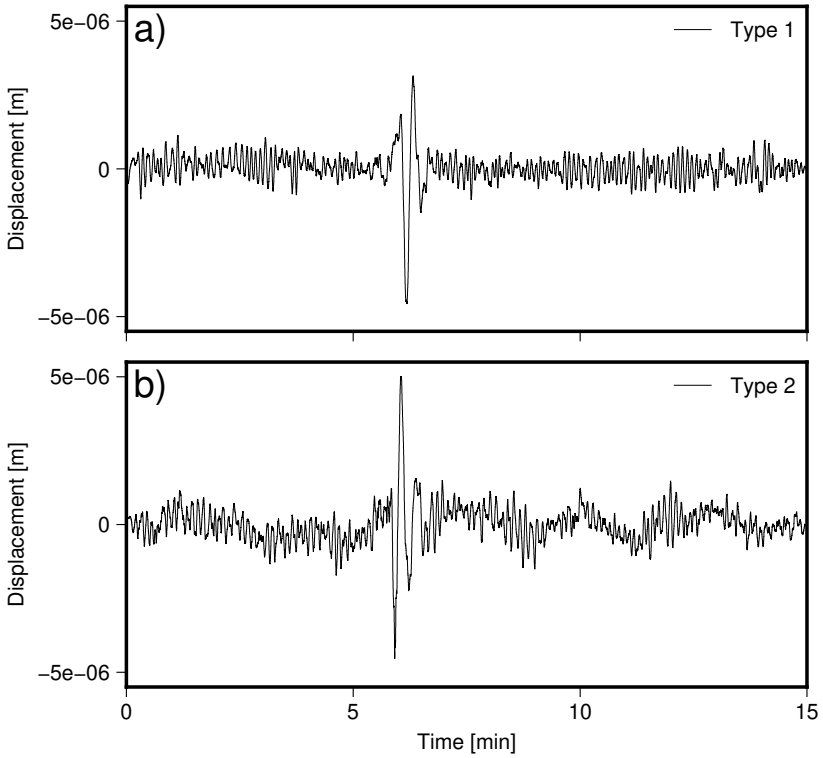

Figure 1.3. The displacement seismograms showing examples for two family types of VLPs observed on Whakaari: (a) Type 1 observed April 28th, 2016 on WIZ station and (b) Type 2 observed on January 23rd, 2018 also on WIZ station. The displacement seismograms were restituted including spectral components up to 1000 s. The event trigger times were taken from Additional file 1 from Park et al. (2020).

near-field, i.e. within one wavelength from the source. In the near-field, the seismic displacement at the surface is directly proportional to the deformation at the source. Therefore, it is essential to retrieve the exact source time history in addition to amplitude and moment tensor components to adequately model the deformation process. Often, the first step in searching for a VLP signal is analysing the amplitude spectrum of the recorded velocity seismogram. For a VLP signal observed on Montserrat, we see a broad peak relating to the VLP signal around 0.01 Hz (Figure 1.4a). However, this VLP signal has been distorted by the instrument response as the low frequencies in the original signal have been cut-off. Hence, when analysing VLP signals that have a frequency content outside the flat-band of the instrument response, one needs to keep in mind the original signal could contain seismic energy at much longer periods than displayed in the amplitude spectrum of the recorded signal. Figure 1.4b shows such an example where a signal with dominant period of 500 s is observed

at a station with a 120 second instrument.

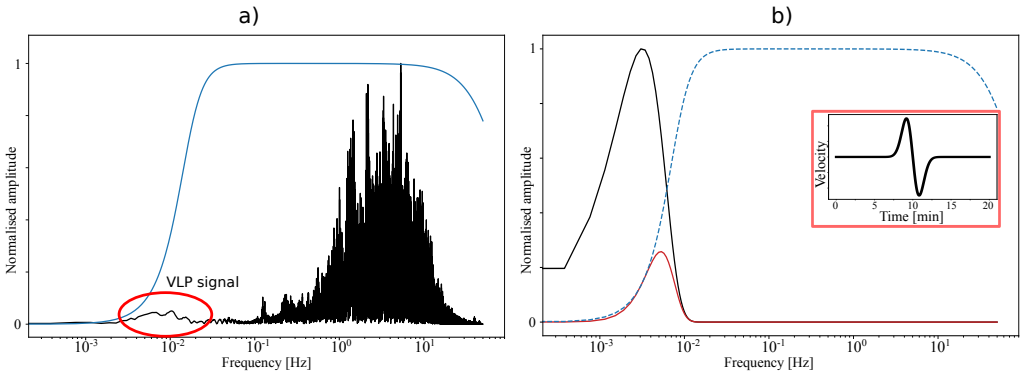

Figure 1.4. a) Amplitude spectrum of the vertical component velocity seismogram recorded at MBWW station on March 23, 2012 showing a broad VLP signal with dominant frequency of 0.01 Hz with superimposed transfer function of 120s-instrument at that station. b) Example of how the instrument response impacts the observed amplitude spectrum. I produced a synthetic velocity seismogram with period of 500 seconds (red box), calculated the amplitude spectrum (black) and then simulated the effect of the 120s-instrument response on the input signal (red).

To account for the shape of the instrument response and to make sure that the restitution of ground displacement considers the whole energy content of the ground motion we have to carry out certain processing steps. These processing steps go beyond the usual "instrument removal" applied as a routine by seismic processing packages, which considers the frequency range in the pass-band of the instrument only. Examples of VLPs observed on Stromboli volcano from two different studies show how these processing steps can influence our interpretation of the source dynamics. Figure 1.5 shows the restitution of vertical ground displacement of a VLP signal observed during a Strombolian eruption (Neuberg and Luckett, 1996b; Neuberg, 2006) using a 120 s instrument. For the process of restitution different high-pass filters are applied with cut-off frequencies of 0.004 Hz (250 s), 0.002 Hz (500 s), and 0.001 Hz (1000 s) to the velocity trace after which the instrument response (including the digitiser gain) is removed and the trace is integrated to obtain the displacement seismogram. The application of a high-pass filter with a cut-off frequency lower than the flat-band of the instrument response (Neuberg and Luckett, 1996b; Caudron et al., 2018) helps us recover the low frequency information while suppressing the amplification of the long period, environmental and electronic noise during the integration. Choosing the appropriate high pass filter is crucial, as

the interpretation of the obtained displacement seismograms changes. Chouet et al. (2003) observed two types of VLP signals (Type 1 and Type 2, Figure 1.6) during the Strombolian eruptions using 60 s instruments. They apply a bandpass filter between 2 and 30 s to the velocity trace after which the instrument response is removed and they interpret the Type 2 events as inflation which is then followed by deflation and re-inflation. Comparing the ground displacement seismograms shown in Figure 1.5 and Figure 1.6 we can see that if we don't include the lowest spectral components of the signal, our interpretation of the source behaviour changes from inflation-deflation (Figure 1.5d) to a more oscillatory behaviour (Figure 1.6b). Unfortunately, there is no general recipe or criteria how to define the lowest cut-off frequency as this process is highly dependent on the data quality. In general, the vertical components are less affected by low frequency noise than the horizontal components. We also have to assume that there is no seismic energy or a static offset at even lower frequencies.

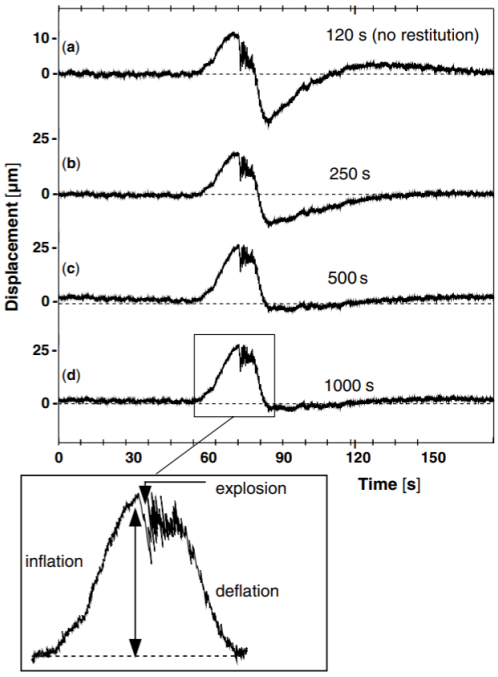

Figure 1.5. Restitution of ground displacement for a VLP observed at Stromboli volcano. (a) Displacement seismogram (without the instrument response removed) (b), (c), and (d) Displacement seismograms after correcting for the instrument response and considering spectral components to a period of 250, 500, and 1000 s respectively. Adopted from Neuberg (2006).

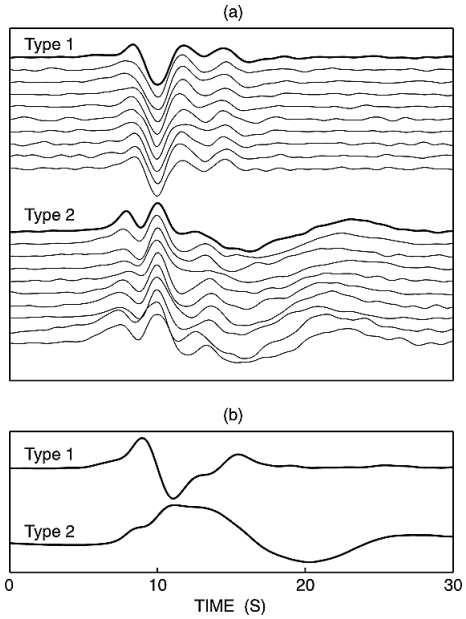

Figure 1.6. (a) Normalised east component of a velocity seismograms for Type 1 and Type 2 VLP events filtered between 2 and 20 s (Type 1) and 2 and 30 s (Type 2). (b) Normalised east component displacement seismograms for the two types of VLP signals observed. Adopted from Chouet et al. (2003).

In this thesis I focus on two VLP signals observed in two different volcanic environments; one on Soufrière Hills volcano, Montserrat and the other on White Island volcano, New Zealand, a known hydrothermal volcanic system (Section 1.2). By following the same restitution process described above, i.e. applying different high pass filters and then removing the instrument response, we can see that the description for the two VLP events is quite different. For the VLP signal from Montserrat (Figure 1.7) which was recorded using a 120s Güralp-3T broadband instrument, the application of different high pass filters changes the interpretation of the source behaviour. Figure 1.7a shows a 16 minute long record of the VT swarm observed on 23 March 2012 at Soufrière Hills volcano, Montserrat. The velocity seismogram is dominated by high frequency VT earthquakes. However, if we integrate the seismogram (Figure 1.7b) the VLP signal becomes obvious. The displacement seismogram in trace (c) shows an apparent inflation (motion up) followed by a deflation (motion down) below the pre-signal level. This interpretation dramatically changes by including longer periods in traces (d) and (e). The ground displacement shown now in trace (e) could be described as a step-like inflation. The fact that a further extension to a lower frequency range does not change the waveform indicates

that the trace now represents the "true" ground displacement of the process. In this case it gives us the "true" amplitude of the displacement as well, which can be directly read from the displacement seismogram (Figure 1.7f).

However, for the VLP signal from White Island volcano, recorded using a Güralp 3ESP seismometer with a corner period of 60 s, the restitution process does not change the oscillatory nature of the original waveform (Figure 1.8). Therefore, after we are sure that the oscillatory waveform is not due to the effect the instrument response has on the very-long period signals, we can interpret the resulting signal as the deformation signature of the source process.

VLP signals observed on Montserrat and Whakaari are studied in Chapter 3 and Chapter 4, respectively. While we can interpret the step-like displacement at Montserrat (Figure 1.7f) as step-like inflation at the source we ask ourselves whether VLP displacements at Whakaari (Figure 1.8e) can be caused by a similar source displacement and the resulting oscillatory waveforms are due to poroelastic medium. I examine this problem through modelling wave propagation in porous media and fluid-solid interactions.

1.4 Moment tensor inversion

The principal technique for estimating seismic source mechanisms in both "tectonic" and "volcanic" settings is the moment tensor inversion (MTI). The moment tensor (MT) is a general, mathematical representation of equivalent body forces of a seismic source (Aki and Richards, 2002). It is composed of nine force couples, where each couple relates to one set of opposing forces (Figure 1.9). Using MTI, we invert the waveforms of the signal (in our case the restituted displacement seismograms) and solve for the amplitudes and the time histories of the moment tensor (or moment-rate tensor if we used velocity waveforms). What differentiates the MTI in volcano seismology from inversions in the "tectonic" seismology is that in the volcanic environments we have to include additional three single force components on top of the nine moment tensor components (Ohminato et al., 1998). Although moment-tensor inversions are our best way into "seeing" the source mechanisms, there are still unknowns and uncertainties that come with it. Contreras-Arratia and Neuberg (2019) show the difference between MTI results when the assumption of a planar fault for seismic sources deviates to a more complex geometry like a dyke fault or a ring

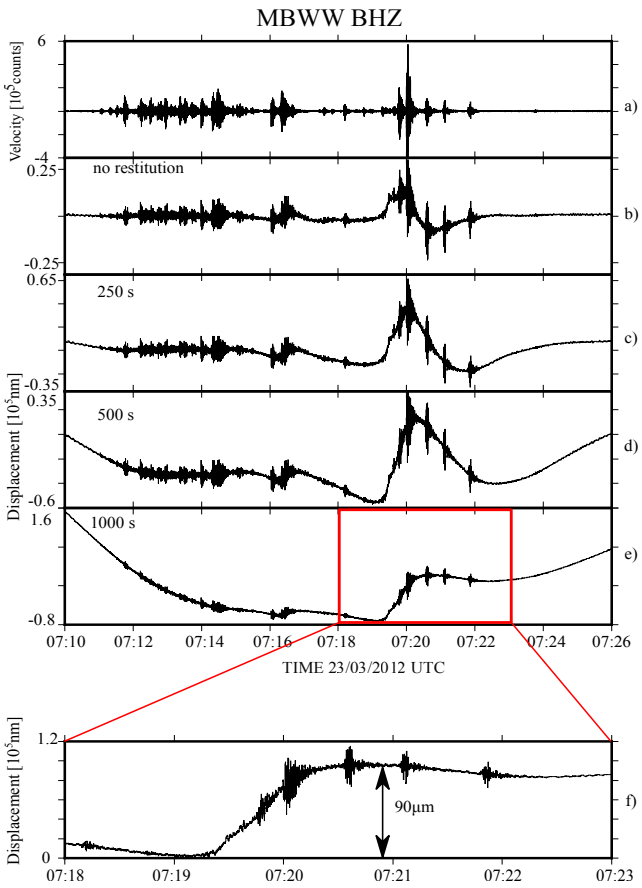

Figure 1.7. Restitution of the vertical component ground displacement at MBWW station. (a) Uncorrected velocity seismogram. (b) Integrated (without restitution) velocity seismogram which identifies the VLP signal (c) to (e) Displacement seismograms after correcting for the instrument response and considering spectral components to a period of 250, 500 and 1000 s respectively. (f) Five minute long time window showing true ground displacement.

fault. Bean et al. (2008) and Trovato et al. (2016) examined the influence of velocity models used in moment-tensor inversions, where they compared the results of sources in a homogeneous halfspace and models with low-velocity surface layers and models with velocity gradients. Also, topography and topographic scattering produce effects which lead to uncertainties in the source solutions (e.g. Neuberg and Pointer, 2000; O'Brien and Bean, 2009).

To describe displacement field $\boldsymbol{u}$ at the position $\boldsymbol{x}$ on the surface due to the point source represented by moment tensor $\boldsymbol{M}$ and a single force $\boldsymbol{F}$ at the

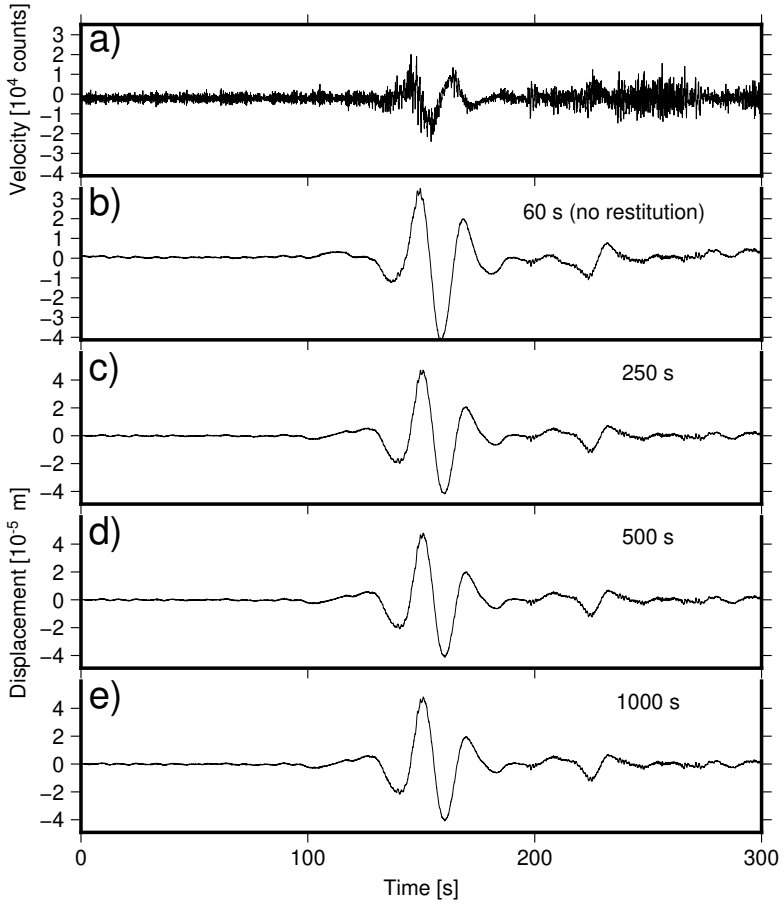

Figure 1.8. Restitution of the vertical component ground displacement of a VLP signal from White Island. (a) Raw velocity seismogram (b) Displacement trace without removal of the instrument response (c) to (e) Displacement seismograms after correcting for the instrument response and considering spectral components to a period of 250, 500 and 1000 s respectively.

position $\boldsymbol{\xi}$ we use (Chouet, 1996b):

$$u_n(\boldsymbol{x},t) = M_{pq}(\boldsymbol{\xi},t) * G_{np,q}(\boldsymbol{\xi},\boldsymbol{x},t) + F_p(\boldsymbol{\xi},t) * G_{np}(\boldsymbol{\xi},\boldsymbol{x},t) \qquad (1.1)$$

where $u_n(\boldsymbol{x},t)$ is the n-th component of the displacement at the position $\boldsymbol{x}$ on the surface at the time t, $M_{pq}(t)$ is the time history of the pq-component of the moment tensor $\boldsymbol{M}$ at the source position $\boldsymbol{\xi}$, F_p is the time history of the force applied in p-th direction at source ($\boldsymbol{\xi}$), and $G_{np}(\boldsymbol{\xi},\boldsymbol{x},t)$ is the np component of the Green's tensor relating the n-th component of the displacement at $\boldsymbol{x}$ with the p-th component of the force applied at $\boldsymbol{\xi}$. The $,q$ notation describes spatial differentiation with respect to source coordinate ξ_q and the symbol $*$ indicates

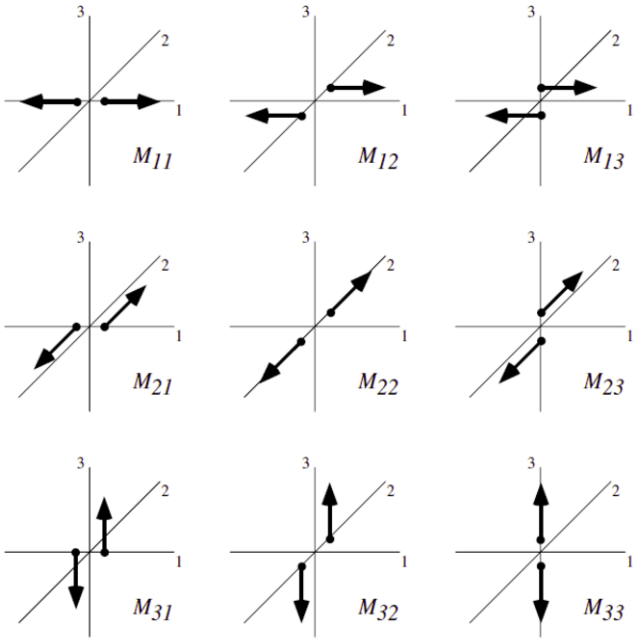

Figure 1.9. The moment tensor is composed out of nine force couples, where diagonal components are linear vector dipoles and off-diagonal are force couples with moment. Adopted from Aki and Richards (2002).

time convolution (Chouet, 1996b).

The Green's functions (GF) are used to describe the Earth's response at the station at location $\boldsymbol{x}$ and time t for a perfect impulse source excitation. To obtain the Green's functions we need either direct measurement or an estimate of the velocity and density structure of our subsurface model. The accuracy of the calculated GFs can be strongly influenced by our (poor) understanding of the propagation medium (Bean et al., 2008) which then impacts the accuracy of the moment tensor inversion. Therefore, when discussing the uncertainties in the moment tensor inversion results, Green's functions are usually discussed first. Later in this thesis, I will show how we also have to put a great emphasis on the effect the seismic network configuration has on moment tensor inversion results.

1.5 Aim and Objectives

In this thesis I aim to show how to deal with VLP signals; how to identify them, how to treat them to obtain the most information from the broadband seismometer, and how to resolve and interpret their source processes depending on the volcanic environment they are observed in, for a range of periods and network characteristics.
The main objectives of this thesis are:

- Examine how seismic network configuration affects the moment tensor inversion results.
- Study the influence the source orientation has on moment tensor inversion results.
- Show how a volcano observatory can evaluate their ability to invert moment tensors for a variety of source orientations and volumetric components in dependence on the station distribution.
- Study a VLP signal observed on Soufrière Hills volcano, Montserrat for which a proper restitution process has been applied and estimate the location and volume change using moment tensor inversion.
- Show that the oscillatory waveform of VLP signals at Whakaari is due to the source mechanism in contrast to the case of Montserrat where an oscillatory behaviour would be due to the incomplete removal of the instrument response.
- Examine the hypothesis that the oscillatory VLP waveform observed on Whakaari is due to poroelastic wave propagation.
- Examine whether a coupled fluid-solid system could explain the VLP displacements in hydrothermal systems.

1.6 Outline

After this introduction chapter, in Chapter 2 I develop and perform moment tensor inversion resolution tests to see how different source orientations relate to our ability to correctly invert for moment tensors when the station distribution is varied. In Chapter 3 I perform moment tensor inversion for the VLP event observed on Soufrière Hills volcano, Montserrat, estimating its source mechanism, location, and source volume change. In Chapter 4 focusing on VLP waveforms from White Island volcano, New Zealand, I first give an overview of Biot's theory for poro-elastic wave propagation. Then using the characteristic values for this volcanic environment I perform numerical simulations of poroelastic wave propagation to explain the observed waveforms. Further, I examine how a coupled fluid-solid system can explain the oscillatory nature of the observed waveforms. In Chapter 5 I discuss how these results help the broader volcanological community, how volcano observatories can use the moment tensor inversion resolution tests to improve their ability to invert for source parameters in times of re-deployments or seismic upgrades of their seismic network, and how using poroelastic theory rather than elastic can impact our modelling of seismo-volcanic signals.

Chapter 2

Moment tensor inversion resolution tests

2.1 Introduction

One aspect of moment-tensor inversions that has been widely neglected is the influence of the seismic network geometry. Lanza and Waite (2018) tested the ability of 16 synthetic seismic networks with the number of stations ranging from three to 40 to resolve the key components of the moment tensor. As a case study they use Pacaya volcano, Guatemala for which they computed synthetic seismograms for six input source models - (1) a dipping crack, (2) a vertical crack, (3) an isotropic source, (4) a pure composite linear vector dipole (CLVD), (5) a linear vector dipole (LVD), and (6) a double-couple (DC). In this chapter, on a case study for Soufrière Hills volcano, Montserrat, in order to estimate the influence of the seismic network configuration on the resolved moment tensor components, I perform multiple moment-tensor inversions using the existing station configuration of the Montserrat Volcano Observatory (MVO) and realistically subtracting stations to see how well can we resolve different source mechanisms during a volcanic crisis, and adding stations to enhance the azimuthal coverage and see how much our results improve. The input sources are described as vertical DCs with varying strike directions to also reveal the influence of the source orientation on the resolved moment tensor. Additionally, I also show how it is possible, depending on the station configuration, to get a good fit in the time domain, while the results for source mechanism do not converge to an unique solution. Using these moment-tensor

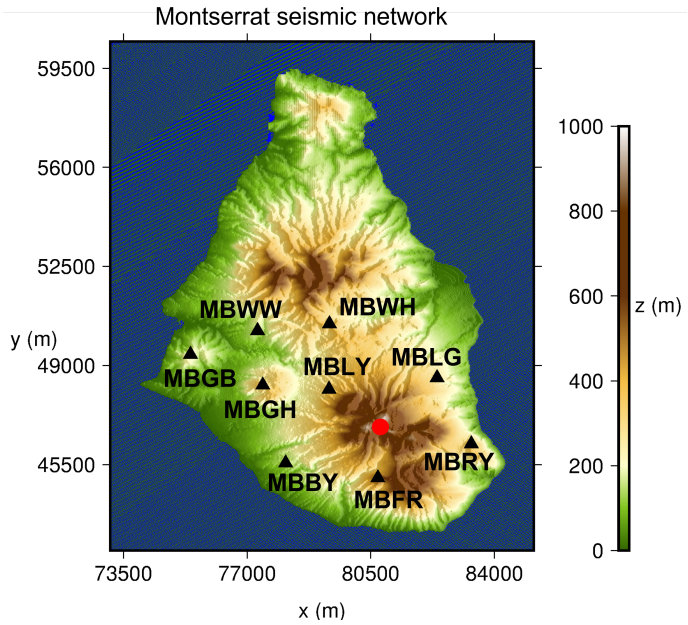

Figure 2.1. Map of Montserrat with its seismic network configuration.

resolution tests the observatories can test their existing station configuration and enhance their ability to correctly invert for moment tensors by adding a station at a certain location.

2.2 Case study

As a case study I use Soufrière Hills volcano, Montserrat. The seismic network on the island of Montserrat consists of nine stations equipped with three-component broadband seismometers (Figure 2.1). Water Works (MBWW) station, deployed by the University of Leeds, Broderick's Yard (MBBY), Windy Hill (MBWH), Fergus Ridge (MBFR), Garibaldi Hill (MBGB), St. George's Hill (MBGH), Long Ground (MBLG), Lee's Yard (MBLY), and Roche's Yard (MBRY). The 3-D topography is derived from a digital elevation map from 2003 with a resolution of 10 m. There were significant topographic changes following the large partial collapse of the lava dome on 11 February 2010, and the new DEM is used in the next chapter. For this part which is focused on synthetic tests, I use the DEM from 2003.

2.3 Numerical modelling and moment tensor inversion scheme

2.3.1 Numerical domain

The synthetic seismograms and the Green's functions, necessary for the MTI, were computed using the spectral element method software *SPECFEM3D* (Komatitsch et al., 2012). The numerical domain was $12 \times 18 \times 10$ km^3 with 400 m grid spacing, topography included, and boundary conditions set to free surface at the top of the model and absorbing boundaries on the other five surfaces. I use a homogeneous velocity model with $v_\mathrm{p} = 3500$ m/s, $v_\mathrm{s} = 2000$ m/s, and $\rho = 2600$ kg/m^3. As this study is focused on the sensitivity of moment tensor inversions to station configurations, the assumption of a homogeneous halfspace was deemed appropriate. An important aspect of using a spectral element method is creating an appropriate mesh representing our medium. To avoid numerical dispersion, an appropriate grid spacing has to be calculated. In order to do that we first have to think about the wavelength of our inspected signal:

$$\lambda_\mathrm{min} = \frac{v_\mathrm{min}}{f_\mathrm{max}}, \tag{2.1}$$

where λ_min is the minimal wavelength of our signal, v_min is the minimal velocity in our model (i.e. v_s), and f_max is the maximal frequency we will inspect. To get the desired grid spacing we then take into account the number of nodes per wavelength:

$$\mathrm{d}h = \frac{\lambda_\mathrm{min}}{n}, \tag{2.2}$$

where dh is the maximal grid spacing and n is the number of nodes per wavelength characteristic to each numerical scheme. Additionally, for the numerical scheme to be stable, the following criteria for the size of the time-step has to be satisfied:

$$\mathrm{d}t < 0.3\frac{\mathrm{d}h}{v_\mathrm{max}}, \tag{2.3}$$

where dt is the maximum time step and v_max is the maximum velocity in the medium (i.e. v_p). The factor 0.3 relates to Courant stability number for this numerical scheme (Komatitsch et al., 2012).

2.3.2 Moment tensor inversion

As this study aims to look at the influence of station configuration on the resolved source models using moment tensor inversion, I use *VOLPIS* (Volcanic Long Period Inversion for the Source, Cesca and Dahm, 2008), a Fortran based moment tensor inversion code which operates in the frequency domain. As convolution in the time domain equals multiplication in the frequency domain we can re-write equation (1.1) as:

$$u_n(\boldsymbol{x},\omega) = M_{pq}(\omega)G_{np,q}(\boldsymbol{\xi},\boldsymbol{x},\omega) + F_p(\boldsymbol{\xi},\omega)G_{np}(\boldsymbol{\xi},\boldsymbol{x},\omega) \tag{2.4}$$

Furthermore, using the abbreviations:

$$\begin{aligned} &m_1 = M_{11} \quad m_2 = M_{12} \quad m_3 = M_{13} \\ &m_4 = M_{13} \quad m_5 = M_{23} \quad m_6 = M_{33} \\ &m_7 = F_1 \quad m_8 = F_2 \quad m_9 = F_3 \end{aligned} \tag{2.5}$$

we can compact equation (2.4) into (Cesca and Dahm, 2008):

$$u_n(\omega) = m_p(\omega)G_{np}(\omega) \tag{2.6}$$

where G_{np} are now Green's functions (GFs) relating to either spatial derivatives of GFs when paired up with moment tensor components or to plain GFs when paired with single force components.
As we now have ground displacement data (deconvolved seismograms and converted into displacement) and we have obtained all GFs, which are the same length and sample rate as the displacement data, we can solve equation (2.6) for moment tensor components m_p using least squares inversion ($\boldsymbol{d} = \boldsymbol{Gm}$). The power of this inversion code is that it resolves both the time histories of the surface displacements (or velocities) and the time histories of the individual moment tensor (MT) and single force (SF) components.

2.4 Seismogram vs Source

First I tested how well we can resolve a source model using different station configurations, when the numbers of stations used in the inversion vary. The source was placed below the volcano summit at 1000 m below sea level (b.s.l.). The input source time history is described using a Gaussian with a period of 3 s. The source used for calculating synthetic displacements was a pure vertical slip with a moment magnitude (M_0) of 10^{12} Nm, dip (δ) 90°, rake (λ) 90°, and strike (ϕ) of 60°. The displacement seismograms were calculated for two scenarios - (1) when all nine stations are operational and (2) an "eruption" scenario where only 4 most distant stations north-west of the volcano are operational (MBGB, MBGH, MBWH, MBWW). We are interested in looking at both how well my resolved seismograms fit with the my forward model (*fit at the surface*) and how well does the inversion resolve the input source time history, i.e. time history of the moment tensor components (*fit at the source*). Figure 2.2 shows the results for the first scenario where all the stations are operational. As expected, the fit at both the surface (Figure 2.2a) and at the source (Figure 2.2b) are good. The only exception is station MBBY, however for these source parameters ($\phi = 60°$) this station lies on the nodal plane, which can be inferred both by looking at the map and by noticing the order of magnitude smaller displacement amplitude at that station. Things change when we look at the second scenario where only the four most distant stations are used (Figure 2.3). Surprisingly, the fit at the surface is more than acceptable, however, when we look at the fit at the source, we can see that the MT components are not resolved at all. This shows that we shouldn't trust the results from just the 'seismogram' fit as it does not guarantee the choice of the correct model for a non-unique solution.

A common methodology for finding the best solution of the moment tensor inversion is based on minimising a weighted square misfit between the observed (in my case synthetic observations) and resolved data (e.g. Ohminato et al., 1998; Chouet et al., 2003; Cesca and Dahm, 2008):

$$\text{misfit} = \left[\frac{\sum_{i=1}^{N_t} \sum_{j=1}^{N_i} (d_i(t_j) - s_i(t_j))^2}{\sum_{i=1}^{N_t} \sum_{j=1}^{N_i} (d_i(t_j))^2} \right], \tag{2.7}$$

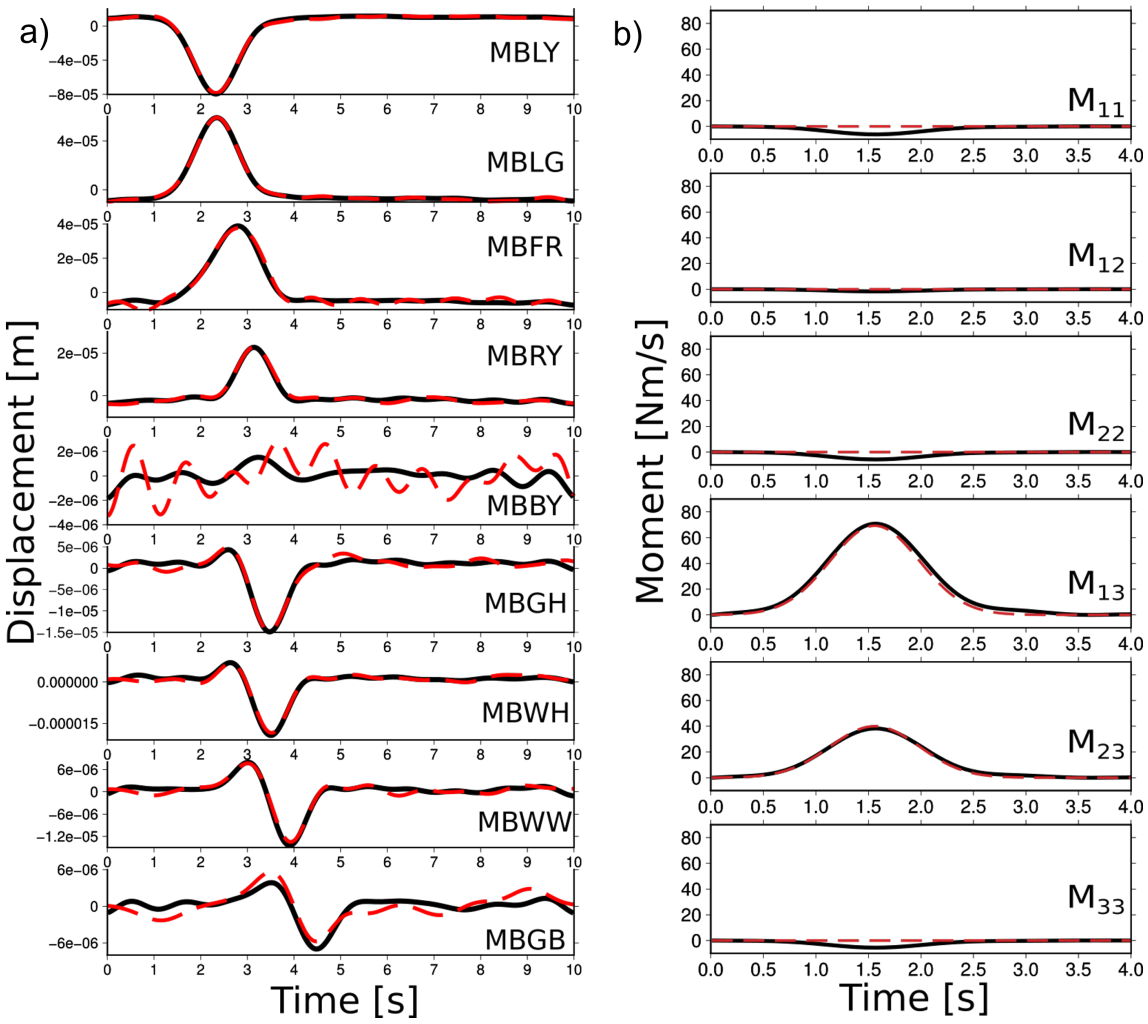

Figure 2.2. MTI using 9 station configuration showing: a) Resolved time histories of the surface displacements (dashed red) compared to the surface displacements obtained computing the forward problem (black). b) Resolved time histories for the MT components (black) compared with the time histories of the input model (dashed red).

where N_t is the number of time traces, N_i is the number of time samples for j-th trace, and $d_i(t_j)$ and $s_i(t_j)$ are the j-th samples of i-th time trace for input data and synthetic time trace respectively (Cesca and Dahm, 2008). The misfit results are dimensionless and normalised. However, because of the examples shown in this section, in subsequent tests when calculating the misfit, i.e. the goodness of fit for my results, for time traces I do not use the synthetic observations and the resolved seismograms, but the input source model time histories and the resolved source model time histories.

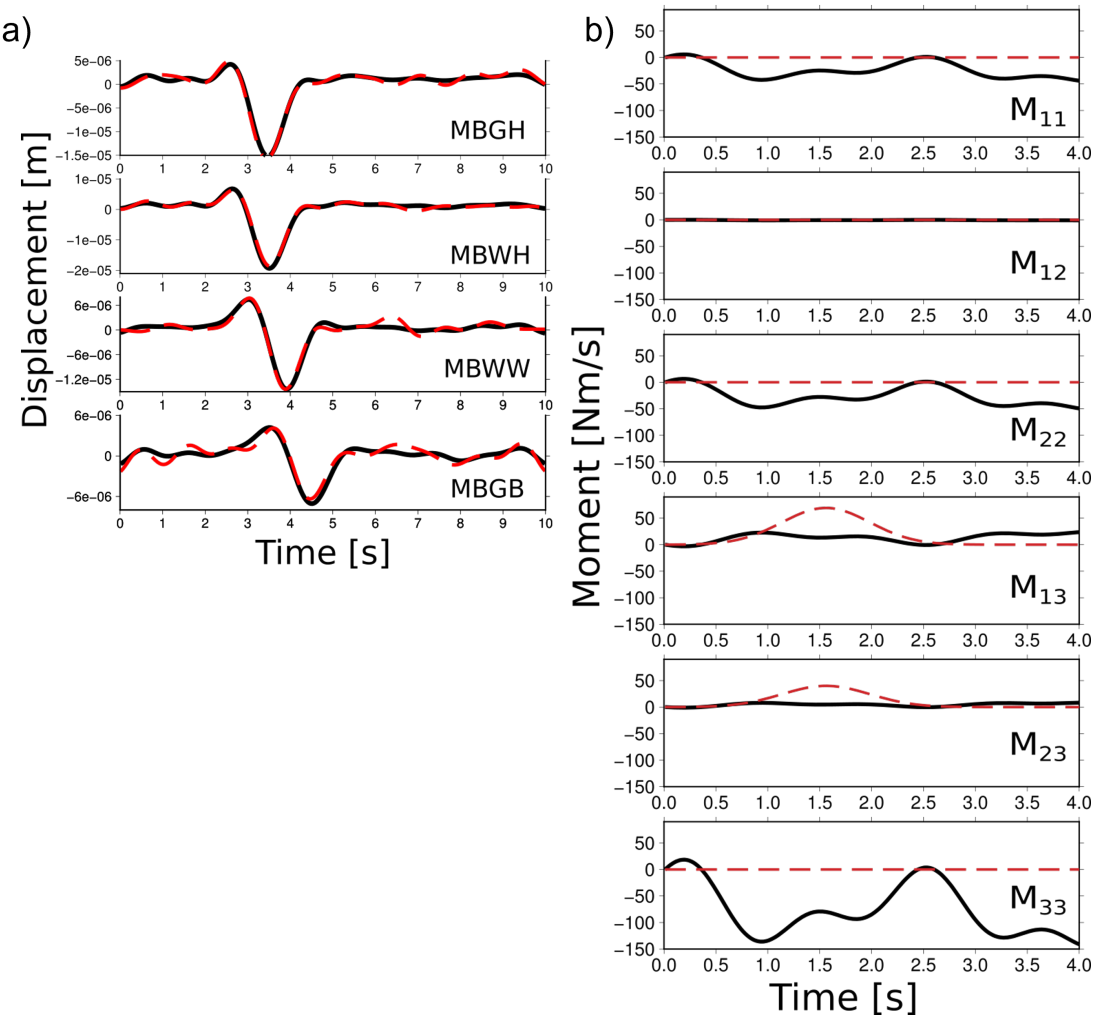

Figure 2.3. MTI using 4 station configuration showing: a) Resolved time histories of the surface displacements (dashed red) compared to the surface displacements obtained computing the forward problem (black). b) Resolved time histories for the MT components (black) compared with the time histories of the input model (dashed red).

2.5 Influence of the source orientation

For this set of synthetic tests I expand the configurations of my tests. I place the sources at three different depths; 0 m below sea level (b.s.l), 500 m below sea level, and 1000 m below sea level. The source mechanism was again a pure vertical slip DC, with $M_0 = 10^{12}$ Nm where the strike angle is varied between 0° and 180° with 15° interval. Firstly, the tests were done using the seismic network of nine stations. Figure 2.4 shows the results for resolve MT

components when the source is placed at sea level (0 m b.s.l.). Source Model 1 (Figure 2.4a) is described using dip (δ) 90°, rake (λ) 90°, and strike (ϕ) of 30°:

$$\boldsymbol{M}_{\textbf{model 1}} = \begin{bmatrix} M_{11} & M_{12} & M_{13} \\ M_{21} & M_{22} & M_{23} \\ M_{31} & M_{32} & M_{33} \end{bmatrix} = \begin{bmatrix} 0 & 0 & 0.5 \\ 0 & 0 & 0.866 \\ 0.5 & 0.866 & 0 \end{bmatrix}. \tag{2.8}$$

The calculated misfit using equation (2.7) is 0.02.

Source Model 2 (Figure 2.4b) is a vertical slip with strike 195°:

$$\boldsymbol{M}_{\textbf{model 2}} = \begin{bmatrix} M_{11} & M_{12} & M_{13} \\ M_{21} & M_{22} & M_{23} \\ M_{31} & M_{32} & M_{33} \end{bmatrix} = \begin{bmatrix} 0 & 0 & -0.2588 \\ 0 & 0 & -0.9659 \\ -0.2588 & -0.9659 & 0 \end{bmatrix}. \tag{2.9}$$

The misfit between the resolved time histories of MT components and the input MT components is 0.3. It is important to notice the "leakage" into diagonal components of the MT (M_{11}, M_{22}, M_{33} in Figure 2.4b) in the MTI results. The diagonal components are part of the isotropic part of the moment tensor and they indicate a volume change at the source.

The third example used in this comparison is Source Model 3 (Figure 2.4c) where the strike was 15°:

$$\boldsymbol{M}_{\textbf{model 3}} = \begin{bmatrix} M_{11} & M_{12} & M_{13} \\ M_{21} & M_{22} & M_{23} \\ M_{31} & M_{32} & M_{33} \end{bmatrix} = \begin{bmatrix} 0 & 0 & 0.2588 \\ 0 & 0 & 0.9659 \\ 0.2588 & 0.9659 & 0 \end{bmatrix}. \tag{2.10}$$

In this case, the misfit is 1.2 and the input model is not resolved at all. Now in the next step I colour code my results based on the calculated misfits for the whole range of modelled sources. If the misfit is below 0.1 the results are marked as green, meaning that for that we can resolve source components correctly. If it is between 0.1 and 0.8 they are coloured on a spectrum from yellow (0.1) to orange (0.8), meaning that we need to be careful with interpreting these results, and everything with a misfit above 0.8 is coloured red and those results should not be trusted.

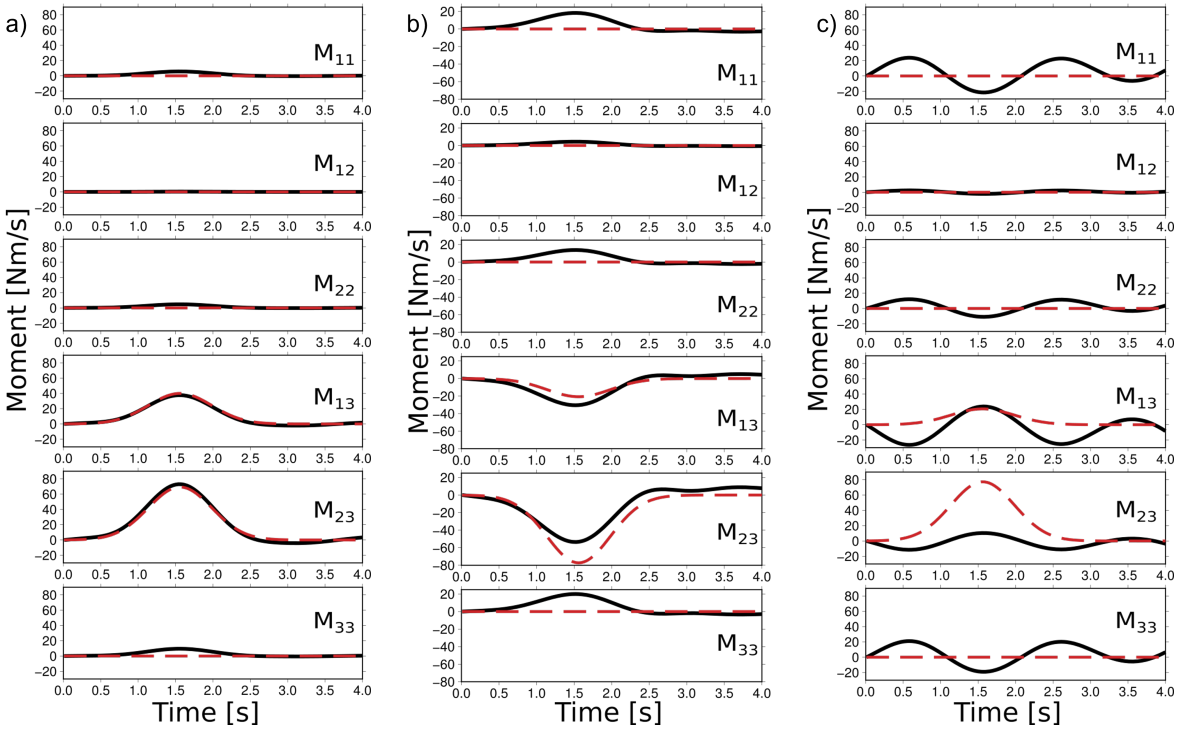

Figure 2.4. Resolved MT components for three models with varying strikes: a) strike = 30° with misfit = 0.02, b) strike = 195° with misfit = 0.3, c) strike = 15° with misfit = 1.2. Black solid line indicates resolved time histories of MT components and dashed red line represents the input model time histories.

Now I map the source orientations for which we can resolve, or not, the MT components (Figure 2.5). This is done for all three examined source depths. We can immediately see the depth dependence of my results as for the source depth of 1000 m b.s.l. we can resolve correct MT components for all strike angles. However, for shallow sources the orientation plays an essential role.

2.6 Discussion

2.6.1 'Improvements' to the seismic network

Naturally, the next step is to examine how the moment tensor inversion results could be improved. The original seismic network configuration (Figure 2.1) only has two stations (MBRY, MBLG) east of the volcano, therefore the azimuthal coverage is not ideal. For this reason I added three stations on the eastern part of the island - MBDS, MBJN, MBPS (Figure 2.6). As we would expect

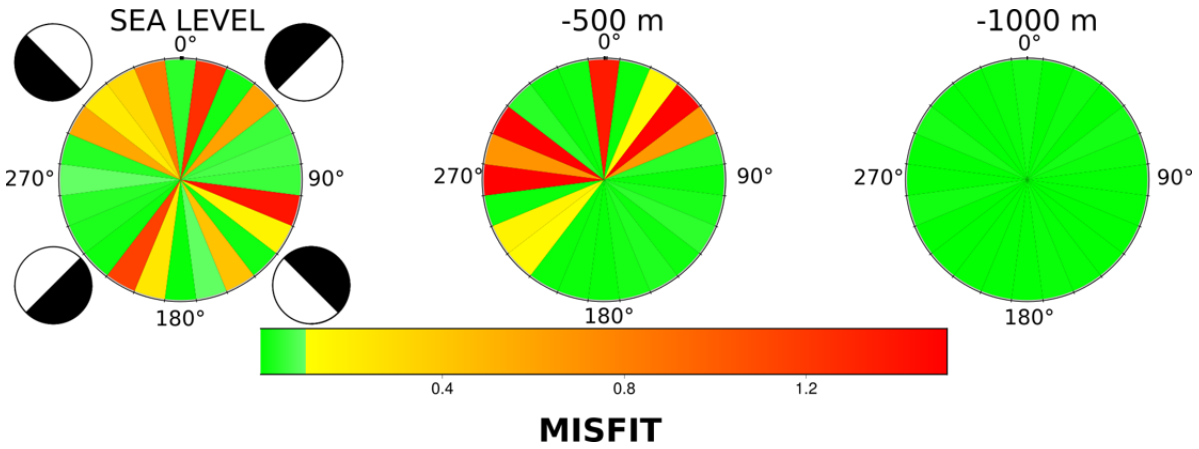

Figure 2.5. Map of the source orientations for which we can resolve (or not) the MT components for source depths at sea level, 500 m b.s.l., and 1000 m b.s.l. When the misfit is below 0.1 the results are marked with green, meaning that we can resolve source components correctly. When it is between 0.1 and 0.8 they are coloured on a spectrum from yellow (0.1) to orange (0.8), meaning that we need to be careful with interpreting these results, and everything with a misfit above 0.8 is coloured red and those results should not be trusted.

the results are improved drastically. It is interesting to see that, although the results for most of the strike angles are improved, for some it improved to a lesser degree, e.g. strike 105° for the source at sea level, and for some strike angles, e.g. strike 165° and 180° it became worse. A similar situation is seen when the source is placed at 500 m b.s.l., where for the strikes of 105° and 135° the correct MT components became impossible to resolve. However for all other strike angles the results were greatly improved.

2.6.2 'Eruption' scenarios

Next I looked at different 'eruption' scenarios where less than nine stations were operational. I created four different models, two for network configurations with six stations and two when the network configurations comprised four stations (Table 2.1). Model A (Figure 2.7), consisting of six stations (MBBY, MBFR, MBGH, MBRY, MBWH, MBWW), was used as it mimics the station configuration which was active during the March 2012 volcanic crisis when a VLP signal was observed which is the focus of the Chapter 3. Model B (Figure 2.8) again uses six stations (MBBY, MBFR, MBGB, MBWH, MBWW, MBDS) where one station (MBGH) from Model A was replaced with a new synthetic

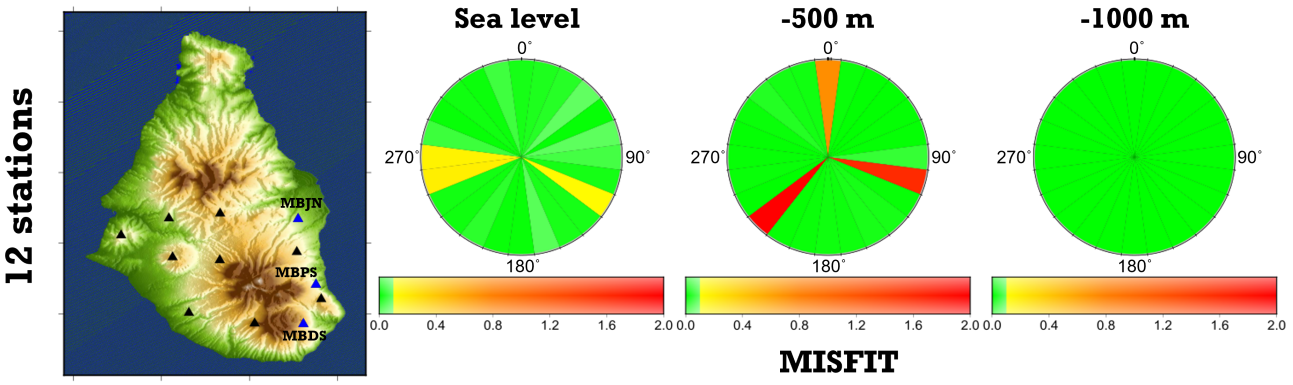

Figure 2.6. Improvements to the seismic network. The original station configuration is represented using black triangles and the three new stations (MBDS, MBJN, MBPS) are represented with blue triangles. There is a general improvement of the results, except for two strike angles for the source at sea level ($\phi = 165°$ and $\phi = 180°$) and at 500 m b.s.l. ($\phi = 105°$ and $\phi = 135°$).

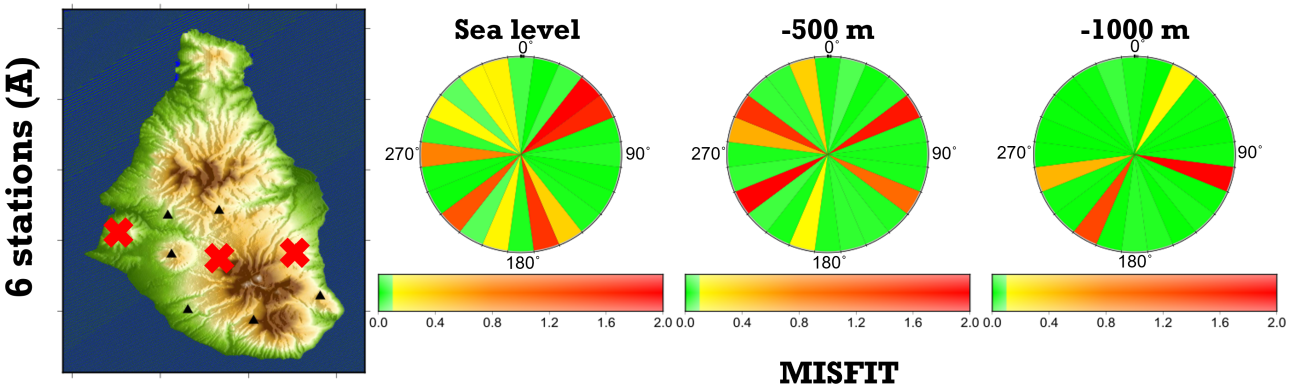

Figure 2.7. Station configuration and MTI results for Model A.

station (MBDS) to improve the azimuthal coverage east of the volcano summit. The MTI results for these two models are somewhat comparable, for the shallower source depths the overall area of the map in green is similar for the two models but where for some strike angles it was possible to fully resolve MT components, it was not possible to resolve them in the other model. Surprisingly, for the largest depth, it was possible to correctly resolve MT components for almost all strike angles, while I didn't have the same efficacy in the Model B set up.

As expected for the other two models (Models C & D) where only 4 stations were used in the inversions the results were inferior. For the Model C only

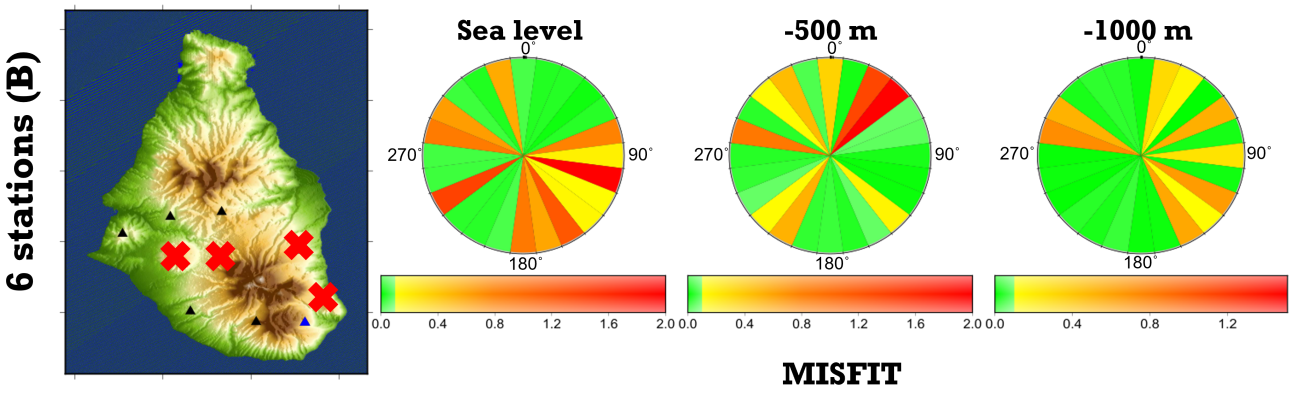

Figure 2.8. Station configuration and MTI results for Model B.

the four most distant stations (MBGB, MBGH, MBWH, MBWW) from the volcano were used in the inversion (the same station configuration model used in Section 2.4). Although the seismograms were able to be resolved perfectly as seen in the Figure 2.3 we can see that MT components couldn't be resolved for any of the strike angles (Figure 2.9). However, if we keep the number of stations the same, just exchange one station (MBGH) with another one on the other side of the volcano (MBRY) the results are improved, especially for deeper depths (Figure 2.9). This shows the influence the azimuthal coverage has on the moment tensor inversion. Lanza and Waite (2018) report that in their tests for the station configurations which have maximum azimuthal gaps between adjacent stations less than 130° they were able to obtain better results than for than configurations with the same number of stations but larger azimuthal gap. Similarly, we see here that when adding a station which is $\approx 180°$ away from its adjacent stations we can considerably enhance the ability to correctly resolve MT components.

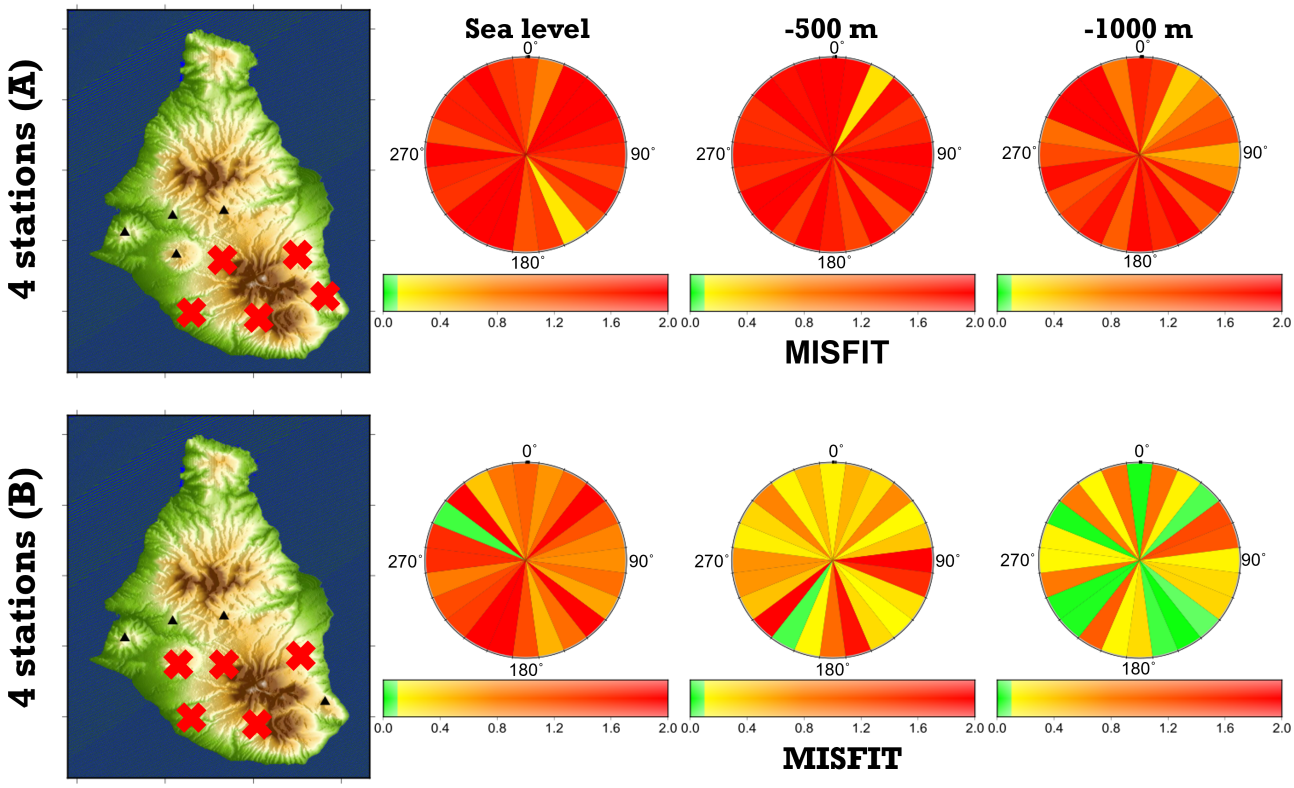

Figure 2.9. Station configuration and MTI results for Models C (top) and D (bottom).

Table 2.1. Different station configuration models used for the eruption scenarios. Station names in blue indicate the new synthetic stations.

Station	Model A	Model B	Model C	Model D
MBBY	✓	✓		
MBFR	✓	✓		
MBGB		✓	✓	✓
MBGH	✓		✓	
MBLG				
MBLY				
MBRY	✓			✓
MBWH	✓	✓	✓	✓
MBWW	✓	✓	✓	✓
MBDS		✓		
MBJN				
MBPS				

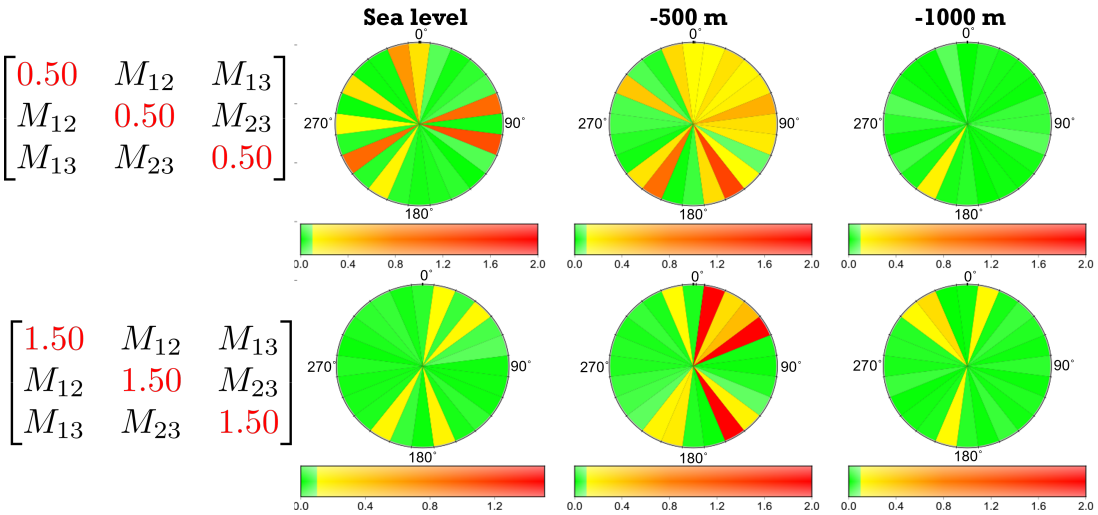

Figure 2.10. Influence of isotropic component on MTIs using 9 stations. Comparing with Figure 2.4 we can see how the area of well resolved MT components becomes bigger as we include the isotropic component.

2.6.3 Influence of the isotropic component

A big focus of my research are very-long period (VLP) seismic signals. As they are caused by sudden pressure transients inside a volcanic edifice often caused by volcanic fluid movement, we can expect a significant isotropic component of the moment tensor. For this reason, I examine the influence of the isotropic component in these moment tensor inversion resolution tests. I keep the off-diagonal MT components of my input signal the same but I add either $M_{11} = M_{22} = M_{33} = 0.5$ or $M_{11} = M_{22} = M_{33} = 1.5$ as my diagonal MT components. The tests are then done for MTI using the nine station configuration (Figure 2.10) and for the Model A station configuration (Figure 2.11 and Figure 2.12). The influence of the added isotropic component is visible in all of the examples. This was an encouraging result prior to performing moment tensor inversion on real data for the observed VLP signal on Montserrat which is presented in the next chapter.

2.7 Conclusion

These tests show the absolute necessity to take into account the seismic network configuration when performing moment tensor inversions. Special care has to be taken when the number of stations used in the inversion is small and/or

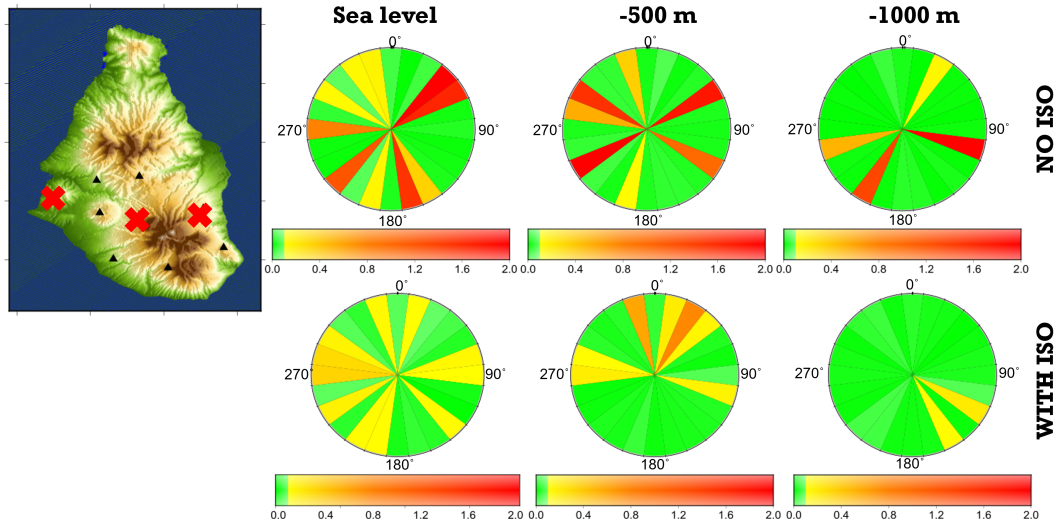

Figure 2.11. Comparison between how well can we resolve MT components using a 6 station network configuration when the isotropic component is applied and when it is not. The value for the isotropic MT components used in these tests is 0.5.

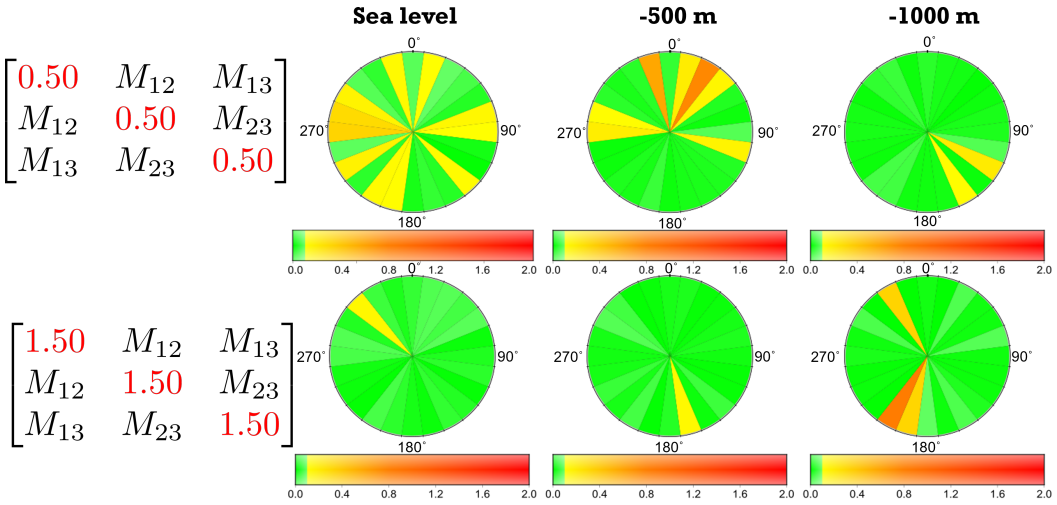

Figure 2.12. Influence of isotropic component on MTIs using 6 stations.

the azimuthal coverage is poor, that the seismogram fit between observed and resolved waveforms is not indicative of a correct moment tensor result as it does not guarantee the choice of the correct model for a non-unique solution. While temporal networks are often designed so they have great azimuthal coverage with stations near the source, permanent seismic network configurations are often affected by the inaccessibility to certain locations. These tests can therefore be performed by volcano observatories to predict their ability to invert for a variety of source orientations, with or without volumetric components, in dependence on the station configuration and draw upon these results in times of re-deployment or seismic upgrades of their seismic network in order to add, remove or exchange certain location of the stations. In future work it would also be of great interest to see the possible influence of station configuration on the ability to locate earthquakes.

Chapter 3

VLP signal on Montserrat - A MTI Case Study

3.1 Introduction

The eruption of Soufrière Hills volcano (SHV) began in 1995 and has consisted of five phases of magma extrusion, the last of which ended on 11 February 2010. After more than two years of quiescence with no lava extrusion and low seismicity, two swarms of around 50 volcano-tectonic (VT) earthquakes occurred at SHV on 22 and 23 March 2012 (Smith, 2015). The most intense VT swarm lasted for around 15 minutes, starting at 07:10 UTC on 23 March 2012 (Figure 1.7a). During this swarm, a local magnitude (M_L) 3.9 VT earthquake was observed at 07:20 UTC making it the largest VT earthquake ever observed on Montserrat till that date. This was followed by three hybrid events that terminated the swarm at 07:22 UTC (Cole et al., 2012). Several hours after this swarm, a short episode of ash venting began and an elevated SO_2 flux was recorded between 23 and 27 March - peaking at 4600 t/day on 26 March 2012. What made this VT swarm unique were two 'hidden' very-long period (VLP) signals which were observed across the MVO (Montserrat Volcano Observatory) seismic network during this swarm coinciding with a large amplitude strain signal ($\sim$ 280 nano strain) recorded on borehole strainmeters on the island (Hautmann et al., 2014).

Although some VLP seismicity can be seen clearly on broadband velocity seismograms (e.g. Jolly et al., 2017), VLP signals often cannot easily be identified in the velocity domain. This is due to the instrument acting as a

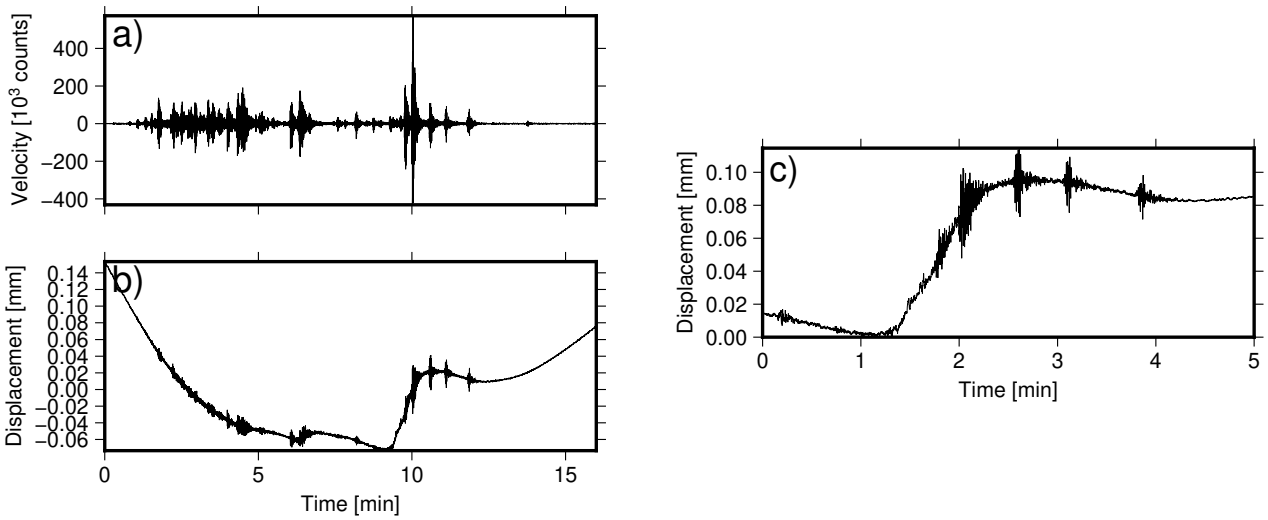

Figure 3.1. a) 16 min record of a VT swarm observed on 23 March 2012. b) Displacement seismogram obtained after a restitution process where we considered spectral components to a period of 1000 s showing the two VLP signals. c) Five min long time window showing the larger VLP signal.

differentiator converting ground displacement to velocity, whereby the instrument amplifies the high frequencies. Furthermore, a band-pass filter is applied defined by the instrument response. In such a case, a simple way to identify a VLP signal is to integrate the velocity seismogram or to apply a low-pass filter. In our case, after integrating the velocity seismogram, we see two clear VLP signals, one starting at 07:16 UTC and the other one, with much larger amplitude, at 07:19 UTC (Figure 3.1).

In this chapter I focus on the second, larger amplitude signal and use it as a case study to highlight the significance of the correct treatment of instrument removal as a necessary, crucial step in data processing. It is worth noting that when the periods of these signals fall into the far end of the very-long period range they are often referred to as an ultra-long period (ULP) seismic signals. The event I am describing in this chapter falls into that range of ULPs, however I choose to call it a VLP as the source process between these two types of signals does not differ.

This chapter is based on Sindija et al. (2021) where we emphasise the importance of taking into account how different seismometers influence the observed signals and what the necessary processing steps are in order to retrieve the maximum amount of information from the observed waveforms (Figure 1.7). We try to retrieve information suppressed by the instrument and subsequently,

use this information in the moment tensor inversion to estimate the location and other source parameters. The so-called restitution process, i.e. obtaining the time-history of the VLP surface displacements, described in Section 1.3 and the ground displacement modelling was part of my Master by Research degree. The moment tensor inversion segment of the work is the product of my PhD work.

3.2 Data acquisition

At the time of the event the seismic network on the island of Montserrat consisted of nine stations equipped with three-component broadband seismometers. Due to recording problems, the number of stations available for this study was reduced to six: Waterworks (MBWW) station, deployed by the University of Leeds, equipped with a 120 s Güralp-3T broadband instrument, Broderick's Yard (MBBY) and Windy Hill (MBWH) stations with 60 s Güralp-3ESPC broadband instruments, and stations Fergus Ridge (MBFR), St. George's Hill (MBGH), and Roche's Yard (MBRY) equipped with 30 s Güralp-40T broadband instruments (Figure 3.2). All data were recorded with a sampling rate of 100 Hz and were processed using the software package Obspy (Krischer et al., 2015).

3.3 VLP ground displacement

Figure 3.1c shows the vertical component ground displacement of the VLP signal observed at MBWW, obtained by the restitution process described in Section 1.3. However, due to the very low frequency content of the VLP, the restitution method described in Section 1.3 was not applicable for the stations equipped with instruments with natural periods shorter than 120 s. These instruments have a much lower signal to noise ratio at long periods. A way around this problem is using the following forward modelling technique: we assume a ground displacement model, or adopt the one determined by the 120 s instrument as a starting model. Next we apply the instrument response of the 60 s or 30 s seismometers to this trace, differentiate it, and compare the resulting synthetic velocity seismogram with the velocity data. As a starting model for ground displacement we use an approximation of the waveform

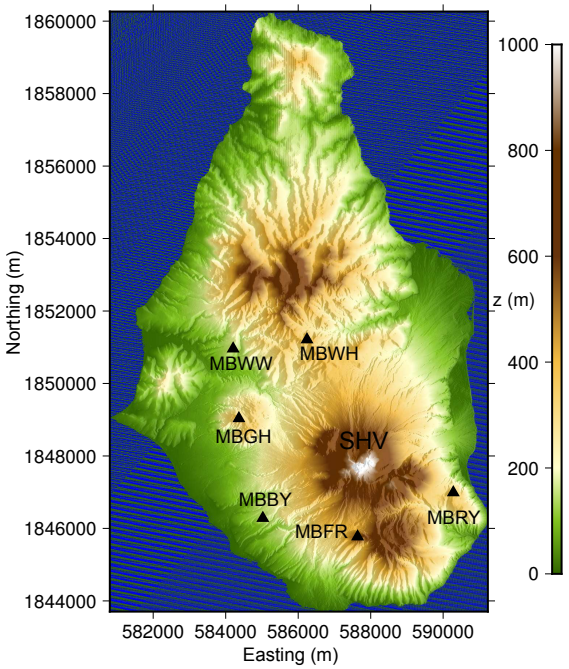

Figure 3.2. Topographic map of Montserrat with 6 operational stations on March 23, 2012.

that we obtained from the vertical component of the 120 s instrument at the MBWW station. Vertical components are generally less affected by noise than the horizontal components. One has to be aware that such an approach makes all following results highly dependent on the single station MBWW. If the instrument response is even slightly incorrect the effect will be carried across the network into all synthetic displacement seismograms and, therefore, into the model. Similarly, any other noise at MBWW would be carried through to the rest of the stations.

In the limited 5 min time window (Figure 3.1c), the restituted signal appears to be a step function, however, outside this time window the long term behaviour cannot be uniquely determined. As the signal was recorded with a velocity sensor (seismometer) a static offset represented by the step function will always decay to zero. Nevertheless, focusing on the source process in our volcanological study, we are interested in the initial slope of the signal. Therefore, in contrast to VLP signals on other volcanoes that are observed and interpreted as oscillatory behaviour (e.g. Dawson and Chouet, 2014; Caudron et al., 2018) and the VLP signal from Whakaari described in Chapter 4, we assume a step-like displacement. We model it by using the Richards Growth

Equation (RGE), a generalised logistic function defined by upper (K) and lower (A) asymptotes, the curve growth rate (B), the time of the maximum growth (M), and the asymmetry parameter (ν) (Richards, 1959; Green and Neuberg, 2005):

$$Y(t) = A + \frac{K - A}{[1 + e^{B(t-M)}]^{1/\nu}}. \tag{3.1}$$

We adjust the parameters of the step function to match the restituted ground displacement of the vertical component of the 120 s instrument (Figure 3.3). This trace is now used as the input to create the synthetic velocity seismograms for the 120 s, 60 s, and 30 s instruments, respectively. First we apply the 120 s instrument response (including differentiation), apply a low-pass filter with cut-off frequency of 0.05 Hz, and compare it with the data of MBWW where the same low-pass filter had been applied to remove the superimposed short-period events (Figure 3.3). The comparison shows that even though the amplitude of the step function is well constrained by the restituted data from the MBWW station, the modelled step function does not match the detailed time history in the velocity domain. The same discrepancy is also seen when comparing the resulting velocity seismograms of the band-limited stations with the original data on other components and stations. Upon more detailed analysis of the restituted ground displacement at MBWW we noticed a change of slope in the step function approximately 1.5 minutes (t_0) into the trace. To model this discontinuity, we designed a two-phase step function using the RGE as a basis to see if a change in the slope can explain the discrepancy in the velocity domain. The modified step function is therefore divided into two phases, Y_{phase1} and Y_{phase2} (Figure 3.3) described respectively as:

$$Y_{\text{phase1}}(t) = A_1 + \frac{K_1 - A_1}{[1 + e^{B_1(t-M_1)}]^{1/\nu_1}}, \; t \leq t_0 \tag{3.2a}$$

$$Y_{\text{phase2}}(t) = A_2 + \frac{K_2 - A_2}{[1 + e^{B_2(t-M_2)}]^{\nu_2}}, \; t > t_0. \tag{3.2b}$$

We make the crucial assumption that the change in the slope happens at the same time for all components at all stations. Due to the wavelength of the signal, the arrival time difference at different station is negligible, therefore we can take this assumption into account. The function is made continuous by selecting A_2 which minimises $|\max(Y_{\text{phase1}}) - \min(Y_{\text{phase2}})|$ at t_0. Applying the

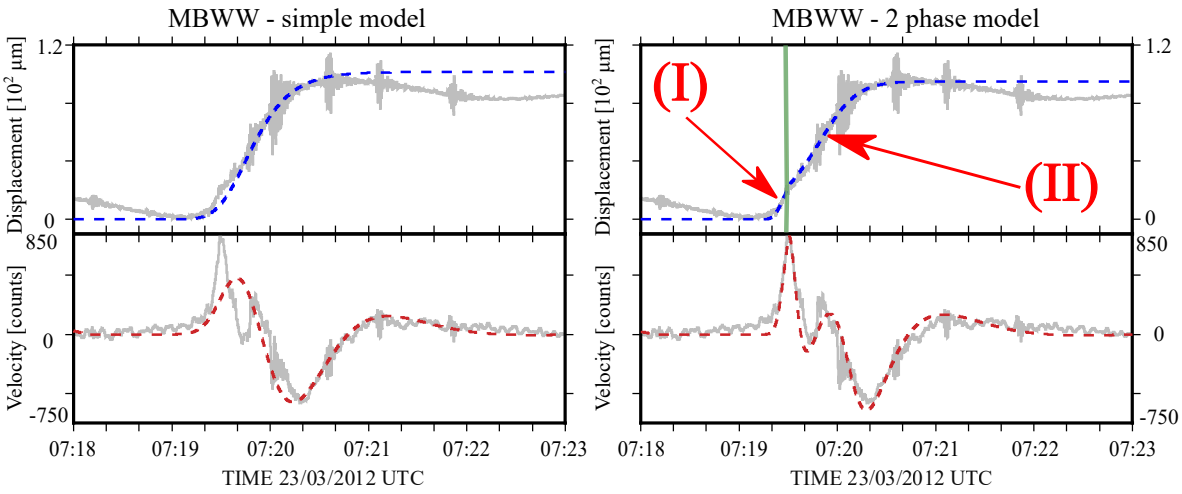

Figure 3.3. Ground displacement models (blue dashed lines) based on the restituted ground displacement (grey) at MBWW on March 23, 2012; using a simple step function (left) and using a 2 phase step function (right). We apply the band-pass limited instrument response and differentiate both ground displacement models and then compare the resulting synthetic velocity data (red dashed line) with the low passed filtered (below 20 s) observed data (grey). The green vertical line represents the onset time of the change of slope and the roman numerals represent the two phases of our modelled step function.

instrument response to this model for ground displacement produces a synthetic velocity seismogram which now matches the data in the velocity domain. After we have shown this model works for a station equipped with 120 s instrument, we examine how well our ground displacement model fits at stations equipped with 60 s and 30 s instruments. While for station MBWW the displacement model is fitted to the restituted ground displacement, for other stations we use the simulated annealing (SA) method (Du and Swamy, 2016) to determine the best fit. We vary the ground displacement model parameters equation (3.2) and the goodness of fit is measured in the velocity seismogram. A 95 % confidence interval has been included on the overall step amplitude estimate. Therefore, a

10% uncertainty in the estimate of the step amplitude linearly translates into 10 % uncertainty in the volume change estimate in Section 3.4.1. Using the method of Wielandt and Forbriger (1999) we also removed the effect of the tilt from the horizontal components. Our results show that the two-step model can explain the observed velocity waveforms on all available stations in the network for both the vertical and horizontal components (Figure 3.4, Figure 3.5, Figure 3.6). Furthermore, the results from 60 and 30 s stations reinforce our selection of the 1000 s high-pass filter as appropriate for the restitution process because if our ground displacements were not a step-like function it would not provide a good match in the velocity domain. While the combined fit in the velocity and displacement domain was necessary to circumvent the bandwidth limitations of 30 and 60s instruments, this approach also revealed the advantages of capturing details in the time history of the signal in the velocity domain.

The final best fit models are shown in Figure 3.5 and Figure 3.6 and the horizontal displacement vectors, based on the maximum displacement amplitudes are shown in Figure 3.7. Based on the directivity and the amplitudes of the restituted and modelled ground displacements, we can infer a shallow source. Furthermore, we must note the directivity of displacements at MBBY as it is the only station where the vertical component displacement is negative and the horizontal components are directed 'away' from the source (assuming a source below summit of the volcano). The possibility that the station was installed with reversed polarities was discarded by comparing teleseismic earthquake data across the entire network. Therefore, I continue the analysis with unchanged polarities at MBBY.

3.4 Moment tensor inversion

Only after we perform the appropriate restitution process, obtaining the amplitude and time history of the displacements, we can evaluate the volume change at the source by performing a moment tensor inversion. I approach this problem from several angles: (a) using the previously described MTI code VOLPIS (Cesca and Dahm, 2008) where I solve for both source time history and the MT components and (b) by performing an MTI where the source time history is assumed.

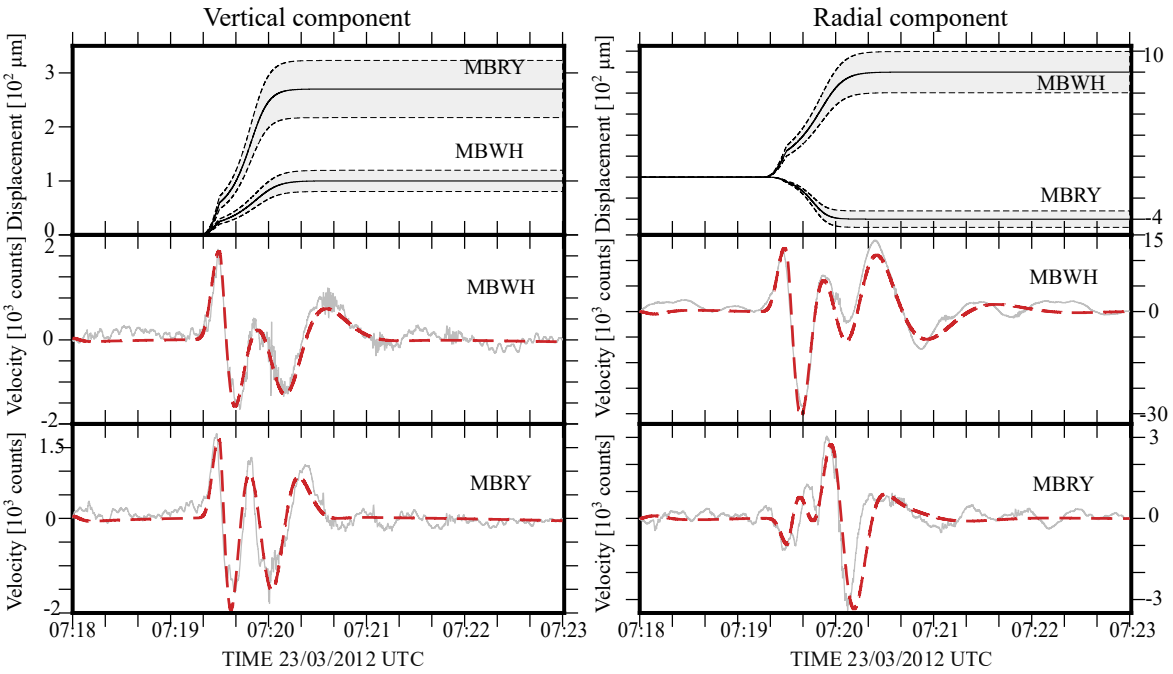

Figure 3.4. Vertical (left) and radial (right) component of the modelled ground displacements for stations MBWH and MBRY using the 2 phase step functions. The 95 % confidence intervals are shown as grey shaded areas. After simulating the instrument response we compare the synthetic velocity data (red dashed line) with the observed data (grey). A low-pass filter with cut-off frequency of 20 s is applied to both synthetic and observed data.

3.4.1 Method A - Resolving both source time history and MT components

Using the VOLPIS code (Cesca and Dahm, 2008) one can resolve both the moment tensor (MT) and single force (SF) components, as well as the source time history. To simplify the MTI but still keep the necessary information obtained from the restitution and ground displacement modelling, I also simplify the resolved source time histories. As in the MTI, we are mostly interested in the amplitude of the step-like displacement itself, I model the displacements again as a simple step function (equation (3.1)). The simple displacements are modelled individually based on the 2 phase step function so the start, end, and the maximum amplitude of the 'static' displacement is equal. Additionally,

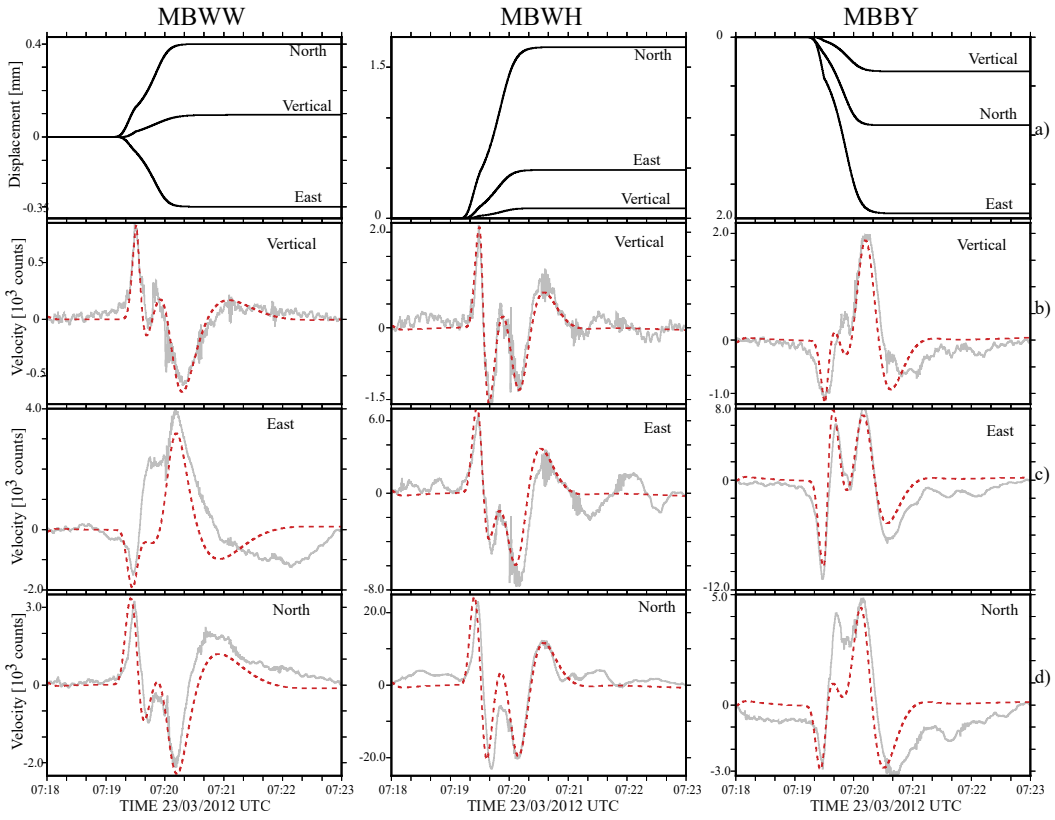

Figure 3.5. (a) Displacement models for all three components at stations MBWW, MBWH, and MBBY. (b-d) After applying the instrument response and differentiating the resulting synthetic velocity seismogram is band-passed (red dotted) and compared with the band-passed velocity seismogram (grey). The velocity seismograms are filtered between 0.001 and 0.05 Hz.

as VOLPIS is a frequency domain inversion code, the large static step at the end of the displacement models could make the inversion unstable. Therefore I differentiate the resulting displacement step models:

$$v(t) = \frac{\mathrm{d}}{\mathrm{d}t} Y(t) = \mathcal{F}^{-1}\left[j\omega\mathcal{Y}(\omega)\right], \ \mathcal{Y}(\omega) = \mathcal{F}\left[Y(t)\right] \tag{3.3}$$

where $v(t)$ represents the velocity trace, $Y(t)$ is a simple step function, and the $\mathcal{F}$ indicates the Fourier transform. The MTI is therefore performed in the velocity domain resulting in the moment rate components. The resolved moment rate components are then integrated and can be directly compared with the source time history used for modelled displacements. The Green's functions are computed using a spectral element method SPECFEM3D (Komatitsch et al., 2012), for a volumetric grid (2.0 km $\times$ 1.2 km $\times$ 0.8 km) (Figure 3.8) of 385

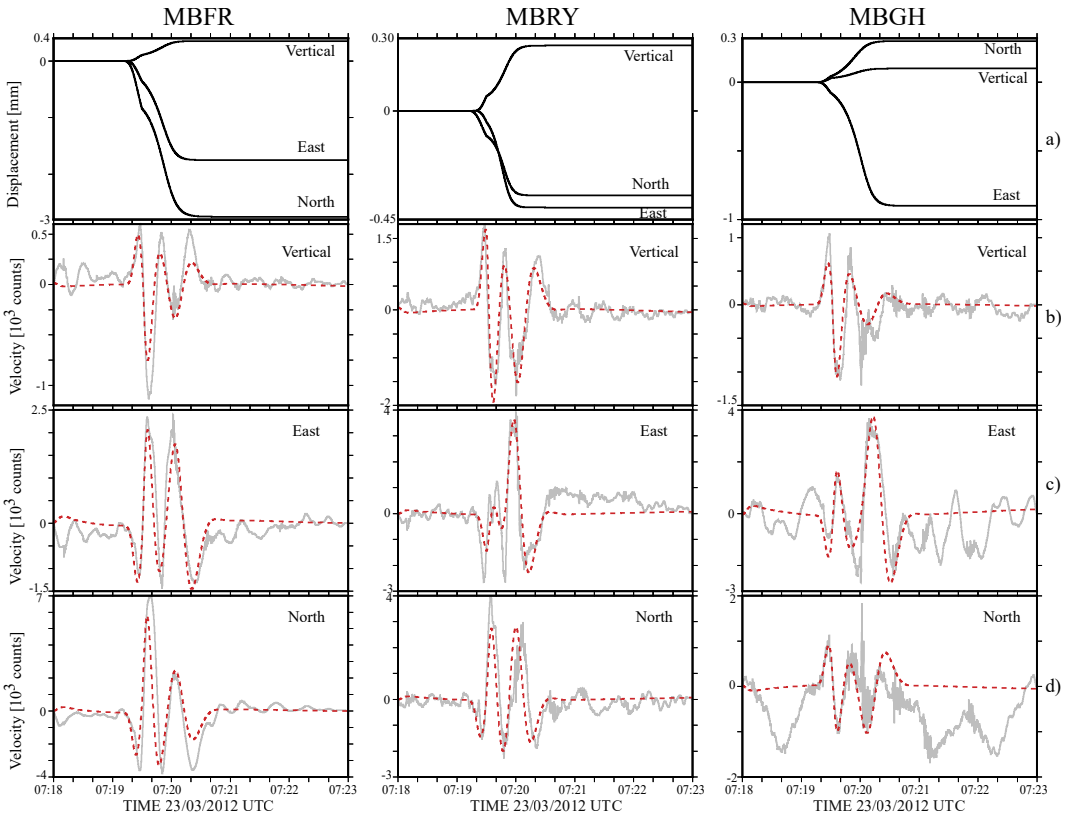

Figure 3.6. (a) Displacement models for all three components at stations MBFR, MBRY, and MBGH. (b-d) After applying the instrument response and differentiating the resulting synthetic velocity seismogram is band-passed (red dotted) and compared with the band-passed velocity seismogram (grey). The velocity seismograms are filtered between 0.001 and 0.05 Hz.

possible source locations with grid spacing of 200 m centred below the summit of SHV. The Green's functions are calculated taking into account topography and assuming a homogeneous halfspace with $v_p = 3500$ km/s, $v_s = 2000$ km/s, and $\rho = 2600$ kg/m^3. The VLP signals have wavelengths much larger than the source-receiver distances, therefore we shouldn't expect any influence from short wavelength subsurface heterogeneities, and the assumption of a homogeneous halfspace is justified. Results shown in Figure 2.12 in Chapter 2 showed that we can be fairly certain to resolve MT components if the isotropic components of the source MT are large. Therefore, assuming that I can estimate the location of the source by performing the MTI for each point in this volumetric grid and finding the minimum misfit between observed and synthetic velocity seismograms through the inversion using:

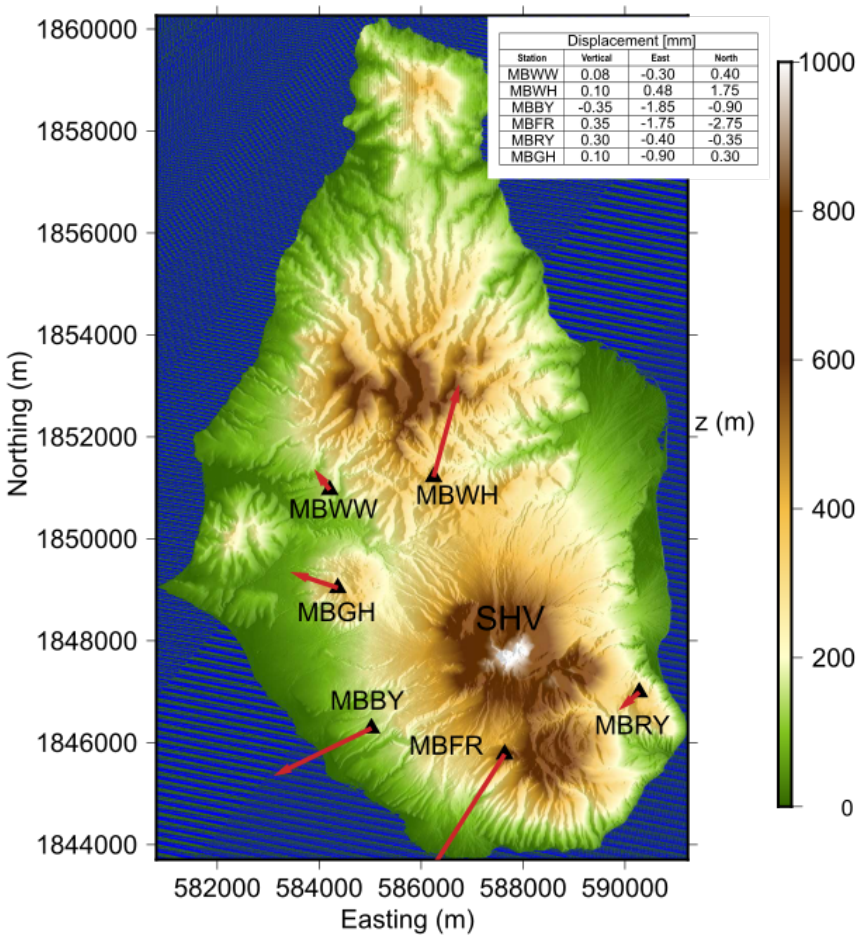

Figure 3.7. Horizontal displacement vectors at all available stations derived from the maximum amplitudes of the restituted/modelled step functions. The displacement amplitudes for all three components are shown in the table in the top right corner.

$$\text{misfit} = \left[\frac{\sum_{i=1}^{N_t} \sum_{j=1}^{M_i} (d_i(t_j) - s_i(t_j))^2}{\sum_{i=1}^{N_t} \sum_{j=1}^{M_i} (d_i(t_j))^2} \right], \tag{3.4}$$

where N_t is the number of time traces, M_i is the number of time samples for j-th trace, and $d_i(t_j)$ and $s_i(t_j)$ are the j-th samples of i-th time trace for input data and synthetic time trace, respectively (Cesca and Dahm, 2008). The misfit results are dimensionless and normalised. The data were decimated to 3 Hz sampling rate and bandpassed between 0.001 and 1 Hz. The inversions are done with the constraint that the source parameters have the same time

histories for the six MT components and a (possibly) different one for the SF components.

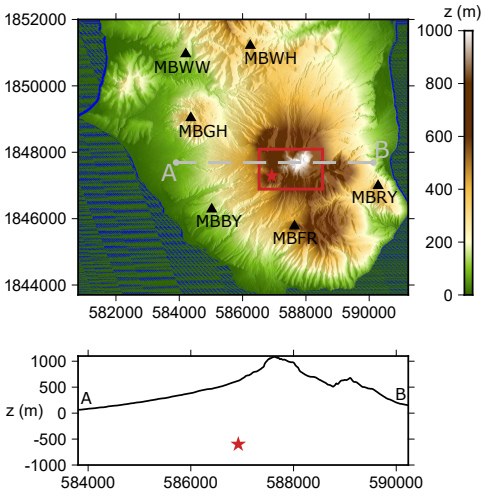

Figure 3.8. (top) Zoomed in map of Montserrat showing the horizontal boundaries of the volumetric grid of possible source locations. Location of the best-fitting model is shown with the red star. (bottom) Cross section profile (extracted from point A to point B) showing the depth of the source and its relative location from the summit of the SHV.

The best-fitting model was found to be at depth of 600 m, 1000 m west and 400 m south of the volcano summit (Figure 3.8). The resulting waveform fit (Figure 3.9) shows a good fit for all three components at all stations. The resulting moment and single force time histories are shown in Figures 3.10. By normalising the resolved moment tensor (Figure 3.10):

$$\boldsymbol{M} = M_0 \begin{bmatrix} M_{\mathrm{nn}} & M_{\mathrm{ne}} & M_{\mathrm{nz}} \\ M_{\mathrm{en}} & M_{\mathrm{ee}} & M_{\mathrm{ez}} \\ M_{\mathrm{zn}} & M_{\mathrm{ze}} & M_{\mathrm{zz}} \end{bmatrix} = 3.8 \times 10^{13} \begin{bmatrix} 0.53 & -0.29 & -0.55 \\ -0.29 & 0.13 & -0.44 \\ -0.55 & -0.44 & 0.73 \end{bmatrix} \mathrm{Nm} \quad (3.5)$$

we estimate the scalar seismic moment (M_0) to be 3.8×10^{13} Nm. The resolved vector of single forces is:

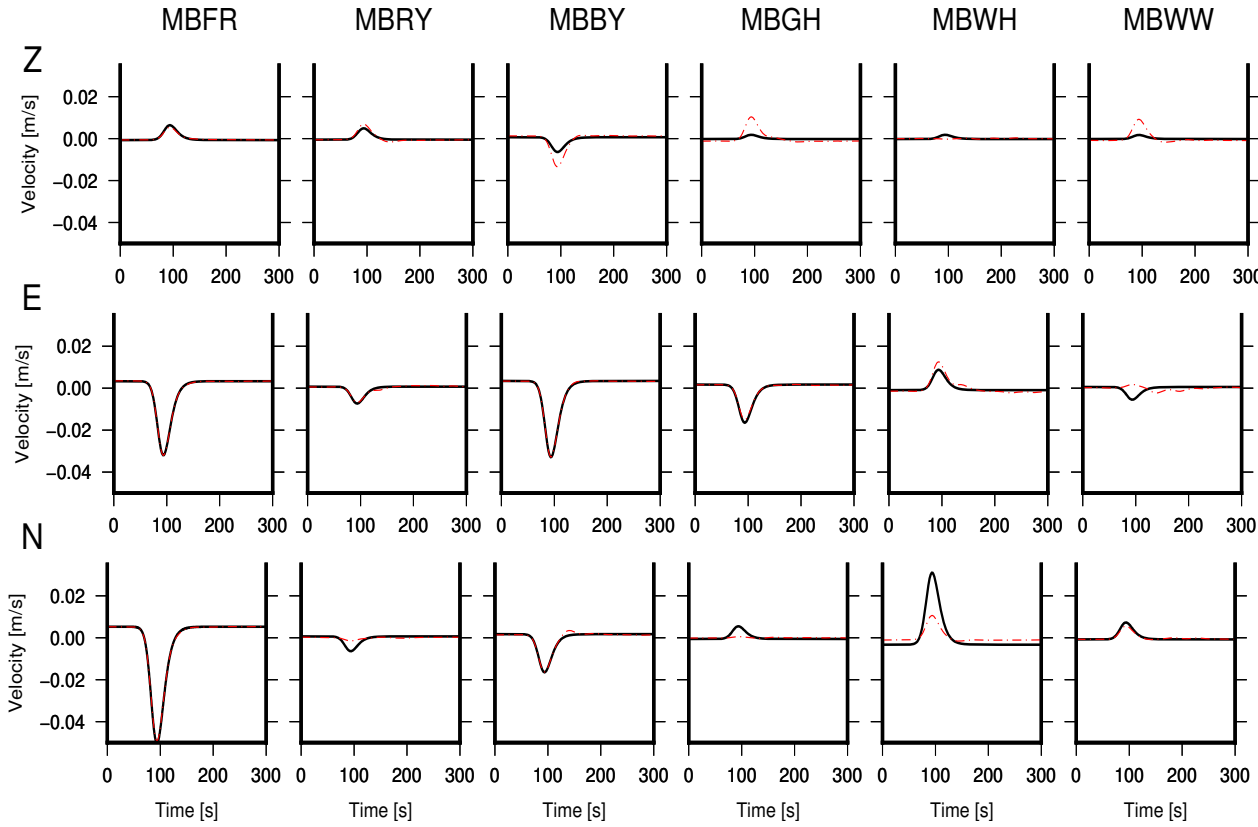

Figure 3.9. The seismogram fit in the velocity for three components at the available stations for the March 2012 event. Black solid line represents our input data for the inversion, while the dashed red line represents the best-fit solution synthetic data.

$$\boldsymbol{F} = F_0 \begin{bmatrix} F_{\mathrm{n}} \\ F_{\mathrm{e}} \\ F_{\mathrm{z}} \end{bmatrix} = 3.3 \times 10^{10} \begin{bmatrix} 0.17 \\ -0.75 \\ -0.64 \end{bmatrix} \mathrm{N} \tag{3.6}$$

Comparing the maximum amplitudes of single force components (Figure 3.10) and their moment counterparts we see that $|\frac{SF_{\mathrm{north}}}{M_{\mathrm{xx}}}| = 0.0003$ m^{-1}, $|\frac{SF_{\mathrm{east}}}{M_{\mathrm{yy}}}| = 0.005$ m^{-1}, and $|\frac{SF_{\mathrm{vert}}}{M_{\mathrm{zz}}}| = 0.0007$ m^{-1} demonstrating that the single force components are negligible. Following the decomposition of the resolved moment tensor by Vavryčuk (2001), we calculate the percentage of isotropic component to be 64%, CLVD component 12%, and double couple component to be 24%. The shear component has a strike of 187°, dip 21°, and rake 146°. The volume

change (ΔV) at the source is then estimated using $\Delta V = \dfrac{M_{\text{iso}}}{(\lambda + \frac{2}{3}\mu)}$, where M_{iso} represent isotropic moment and λ and μ are the Lamé parameters. Assuming a Poisson's ratio $\nu = \dfrac{1}{4}$, ($\lambda = \mu$) and the model space velocities as defined above, we estimate the source volume change to be $\Delta V = (1015 \pm 100)$ m^3. However, for volcanic rocks at or near liquidus temperature it may be more appropriate to use a Poisson's ratio $\nu = \dfrac{1}{3}$, ($\lambda = 2\mu$) (Murase and McBirney, 1973) which results in a source volume change $\Delta V = (635 \pm 60)$ m^3.

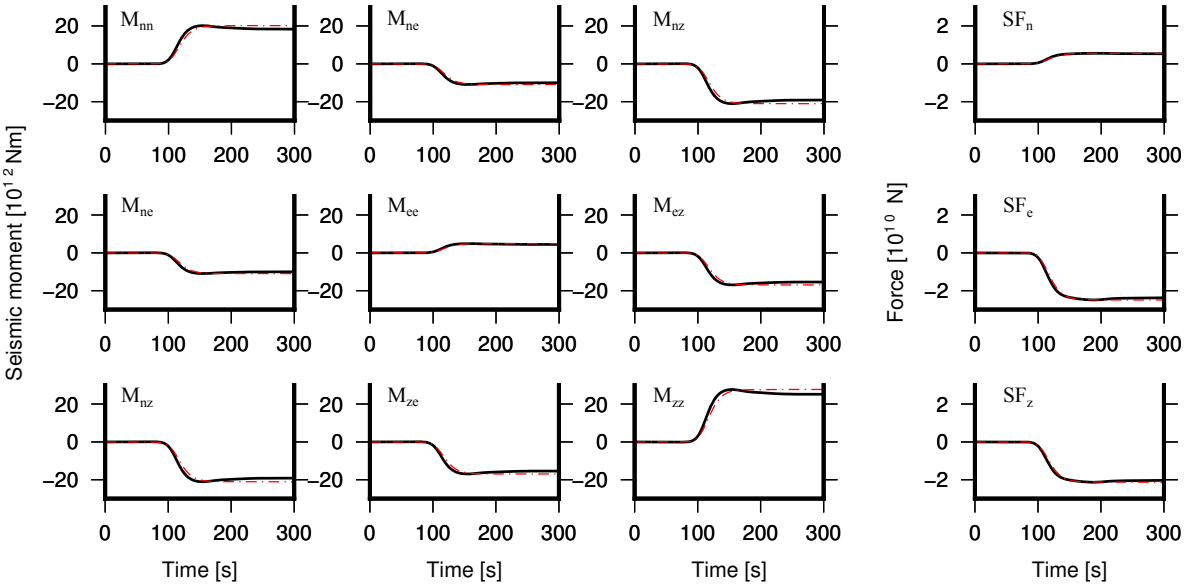

Figure 3.10. The resolved source time histories for the moment tensor and single force components (black). The average source time function used for the modelled displacements is multiplied with the moment tensor/single force component (dashed red line) so we can compare how well the shape of the displacement step function is resolved.

3.4.2 Method B - Assuming the source time history

In equation (1.1) we stated how the observed displacement field $\boldsymbol{u}$ at the station at position $\boldsymbol{x}$ can be described as an excitation of a point source at the position $\boldsymbol{\xi}$ represented by a moment tensor $\boldsymbol{M}$ and a single force $\boldsymbol{F}$. Using the notation from Ohminato et al. (1998) for the moment tensor and single force components:

$$\begin{aligned} m_1 &= M_{11} \quad m_2 = M_{12} \quad m_3 = M_{13} \\ m_4 &= M_{13} \quad m_5 = M_{23} \quad m_6 = M_{33} \\ m_7 &= F_1 \quad m_8 = F_2 \quad m_9 = F_3 \end{aligned} \tag{3.7}$$

and for the Green's functions

$$\begin{aligned} g_{n1} &= G_{n,11} \quad g_{n2} = G_{n,12} \quad g_{n3} = G_{n,13} \\ g_{n4} &= G_{n,13} \quad g_{n5} = G_{n,23} \quad g_{n6} = G_{n,33} \\ g_{n7} &= F_{n,1} \quad g_{n8} = G_{n,2} \quad g_{n9} = G_{n,3} \end{aligned} \tag{3.8}$$

we can re-write equation (1.1) as

$$u_n(\boldsymbol{x}, t) = \sum_{i=1}^{9} m_i(t) * g_{ni}(t). \tag{3.9}$$

As VLP signals have wavelengths of tens to hundreds of km, it places all of the seismic stations in the so-called near-field, i.e. within one wavelength from the source. In the near-field, the seismic displacement at the surface is directly proportional to the deformation at the source. In this example, where we observe a signal with a dominant period of approximately 100 s, or corresponding wavelength of 350 km, all stations are in the near field and we can relate our restituted displacement and models directly to the source volume change. Based on this fact and the results from my previous section where the source time histories of the MT components matched the "input" step functions, I can assume a source time function S_0 and, due to commutative and associative properties of multiplication and convolution operations, rewrite $m_i(t)$ as:

$$m_i(t) = m_i S_0(t), \tag{3.10}$$

and therefore, rewrite equation (3.9) as:

$$u_n(\boldsymbol{x}, t) = \sum_{i=1}^{9} m_i(t) * g_{ni}(t) = \sum_{i=1}^{9} m_i \left(S_0(t) * g_{ni}(t) \right) = \sum_{i=1}^{9} m_i g'_{ni}(t), \tag{3.11}$$

where $g'_{ni}(t)$ are 'practical Green's functions', i.e. Green's functions convolved with the source time function (Maeda and Takeo, 2011). However, this time I only invert for the moment tensor components, as the previous method revealed the negligible influence of the single forces. Therefore, instead of nine moment tensor and single force components in equation (3.11), I am only solving for the six moment tensor components. The volumetric grid of possible source locations for which the 'practical Green's functions were calculated is the same as in the previous method (1.2 km × 1.2 km × 0.8 km) and the practical Green's functions are calculated using the same method and medium as above. After I obtain the 'practical Green's functions' for each grid point, I estimate the location of the source by finding the minimum misfit between observed displacement seismograms and obtained synthetic displacement seismograms through the inversion using equation (3.4).

The best fitting model is located 400 m east and 600 m south of the summit of SHV at depth of 0 m (Figure 3.12). The resolved MT has the magnitude $M_0 = 1.6 \times 10^{15}$ Nm and its MT components are:

$$\boldsymbol{M} = M_0 \begin{bmatrix} M_{\mathrm{nn}} & M_{\mathrm{ne}} & M_{\mathrm{nz}} \\ M_{\mathrm{en}} & M_{\mathrm{ee}} & M_{\mathrm{ez}} \\ M_{\mathrm{zn}} & M_{\mathrm{ze}} & M_{\mathrm{zz}} \end{bmatrix} = 1.6 \times 10^{15} \begin{bmatrix} 0.49 & 0.14 & -0.37 \\ 0.14 & 0.49 & 0.75 \\ -0.37 & 0.75 & 0.30 \end{bmatrix}. \quad (3.12)$$

The percentage of isotropic component is 42 %, CLVD component is 10% and DC component is 48 %. Assuming a Poisson's ration $\nu = \frac{1}{4}$, ($\lambda = \mu$) the volume change is estimated to be $\Delta V = 3.9 \times 10^4$ m^3 while assuming Poisson's ratio $\nu = \frac{1}{3}$, ($\lambda = 2\mu$) the volume change is estimated to be $\Delta V = 2.4 \times 10^4$ m^3.

3.5 Discussion

3.5.1 Comparison of results

We can directly relate the observations at the surface to the source mechanism, by comparing the inverted time histories of moment tensor and single force components with the modelled source time function and, hence, obtain another verification of our moment tensor inversion result. Those show the

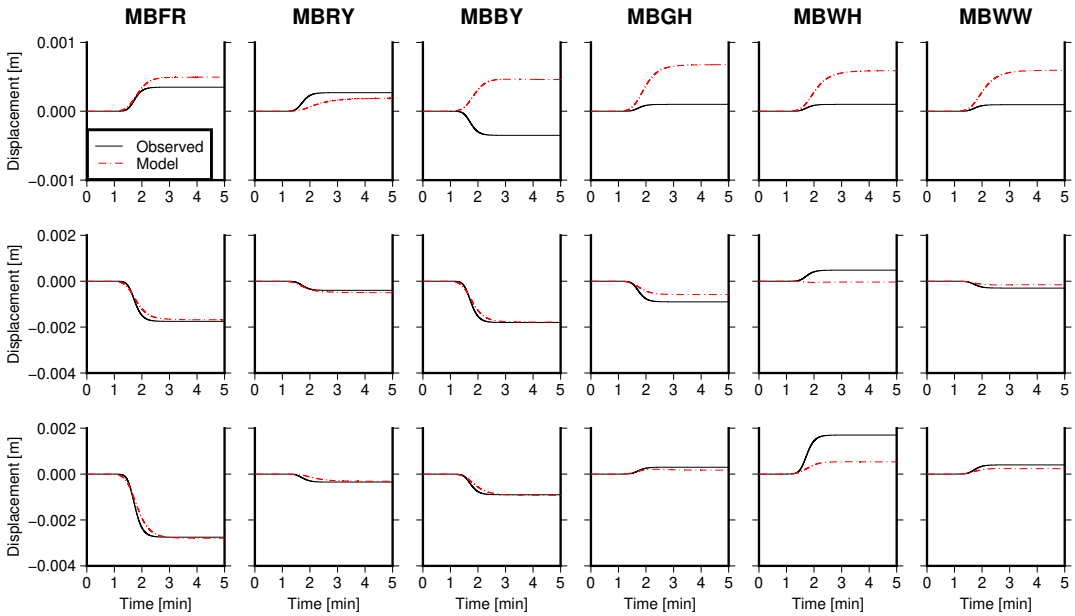

Figure 3.11. Results from the inversion using Method B for the March 2012 VLP event. The observed ground displacements are represented with the black line, while the results for the inversion for a source at depth 0 m are represented with the dashed red line.

source mechanism of the best-fitting model is an explosion with a strong shear component (Figure 3.13). However, we can see the discrepancy between the source locations and the source volume change estimated using the different methods. The potential bias of individual methods was then examined by two simulations - (1) Taking the moment tensor solution from Method A and using it as the input for the forward problem after which the MTI was performed using Method B (assuming a source time history and without single force components) and (2) the other way around, taking the moment tensor solution from Method B and using it as the input for the forward problem after which the MTI was performed using Method A.

For the first simulation I take the resolved location, moment tensor (equation (3.5)), and single force (equation (3.6)) and use them as a input source parameters for the forward problem. Then the combined displacement seismograms from these two source processes are used as an input for the MTI where only MT components are solved for. The MTI results in the correct location and correctly resolved MT components. As expected, this result proved that the influence of the single force components is negligible.

In the second simulation I take the resulting seismograms from Method B

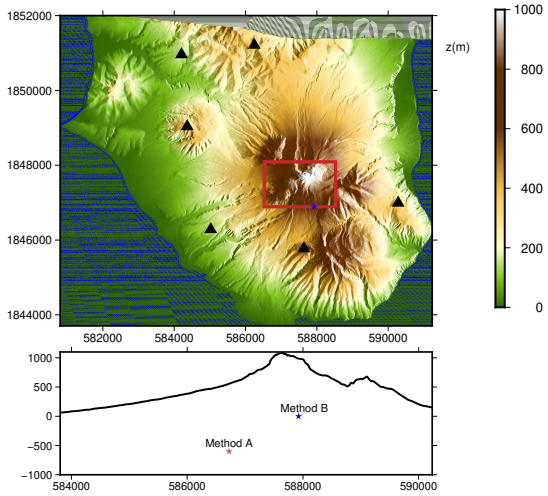

Figure 3.12. (top) Locations of the best-fitting model estimated using Method A (red star) and Method B (blue star). (bottom) Cross section profile showing the depth of the sources and their relative location from the summit of the SHV.

and use them as the input data for moment tensor inversion performed using Method A. The idea is to check if this method shows any leakage of the moment tensor components into single force components. The MTI does not result in the correct location of the source as it moves the source 200 m north and 400 m west on the grid. The resulting velocity seismograms (Figure 3.14) again show a good seismogram fit. However, as it was previously shown, a good seismogram fit does not necessarily result in an equally good source components fit (Figure 3.15).

3.5.2 Source excitation

Using strain data from 3 borehole dilatometers, Hautmann et al. (2014) described this ash venting event as being initiated by the ascent of magmatic fluid from deeper magmatic system into a shallow dyke. However, based on our estimate of volume change and depth we can speculate that it is not the sudden movement of magma that initiated this event. As there was an elevated SO_2 flux recorded after this VLP event we speculate that the source excitation for this event was gas accumulation and release after a new summit vent opened. The resolved downward single force component corresponds to the sudden removal of the vent seal (Ohminato et al., 2006b). A different hypothesis is that the VLP event was due to CO_2 flushing. If the free gas phase of CO_2, degassing

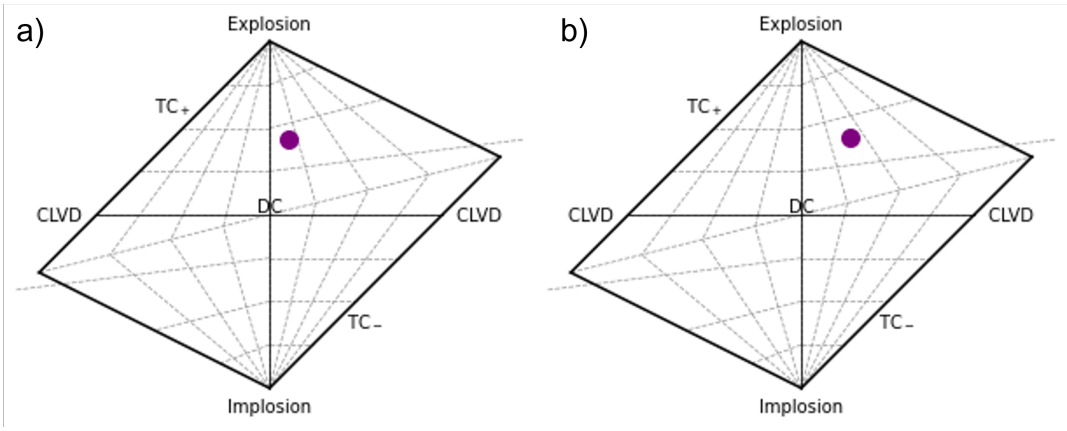

Figure 3.13. Hudson plots showing the source mechanism resolved using (a) Method A and (b) Method B. Both methods estimate the source mechanisms to be an explosion with a strong shear component.

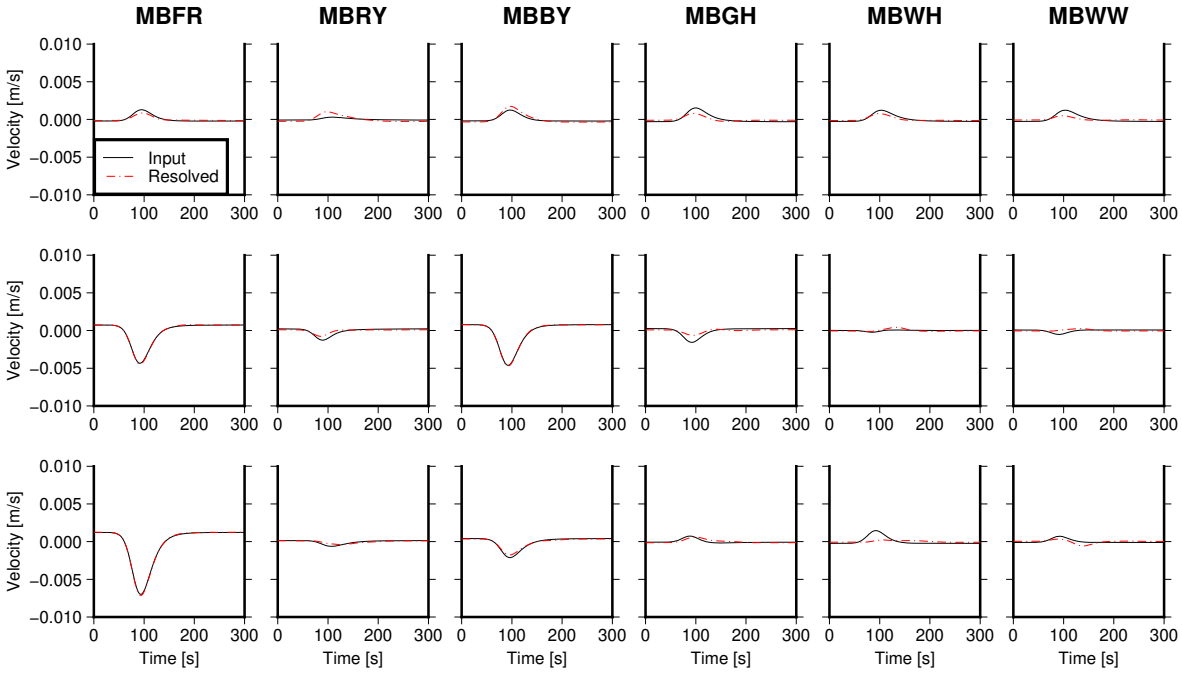

Figure 3.14. MTI performed with Method A showing resolved resolved velocity seismograms (red dashed line) compared with the input velocity traces (solid black) obtained using Method B moment tensor inversion.

at larger depths hits a supersaturated magma batch it can trigger the rapid exsolution of water resulting in a sudden volume change (Caricchi et al., 2018). Looking at a broader aspect of the previous eruptive behaviour of SHV, such modulations could have been a trigger for the onset of a new eruptive phase which would explain why it is not the overpressure or a certain volume recharge

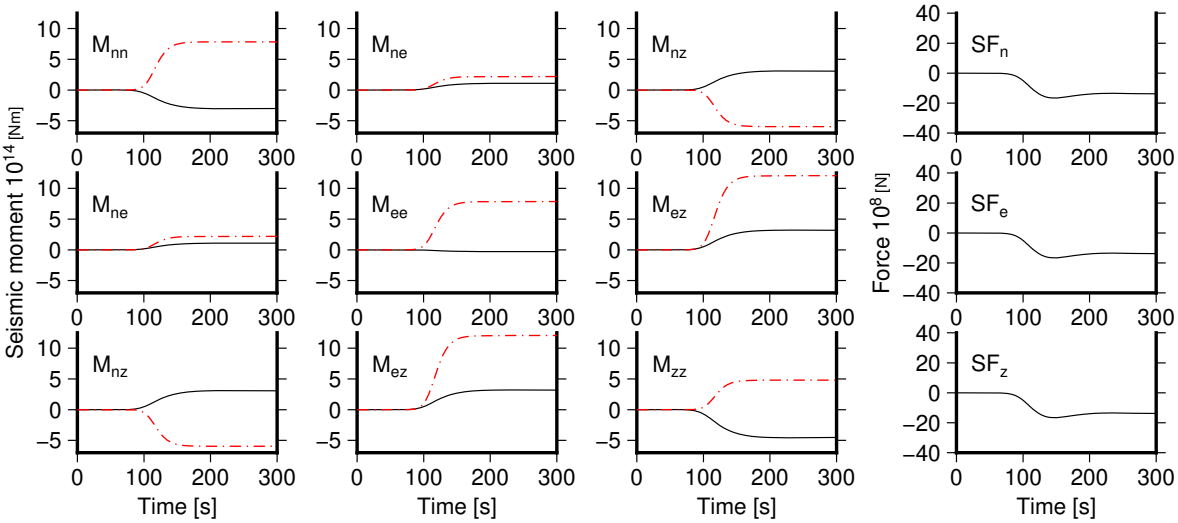

Figure 3.15. MTI performed with Method A showing resolved MT and SF components (solid black line) compared with the input source mechanism (dashed red line). The input mechanism used was the resolved MT using Method B.

that needs to be reached to start an eruptive phase (Figure 3.16).

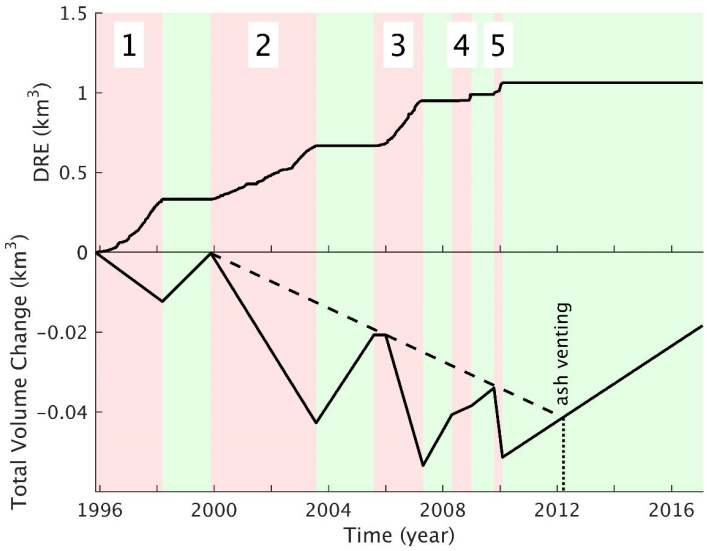

Figure 3.16. Approximation of the cumulative source volume change since the start of the eruption in 1995. The volume extruded during eruptive phase always exceeds the volume replenished during quiet periods. The dashed line marks the onset of renewed extrusions and links it to the timing of the ash-venting episode studied here. Adapted from Neuberg et al. (2018).

3.6 Conclusion

The analysis of the VLP signal observed on 23 March 2012 during an outgassing and ash-venting event on Soufriére Hills Volcano, Montserrat provides a great example how VLP signals can and should be processed. It is of great importance to carry out the proper processing steps in order to retrieve the maximum amount of information from the observed seismograms if we want to interpret source mechanism of VLP signals correctly. I show how forward modelling of the ground displacement can reveal much more details of the source process, since the small changes in displacement are enhanced in the velocity seismogram. Additionally, a moment tensor inversion was performed and estimated the source mechanism to be an isotropic mechanism with a strong shear component. The resulting volume change, potentially caused by CO_2 flushing is estimated to be in the range of $0.6 - 1.1 \times 10^3$ m^3. This volume change can be compared with the one observed at Potocatépetl where Chouet et al. (2005) report the volume change to be $\sim$ 1000 m^3. By combining the results from the restitution process, forward modelling, and the moment tensor inversion we interpret the source mechanism of the event to be a volume opening with a complex, static source displacement and a strong shear component acting in a two-phase motion with a rapid onset and a slower continuation of the motion. Future work around this event could focus on explaining the two phases of the static displacement and based on the results from this and previous chapter, creating a technique where the source parameter uncertainties caused by the station configuration can be estimated using a Bayesian probabilistic source inversion scheme.

Chapter 4

VLP source mechanism in hydrothermal systems

4.1 Introduction

In this chapter I explore a source mechanism for VLP seismicity on White Island, New Zealand (WI) with the local name Whakaari, moving to a hydrothermal volcanic environment, a different volcanic environment compared to Chapter 3. The VLP displacements observed at Whakaari are interesting as they differ from the displacements observed at Montserrat (Figure 4.1). Their oscillatory displacement waveforms have previously been attributed to inflation/deflation source process. In this chapter I will test two different hypotheses which might explain the differences in the observed waveforms. First I investigate whether the oscillatory behaviour of the VLP displacements at Whakaari is an effect of wave propagation in a poroelastic medium. The second hypothesis comes from a simple fluid-solid coupling, where I test if this (damped) oscillation is a product of the impedance difference between the two media. Poroelastic wave propagation has been studied extensively starting with Biot's theory which was developed in a series of papers in 1950's and 1960's (Biot, 1956a,b, 1962), and it is the most popular theory to describe the elastic wave propagation through a fluid-filled porous medium. It has been used in geomechanics, hydrology, and as well in biomechanics, tissue mechanics and cell mechanics. His theory predicts two compressional (P) waves and one shear (S) wave as an effect of the interaction between the fluid and the solid. The fast P-wave has solid and fluid motions in phase while the slow (Biot) P-wave

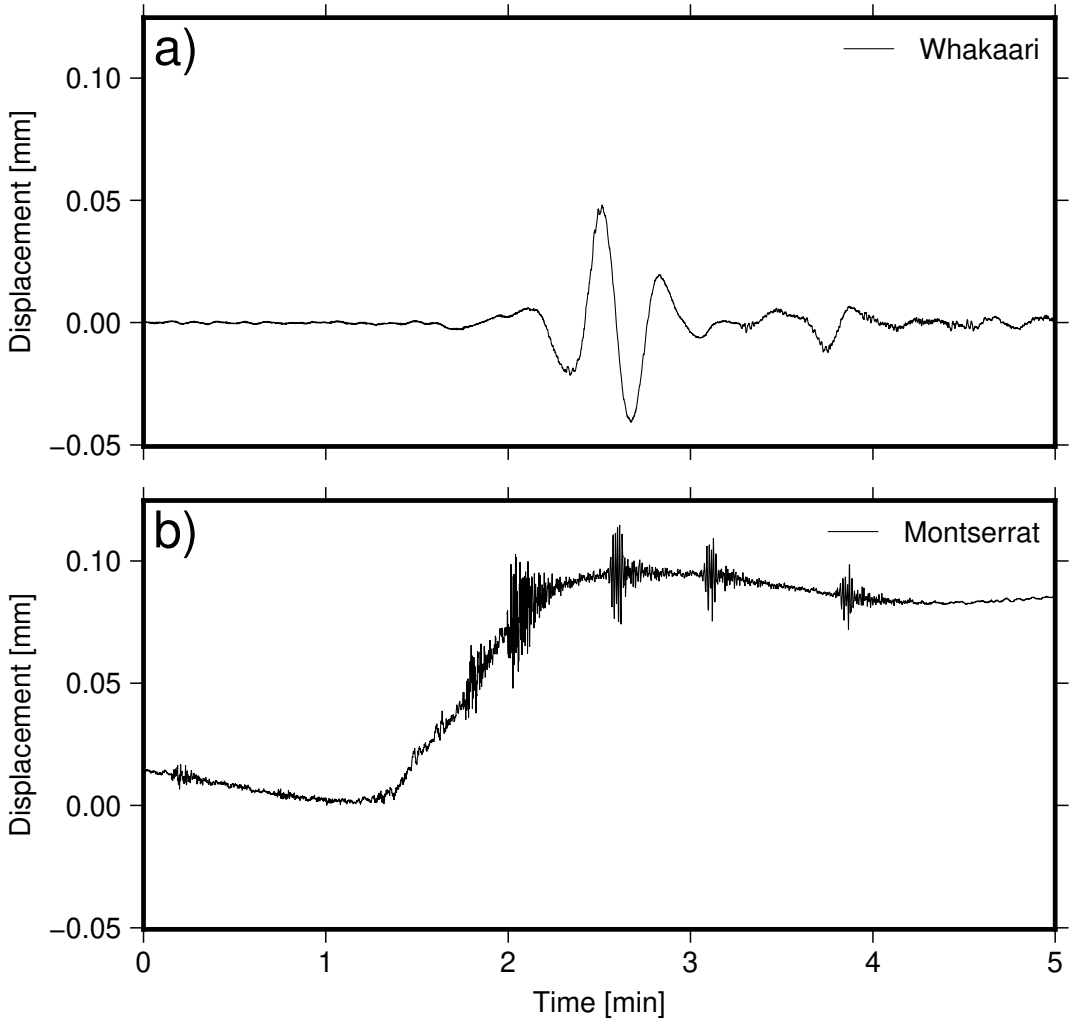

Figure 4.1. Comparison of different VLP displacement waveforms at Whakaari observed on October 3, 2013 and Montserrat observed on March 23, 2012.

has out of phase motions. This phenomenon has been proven experimentally in the 1980s (e.g. Chandler, 1981; Van Der Grinten et al., 1985). Numerical modelling of the poroelastic wave propagation has been done using different kinds of numerical methods, namely finite difference, finite-element, and the spectral element method. Carcione et al. (2010) give an extensive review on the different numerical methods used in computational poroelasticity. As the problem of poroelastic wave propagation has not been studied in the context of volcano-seismology, I focus on the possible effects of the poro-elastic wave propagation in comparison to classical, elastic wave propagation.

In the next section I introduce in detail Biot's theory for poroelastic wave propagation, how I implement it in my numerical scheme, and give results for

my numerical simulations for different scenarios. In Section 4.3 I explore the hypothesis of the fluid-solid coupling as an explanation for the seismic signature of VLPs on Whakaari.

4.2 Poroelastic wave propagation

The initial hypothesis for the description of the observed VLP waveforms on Whakaari was that it is due to wave propagation in a poroelastic medium. Whakaari's geology in terms of porosity characteristics has been studied extensively. Heap et al. (2017) used field and laboratory experiments to measure the permeability of and density/porosity of almost 150 samples collected at Whakaari. Their results give a range of possible porosities, from ~ 0.01 to ~ 0.7, and permeabilities in the range of $\sim 10^{-19}$ to $\sim 10^{-11}$ m^2. Although the values for permeability vary by eight orders of magnitude, I consider them end members of my models, where I incorporate this information into a complex volcano environment with a coupled fluid-solid medium.

The specificity of the poroelastic wave propagation versus the "plain" elastic wave propagation is the existence of an additional, slow P wave which is generated by the relative motion between the solid frame and the fluid in pores. The models presented in this chapter are 2D models in a homogeneous halfspace.

4.2.1 Biot's Theory

The Biot's theory was developed in a series of papers in the 1950's and 1960's (Biot, 1956a,b, 1962) and it is an often used theory to describe the elastic wave propagation through a fluid-filled porous medium. The equation of motion through porous media has been previously derived using multiple methods and here I will recapitulate one of the original methods from Biot (1955, 1956a,b, 1962) using Biot's original variable names. If we consider a volume of the fluid-filled porous system as a cube of unit size, the stress tensor of a porous material is:

$$\begin{bmatrix} \sigma_{xx} + s & \sigma_{xy} & \sigma_{xz} \\ \sigma_{xy} & \sigma_{yy} + s & \sigma_{yz} \\ \sigma_{xz} & \sigma_{yz} & \sigma_{zz} + s \end{bmatrix}. \tag{4.1}$$

We can see that this stress tensor can be separated into two parts. First part, describing the force components acting on the solid part of the unit cube:

$$\sigma = \begin{bmatrix} \sigma_{xx} & \sigma_{xy} & \sigma_{xz} \\ \sigma_{xy} & \sigma_{yy} & \sigma_{yz} \\ \sigma_{xz} & \sigma_{yz} & \sigma_{zz} \end{bmatrix}, \tag{4.2}$$

and the second part describing the forces acting on the fluid part of each face of the cube:

$$\begin{bmatrix} s & 0 & 0 \\ 0 & s & 0 \\ 0 & 0 & s \end{bmatrix}, \tag{4.3}$$

where the scalar s is defined as :

$$s = -\phi p, \tag{4.4}$$

where ϕ is porosity and p is the hydrostatic pressure of the fluid in the pores. We can look at this problem as a general elastic system with conservation properties (Biot, 1955). The solid matrix has compressibility and shearing rigidity, the fluid can be compressible, and the deformation is reversible. This deformation is explained using the strain tensor. The strain components for the solid part are defined as:

$$\begin{aligned} e_{xx} &= \frac{\partial u_x}{\partial x}, \quad e_{xy} = \frac{\partial u_x}{\partial y} + \frac{\partial u_y}{\partial x}, \\ e_{yy} &= \frac{\partial u_y}{\partial y}, \quad e_{xz} = \frac{\partial u_z}{\partial x} + \frac{\partial u_x}{\partial z}, \\ e_{zz} &= \frac{\partial u_z}{\partial z}, \quad e_{yz} = \frac{\partial u_z}{\partial y} + \frac{\partial u_y}{\partial z}, \end{aligned} \tag{4.5}$$

where u_x, u_y, and u_z represent the displacement in the solid. Similarly, we define the components of the strain in the fluid as:

$$\begin{aligned} \varepsilon_{xx} &= \frac{\partial U_x}{\partial x}, \quad \varepsilon_{xy} = \frac{\partial U_x}{\partial y} + \frac{\partial U_y}{\partial x}, \\ \varepsilon_{yy} &= \frac{\partial U_y}{\partial y}, \quad \varepsilon_{xz} = \frac{\partial U_z}{\partial x} + \frac{\partial U_x}{\partial z}, \\ \varepsilon_{zz} &= \frac{\partial U_z}{\partial z}, \quad \varepsilon_{yz} = \frac{\partial U_z}{\partial y} + \frac{\partial U_y}{\partial z}, \end{aligned} \tag{4.6}$$

with U_x, U_y, and U_z representing displacement of the fluid. However, the only significant component for the strain in the fluid is

$$\varepsilon = \varepsilon_{xx} + \varepsilon_{yy} + \varepsilon_{zz}. \tag{4.7}$$

To show the stress-strain relationship of the fluid-solid aggregate we first assume there are no dissipative forces and that we are dealing with the conservative physical system which is in equilibrium at rest (Biot, 1956a). Thus, we can define an elastic potential energy (V) using the seven stress components $\sigma_{xx}, \sigma_{yy}, \sigma_{zz}, \sigma_{xy}, \sigma_{xz}, \sigma_{yz}, s$ which are linear function of the seven strain components $e_{xx}, e_{yy}, e_{zz}, e_{xy}, e_{xz}, e_{yz}, \varepsilon$. Therefore, the elastic potential energy is defined as:

$$2V = \sigma_{xx}e_{xx} + \sigma_{yy}e_{yy} + \sigma_{zz}e_{zz} + \sigma_{xx}e_{xx} + \sigma_{xx}e_{xx} + \sigma_{xx}e_{xx} + s\varepsilon. \tag{4.8}$$

The stress-strain relation is then expressed as:

$$\begin{aligned} \sigma_{xx} &= \frac{\partial V}{\partial e_{xx}}, \quad \sigma_{xy} = \frac{\partial V}{\partial e_{xy}}, \\ \sigma_{yy} &= \frac{\partial V}{\partial e_{yy}}, \quad \sigma_{xz} = \frac{\partial V}{\partial e_{xz}}, \\ \sigma_{zz} &= \frac{\partial V}{\partial e_{zz}}, \quad \sigma_{yz} = \frac{\partial V}{\partial e_{yz}}, \\ s &= \frac{\partial V}{\partial \varepsilon}. \end{aligned} \tag{4.9}$$

We can write the stress-strain relation using a seven-by-seven symmetric matrix with twenty-one independent elastic coefficients (T_{ij}), second order symmetric

tensor (Q_{ij}), and invariant R

$$\begin{bmatrix} \sigma_{xx} \\ \sigma_{yy} \\ \sigma_{zz} \\ \sigma_{xy} \\ \sigma_{xz} \\ \sigma_{yz} \\ s \end{bmatrix} = \begin{bmatrix} & & & T_{ij} & & & Q_{xx} \\ & & & & & & Q_{yy} \\ & & & & & & Q_{zz} \\ & & & & & & Q_{xy} \\ & & & & & & Q_{xz} \\ & & & & & & Q_{yz} \\ Q_{xx} & Q_{yy} & Q_{zz} & Q_{xy} & Q_{xz} & Q_{yz} & R \end{bmatrix} \begin{bmatrix} e_{xx} \\ e_{yy} \\ e_{zz} \\ e_{xy} \\ e_{xz} \\ e_{yz} \\ \varepsilon \end{bmatrix} \tag{4.10}$$

In the case of a statistical isotropy, the potential energy function becomes (Biot, 1955):

$$\begin{aligned} 2V = {} & (A + 2N)(e_{xx} + e_{yy} + e_{zz})^2 + \\ & + N(e_{xy}^2 + e_{xz}^2 + e_{yz}^2 - 4e_{xx}e_{yy} - 4e_{xx}e_{zz} - 4e_{yy}e_{zz}) \\ & + 2Q(e_{xx} + e_{yy} + e_{zz})\varepsilon + R\varepsilon^2. \end{aligned} \tag{4.11}$$

In an isotropic system, the principal stress and principal strain directions coincide, $Q_{ij} = Q$, and we are left with only four distinct elastic constants, A,

N, Q, and R (Biot, 1956a):

$$\begin{aligned}
\sigma_{xx} &= 2Ne_{xx} + Ae + Q\varepsilon \\
\sigma_{yy} &= 2Ne_{yy} + Ae + Q\varepsilon \\
\sigma_{zz} &= 2Ne_{zz} + Ae + Q\varepsilon \\
\sigma_{xy} &= Ne_{xy} \\
\sigma_{xz} &= Ne_{xz} \\
\sigma_{yz} &= Ne_{yz} \\
s &= Qe + R\varepsilon,
\end{aligned} \tag{4.12}$$

with

$$e = e_{xx} + e_{yy} + e_{zz}.$$

We can immediately see the meaning of some of the coefficients in equation (4.12). Without a fluid phase in the system we would have a simple elastic medium, and the coefficients A and N would correspond to Lamé coefficients in the theory of elasticity. The coefficient N corresponds to the shear modulus of the material. The coefficient R is a measure of the pressure required on the fluid to force a certain volume of fluid into the aggregate while the total volume remains the same (Biot, 1956a). The coefficient Q represents the coupling between the volume change of the solid and that of the fluid. If we put the fluid pressure equal to zero, we obtain:

$$\varepsilon = -\frac{Qe}{R}. \tag{4.13}$$

Since the pressure on the solid tends to decrease the porosity in the solid, e and ε must be of opposite sign and therefore Q must be positive. The methods for measurement of the coefficients have been studied by Biot and Willis (1957) and will be discussed on its own in Section 4.2.4.

4.2.2 Wave propagation in porous media

To describe how an elastic wave propagates inside a porous medium we need to look at the relation between stresses and inertial forces. In his theory, Biot

(1956a) introduces the Lagrangian viewpoint and the concept of generalised coordinates. Again, we consider a unit cube of the aggregate, which is small relative to the wavelength of the elastic waves and the size of the pores are small compared to the size of the element. The kinetic function, T, and the dissipation function, D, are described using the six average displacement components $(u_x, u_y, u_z, U_x, U_y, U_z)$ of the solid and fluid respectively. Biot (1956a) derived his equations for the wave propagation in porous media using the Lagrangian formulation

$$\begin{aligned} F^{\mathrm{s}} &= \frac{\partial}{\partial t}\left(\frac{\partial T}{\partial \dot{\mathbf{u}}}\right) + \frac{\partial D}{\partial \dot{\mathbf{u}}} \\ F^{\mathrm{f}} &= \frac{\partial}{\partial t}\left(\frac{\partial T}{\partial \dot{\mathbf{U}}}\right) + \frac{\partial D}{\partial \dot{\mathbf{U}}}, \end{aligned} \tag{4.14}$$

where F^{s} and F^{f} represent the total force acting on the solid and fluid phases respectively, T stands for the kinetic energy of the saturated isotropic porous medium per unit volume, and D represents the dissipation function. The kinetic energy of a unit volume of the bulk material is therefore given by (Biot, 1956a):

$$\begin{aligned} 2T = {} & \rho_{11}\left[\left(\frac{\partial u_x}{\partial t}\right)^2 + \left(\frac{\partial u_y}{\partial t}\right)^2 + \left(\frac{\partial u_z}{\partial t}\right)^2\right] \\ & + 2\rho_{12}\left(\frac{\partial u_x}{\partial t}\frac{\partial U_x}{\partial t} + \frac{\partial u_y}{\partial t}\frac{\partial U_y}{\partial t} + \frac{\partial u_z}{\partial t}\frac{\partial U_z}{\partial t}\right) \\ & + \rho_{22}\left[\left(\frac{\partial U_x}{\partial t}\right)^2 + \left(\frac{\partial U_y}{\partial t}\right)^2 + \left(\frac{\partial U_z}{\partial t}\right)^2\right]. \end{aligned} \tag{4.15}$$

The dissipation function D is

$$2D = b\left[\left(\frac{\partial u_x}{\partial t} - \frac{\partial U_x}{\partial t}\right)^2 + \left(\frac{\partial u_y}{\partial t} - \frac{\partial U_y}{\partial t}\right)^2 + \left(\frac{\partial u_z}{\partial t} - \frac{\partial U_z}{\partial t}\right)^2\right], \tag{4.16}$$

where b is the dissipation factor related to Darcy's coefficient of permeability k, porosity ϕ, and fluid viscosity ν as

$$b = \frac{\nu\phi^2}{k}. \tag{4.17}$$

We can see that the dissipation term in Lagrange's formulation depends on the relative motion between the solid and fluid, which means when there is no motion, the dissipation function D vanishes. The coefficients ρ_{11}, ρ_{12}, and

ρ_{22} act as mass coefficients taking into account that the relative fluid flow through the pores is not uniform (Biot, 1956a). To explain these coefficients, let's consider a one-directional motion in the x-direction. From the Lagrange's equation we derive

$$\begin{aligned} \frac{\partial}{\partial t}\left(\frac{\partial T}{\partial \dot{u}_x}\right) + \frac{\partial D}{\partial \dot{u}_x} &= \frac{\partial^2}{\partial t^2}\left(\rho_{11}u_x + \rho_{12}U_x\right) + b\frac{\partial}{\partial t}\left(u_x - U_x\right) = F_x^{\mathrm{s}} \\ \frac{\partial}{\partial t}\left(\frac{\partial T}{\partial \dot{U}_x}\right) + \frac{\partial D}{\partial \dot{U}_x} &= \frac{\partial^2}{\partial t^2}\left(\rho_{12}u_x + \rho_{22}U_x\right) - b\frac{\partial}{\partial t}\left(u_x - U_x\right) = F_x^{\mathrm{f}}. \end{aligned} \tag{4.18}$$

We can derive the equations for the y- and z-directions in the same way. Now, let's assume there is no relative motion between solid and fluid, i.e.

$$u_x = U_x. \tag{4.19}$$

Consequently, the kinetic energy of the system is described as

$$2T = (\rho_{11} + 2\rho_{12} + \rho_{22})u_x^2. \tag{4.20}$$

We can therefore denote the total density ρ of the fluid-solid aggregate as

$$\rho = (\rho_{11} + 2\rho_{12} + \rho_{22}). \tag{4.21}$$

As we are dealing with a porous medium, we can write this quantity in terms of porosity ϕ and the densities for the solid ρ_{s} and fluid ρ_{f}. Thus, the density of the aggregate is

$$\rho_1 = (1 - \phi)\rho_{\mathrm{s}}, \tag{4.22}$$

and the density of the fluid

$$\rho_2 = \phi\rho_{\mathrm{f}}. \tag{4.23}$$

Therefore, we can express total density ρ as

$$\rho = \rho_1 + \rho_2 = \rho_{\mathrm{s}} + \phi(\rho_{\mathrm{f}} - \rho_{\mathrm{s}}). \tag{4.24}$$

Further, the pressure difference in the fluid per unit length is

$$\begin{gathered} -\frac{\partial p}{\partial x} = \rho_{\mathrm{f}} \frac{\partial^2 u_x}{\partial t^2} \\ \text{or} \\ -\frac{\partial p}{\partial x}\phi = \phi\rho_{\mathrm{f}} \frac{\partial^2 u_x}{\partial t^2} \end{gathered} \tag{4.25}$$

where we can see that the left hand side is the force F_x^f acting on the fluid per unit volume. Taking into account equation (4.23) we get

$$F_x^{\mathrm{f}} = \rho_2 \frac{\partial^2 u_x}{\partial t^2}. \tag{4.26}$$

Still assuming there is no relative motion between fluid and solid equation (4.19), we derive form the second equation in equation (4.18)

$$(\rho_{12} + \rho_{22})u_x = F_x^{\mathrm{f}}. \tag{4.27}$$

Comparing equation (4.27) and equation (4.26) we get

$$\rho_2 = \rho_{12} + \rho_{22}. \tag{4.28}$$

Taking into account equation (4.21) and equation (4.24) we also get

$$\rho_1 = \rho_{11} + \rho_{12}. \tag{4.29}$$

Therefore, the coefficients ρ_{11}, ρ_{22}, and ρ_{12} can be interpreted as the total effective density of the moving solid, the total density of the fluid moving within the solid skeleton, and a coupling coefficient between fluid and solid, respectively. If we assume that the fluid is restrained from flowing, i.e. $U_x = 0$. Then according to the second equation in equation (4.18) we get

$$F_x^{\mathrm{f}} = \rho_{12} \frac{\partial^2 u_x}{\partial t^2}, \tag{4.30}$$

which means that when the solid is accelerated, a force F_x^{f} has to act on the fluid in the opposite direction to prevent any fluid displacement. Therefore, we always must have

$$\rho_{12} < 0. \tag{4.31}$$

Going back to equation (4.18), we can write the force components F_x^{s} and F_x^{f} using stress gradients

$$\begin{aligned} F_x^{\mathrm{s}} &= \nabla \cdot \boldsymbol{\sigma}_x = \frac{\partial \sigma_{xx}}{\partial x} + \frac{\partial \sigma_{xy}}{\partial y} + \frac{\partial \sigma_{xz}}{\partial z} \\ F_x^{\mathrm{f}} &= \nabla_x s = \frac{\partial s}{\partial x}. \end{aligned} \tag{4.32}$$

Combining equation (4.12), equation (4.18), and equation (4.32) we can write out the equation for wave propagation in the x-direction as

$$\begin{aligned} N\nabla^2 u_x + (A+N)\frac{\partial e}{\partial x} + Q\frac{\partial \varepsilon}{\partial x} &= \frac{\partial^2}{\partial t^2}\left(\rho_{11}u_x + \rho_{12}U_x\right) + b\frac{\partial}{\partial t}\left(u_x - U_x\right) \\ Q\frac{\partial e}{\partial x} + R\frac{\partial \varepsilon}{\partial x} &= \frac{\partial^2}{\partial t^2}\left(\rho_{12}u_x + \rho_{22}U_x\right) - b\frac{\partial}{\partial t}\left(u_x - U_x\right). \end{aligned} \tag{4.33}$$

The vector form for the wave propagation in a fluid saturated isotropic porous medium is therefore

$$\begin{aligned} N\nabla^2 \vec{u} + \nabla\left[(A+N)\,e + Q\varepsilon\right] &= \frac{\partial^2}{\partial t^2}\left(\rho_{11}\vec{u} + \rho_{12}\vec{U}\right) + b\frac{\partial}{\partial t}\left(\vec{u} - \vec{U}\right) \\ \nabla\left(Qe + R\varepsilon\right) &= \frac{\partial^2}{\partial t^2}\left(\rho_{12}\vec{u} + \rho_{22}\vec{U}\right) - b\frac{\partial}{\partial t}\left(\vec{u} - \vec{U}\right). \end{aligned} \tag{4.34}$$

As noted by Biot (1956a), an acceleration of the solid matrix without any motion of fluid causes a pressure gradient in the fluid due to the coupling coefficient ρ_{12}. It is also important to note that Biot assumed that the fluid flow is of the Poiseuille type and that this assumption restricts the solution domain to low frequency range. As in this work I am describing waves in very-low frequency range I can continue with this assumption and that the signals we examine will always have frequency lower than the "critical" frequency (f_{c}) defined as

$$f_{\mathrm{c}} = \frac{\nu\pi}{4\rho_{\mathrm{f}}d^2}, \tag{4.35}$$

where d is the diameter of the pores.

4.2.3 Numerical modelling

I implemented numerical models using the Finite Element Method (FEM) software COMSOL Multiphysics (COMSOL Multiphysics v5.5). As the software itself does not have a module for calculating wave propagation in the poroelastic

medium, I used the 'general form partial differential equation (PDE)' module where the PDEs are defined as second order wave equations. The general form PDE interface in COMSOL requests the equations to be written in the form of

$$e_a \frac{\partial^2 \boldsymbol{u}}{\partial t^2} + d_a \frac{\partial \boldsymbol{u}}{\partial t} + \nabla \cdot \Gamma = f, \tag{4.36}$$

where $\boldsymbol{u}$ is a vector with our solid and fluid displacements, e_a is mass coefficient, d_a is damping coefficient and $\nabla \cdot \Gamma$ is the conservative flux (Appendix B). As I want to end up with the four particle displacement components (u_x, u_y, U_x, U_y) for the two-phase isotropic media in x-y plane, we can re-write the stress-strain relationship from equation (4.12) as

$$\begin{bmatrix} \sigma_{xx} \\ \sigma_{yy} \\ \sigma_{xy} \end{bmatrix} = \begin{bmatrix} (2N+A) & A & 0 \\ A & (2N+A) & 0 \\ 0 & 0 & N \end{bmatrix} \begin{bmatrix} \dfrac{\partial u_x}{\partial x} \\ \dfrac{\partial u_y}{\partial y} \\ \dfrac{\partial u_x}{\partial y} + \dfrac{\partial u_y}{\partial x} \end{bmatrix} + \varepsilon \begin{bmatrix} Q \\ Q \\ 0 \end{bmatrix} \tag{4.37}$$

for the solid phase and

$$s = Q\left(\frac{\partial u_x}{\partial y} + \frac{\partial u_y}{\partial x}\right) + R\varepsilon \tag{4.38}$$

for the fluid phase. Further, assuming constant values for densities $\rho_{11}, \rho_{22}, \rho_{12}$, equation (4.34) can be re-written as

$$\begin{aligned} \rho_{11}\frac{\partial^2 \vec{u}}{\partial t^2} + \rho_{12}\frac{\partial^2 \vec{U}}{\partial t^2} + b\frac{\partial}{\partial t}\left(\vec{u} - \vec{U}\right) &= \nabla \cdot \boldsymbol{\sigma} \\ \rho_{12}\frac{\partial^2 \vec{u}}{\partial t^2} + \rho_{22}\frac{\partial^2 \vec{U}}{\partial t^2} - b\frac{\partial}{\partial t}\left(\vec{u} - \vec{U}\right) &= \nabla s \end{aligned} . \tag{4.39}$$

Re-arranging this equation we get

$$\begin{bmatrix} \dfrac{\partial^2 \vec{u}}{\partial t^2} \\ \dfrac{\partial^2 \vec{U}}{\partial t^2} \end{bmatrix} - \begin{bmatrix} D_{22} & -D_{12} \\ -D_{12} & D_{11} \end{bmatrix} \begin{bmatrix} \nabla \cdot \boldsymbol{\sigma} - b\dfrac{\partial}{\partial t}\left(\vec{u} - \vec{U}\right) \\ \nabla s + b\dfrac{\partial}{\partial t}\left(\vec{u} - \vec{U}\right) \end{bmatrix} = 0, \tag{4.40}$$

where D_{ii} are normalised density coefficients described as

$$\begin{aligned} D_{11} &= \frac{\rho_{11}}{\rho_{11}\rho_{22} - \rho_{12}^2} \\ D_{12} &= \frac{\rho_{12}}{\rho_{11}\rho_{22} - \rho_{12}^2}. \\ D_{22} &= \frac{\rho_{22}}{\rho_{11}\rho_{22} - \rho_{12}^2} \end{aligned} \tag{4.41}$$

In the x-y plane, the divergence of the stress tensor equals $\nabla \cdot \boldsymbol{\sigma}_x = \partial_x \sigma_{xx} + \partial_y \sigma_{xy}$, $\nabla \cdot \boldsymbol{\sigma}_y = \partial_x \sigma_{xy} + \partial_y \sigma_{yy}$, therefore the expression for the four particle displacement components can be expressed as

$$\begin{aligned} &\frac{\partial^2 u_x}{\partial t^2} + b\left(D_{22} + D_{12}\right)\left(\frac{\partial u_x}{\partial t} - \frac{\partial U_x}{\partial t}\right) - D_{22}\left(\frac{\partial \sigma_{xx}}{\partial x} + \frac{\partial \sigma_{xy}}{\partial y}\right) + D_{12}\frac{\partial s}{\partial x} = 0 \\ &\frac{\partial^2 u_y}{\partial t^2} + b\left(D_{22} + D_{12}\right)\left(\frac{\partial u_x}{\partial t} - \frac{\partial U_x}{\partial t}\right) - D_{22}\left(\frac{\partial \sigma_{xy}}{\partial x} + \frac{\partial \sigma_{yy}}{\partial y}\right) + D_{12}\frac{\partial s}{\partial x} = 0 \\ &\frac{\partial^2 U_x}{\partial t^2} - b\left(D_{11} + D_{12}\right)\left(\frac{\partial u_x}{\partial t} - \frac{\partial U_x}{\partial t}\right) + D_{12}\left(\frac{\partial \sigma_{xx}}{\partial x} + \frac{\partial \sigma_{xy}}{\partial y}\right) - D_{11}\frac{\partial s}{\partial x} = 0 \\ &\frac{\partial^2 U_y}{\partial t^2} - b\left(D_{11} + D_{12}\right)\left(\frac{\partial u_y}{\partial t} - \frac{\partial U_y}{\partial t}\right) + D_{12}\left(\frac{\partial \sigma_{xy}}{\partial x} + \frac{\partial \sigma_{yy}}{\partial y}\right) - D_{11}\frac{\partial s}{\partial x} = 0 \end{aligned} \tag{4.42}$$

It is worth noting that we can put an external force component on the right hand side of equation (4.42). It is common practice to use an excitation function with spatial and time dependence. In my models I use Dirichlet boundary condition as a prescribed time-dependent displacement at the source.

4.2.4 Biot's coefficients

The coefficients N, A, Q, and R in equation (4.37) and equation (4.37) are still not defined. Previously I have mentioned that coefficient N equals the shear modulus of the bulk material. To define the other coefficients Biot and Willis (1957) use the combination of measurements of shear modulus, jacketed and unjacketed compressibility of the porous solid, and an unjacketed coefficient of fluid content. The jacketed compressibility (κ) test requires a specimen of the material to be enclosed in a thin impermeable jacket and then subjected to an external fluid pressure, while the pore fluid is allowed to escape freely through a tube (Biot and Willis, 1957). Usually it is done on a dry specimen, however Biot and Willis (1957) note that the dry specimen may not exhibit the same

properties as the saturated one. The jacketed compressibility is the inverse of the bulk modulus (K):

$$\kappa = \frac{1}{K} = \frac{1}{\lambda + \frac{2}{3}\mu} \tag{4.43}$$

For the unjacketed compressibility (δ) test the specimen is submerged into a fluid to which an external pressure is applied. It is an inverse of the unjacketed bulk modulus, i.e. the bulk modulus of the solid material composing the porous solid (K_s)

$$\delta = \frac{1}{K_s} \tag{4.44}$$

These two values describe Biot's coefficient (α)

$$\alpha = 1 - \frac{\delta}{\kappa} = 1 - \frac{K}{K_s}. \tag{4.45}$$

Biot and Willis (1957) show that α cannot be smaller than porosity and larger than unity. When looking at unconsolidated soils, the value for α is often approximated to be 1, as the unjacketed compressibility in this case would be much smaller than the jacketed compressibility and therefore $\frac{\delta}{\kappa} \approx 0$.

While the values for the bulk modulus K can be found in literature or calculated using Young's modulus (E) and Poisson's ratio (ν), the values for the bulk modulus of the composite (K_s) have to be obtained using different methods. I use the method by Selvadurai et al. (2019) where he proposes using a multi-phase theory developed for estimating effective properties of composite elastic materials to estimate the compressibility of the solid material phase. For low-permeability Cobourg Limestone, Selvadurai (2019) shows that we can use the estimates of Voight (1928) and Reuss (1929) to calculate the bulk (K_s) and shear (G_s) moduli of the multi-phasic solid material. The Voigt estimate is calculated by using

$$\begin{aligned} K_s^V &= \sum_i^n V_i (K_s)_i \\ G_s^V &= \sum_i^n V_i (G_s)_i \end{aligned} \tag{4.46}$$

and the Reuss estimate by using

$$K_s^R = \left[\sum_i^n \frac{V_i}{(K_s)_i}\right]^{-1}$$
$$G_s^R = \left[\sum_i^n \frac{V_i}{(G_s)_i}\right]^{-1} \tag{4.47}$$

The i in the estimates stands for the mineralogical composition of the material, and V_i for the volumetric fraction of that composition. To narrow down the wide range of these estimates we can use Voigt-Reuss-Hill (Hill, 1952) estimate which takes the average of Voigt and Reuss estimates. For the White Island andesite, the mineral composition is taken from Heap et al. (2015) and shown in Table 4.1.

Table 4.1. Mineralogical fractions for Whakaari andesite (from Heap et al. (2015))

MINERAL	V_i	K_s (GPa)	Reference
plagioclase	37 %	75	Brown et al. (2016)
K-feldspar	14 %	52	Brown et al. (2016)
pyroxene	10 %	0.7	Chai et al. (1997)
cristobalite	17 %	16.3	Pabst and Gregorová (2013)
amorpheus phases, volcanic glass, opal-A	25 %	≈ 40	Pabst and Gregorová (2013)
gypsum	4%	44	Watt (1979)
jarosite	3 %	56	Xu et al. (2010)
haematite	1%	205	Zhang et al. (2020)
Voigt-Reuss-Hill estimate	100 %	27	

Further, Biot (1962) introduces a coefficient M

$$M = \frac{1}{\gamma + \delta - \dfrac{\delta^2}{\kappa}} \tag{4.48}$$

where the coefficient of the fluid content, γ, gives the relationship between porosity (ϕ), fluid compressibility (c), and the unjacketed compressibility (δ) as

$$\gamma = \phi(c - \delta). \tag{4.49}$$

Therefore the coefficients N, A, Q, and R can be expressed as (Biot, 1962):

$$\begin{aligned} N &= \mu \\ A &= \lambda + M(\alpha - \phi)^2 \\ Q &= \phi(\alpha - \phi)M \\ R &= \phi^2 M. \end{aligned} \tag{4.50}$$

This formulation will make it easier to compare the elastic and poroelastic case, as well as model coupled elastic-poroelastic examples, as by setting the coefficients M and ϕ to zero, we get pure elastic wave propagation.

4.2.5 Poroelastic vs. elastic wave propagation

Next we explore the difference in waveforms of poroelastic and elastic wave. The way the equations in (4.50) are set up, the comparison between the two cases is made fairly simple as minimising porosity and the coefficient M we obtain elastic wave propagation. I determine the Lamé parameter λ, shear modulus N, and Young's modulus E using v_p and v_s velocities. As the wavelengths of my signals are very large, I can approximate the model space as homogeneous. Jolly et al. (2012) estimated seismic velocities in the shallower region of Whakaari volcano by use of high-impact sand-bag drops from a helicopter as $v_\mathrm{p} = 2.2$ km/s. It is in the range of v_p velocities obtained by Heap et al. (2015) using uniaxial and triaxial compression experiments (v_p between 1.2 and 5 km/s). I prefer the Jolly et al. (2012) estimates as their approach brings less uncertainty into my model than approximating a large volume by using an individual value for the Young's modulus. Heap et al. (2015) evaluate the range for porosities to be between 5% and up to 50% for the ash tuff deposits. It is worth noting that they also observe slower velocities in rock samples with high porosity. In this hydrothermal system it is also very important to distinguish which fluid fills the porous space in the rock. As I assume a binary $H_2O - CO_2$ system in this environment, I use values for density, fluid compressibility, and fluid viscosity for the two end members of this binary system, CO_2 and H_2O (Table 4.2). The compressibility of CO_2 is much larger than that of water and rock. Water compressibility is of the order of 4.5×10^{-10} Pa^{-1} (Vilarrasa et al.,

2010), compressibility of the rock matrix in the range $2\times10^{-10}-4\times10^{-11}$ Pa^{-1}, and CO_2 compressibility is one to two orders of magnitude greater, from 10^{-9}- -10^{-8} Pa^{-1} (Vilarrasa et al., 2010; Span and Wagner, 1996). The density values for the two end members, $\rho_{CO_2} = 380$ kg/m^3 (Span and Wagner, 1996) and $\rho_{H_2O} = 947$ kg/m^3 (Wagner and Kretzschmar, 2008), are taken for the temperature of 400 K and pressure of 20 MPa, conditions appropriate for the source depth at Whakaari. From relations shown in equation (4.41) we see that the normalised density coefficients D_{ii} used in equation (4.42) relate to density coefficients ρ_{11}, ρ_{22}, and ρ_{12}. The coefficient ρ_{12} can be directly calculated using

$$\rho_{12} = -\phi\rho_{\mathrm{f}}(\tau - 1), \tag{4.51}$$

where τ represents the tortuosity. The tortuosity is a geometrical term defined by the ratio of the average length of the geometric flow path through the medium and the shortest (straight line) path through the medium. Therefore, the values for τ are commonly between 1 (direct path) and 3 (Dullien, 2012). Combining equation (4.22) and equation (4.23) with equation (4.29) and equation (4.28) respectively,

$$\begin{aligned}(1-\phi)\rho_{\mathrm{s}} &= \rho_{11} + \rho_{12}\\ \phi\rho_{\mathrm{f}} &= \rho_{22} + \rho_{12},\end{aligned} \tag{4.52}$$

we can see that by defining the coupling coefficient, ρ_{12}, between the fluid and solid phases, we can easily calculate coefficients ρ_{11} and ρ_{22}.

Table 4.2. Values for the compressibility, density, and viscosity of CO_2 and H_2O. The values are obtained for temperature of 400 K and pressure of 20 MPa.

Variable	CO_2	H_2O
compressibility (c) Pa^{-1}	$5.6 \times 10^{-}9$	5.1×10^{-10}
density (ρ_{f}) kg/m^3	480	947
viscosity (ν_d) $\mathrm{Pa}\cdot\mathrm{s}$	3.17×10^{-5}	22.37×10^{-5}

Table 4.3. Values for elastic/poroelastic coefficients relating to the solid frame used in equation (4.50). The Young's modulus, derived from estimates of seismic velocities is 8.5 GPa and Poisson's ratio is 0.25

Description	Coefficient	Value
Porosity	ϕ	0.3
Jacketed compressibility	δ	3.7037×10^{-11} 1/Pa
Unjackated compressibility	κ	1.76×10^{-10} 1/Pa
Lame parameter	λ	3.4×10^{9} Pa
Shear modulus	N	3.4×10^{9} Pa
Biot's coefficient A	A	3.42×10^{9} Pa
Biot's coefficient P ($P = A + 2N$)	P	1.02×10^{10} Pa
Biot's coefficient Q	Q	4.74×10^{6} Pa
Biot's coefficient R	R	5.99×10^{6} Pa

The model has a rectangular spatial domain of 20×20 km^2, with displacement constraints on the sides of the domain and the free surface condition on the top of the domain. Free surface condition in the poroelastic medium is described as:

$$\begin{aligned} n \cdot \boldsymbol{\sigma} &= 0 \\ p &= 0, \end{aligned} \tag{4.53}$$

where n is the unit vector normal to the free surface and p is the fluid pressure. The topography is not included. I keep the model fairly simple to isolate the characteristics of the porous medium.

To validate how I set-up my equations in the COMSOL PDE interface, I first compare a simple elastic model with a model created using the COMSOL Structural Mechanics module. The source is a spherical void with a radius of 50 m, located at 1.5 km depth mimicking the source depth from Caudron et al. (2018); Jolly et al. (2017). By using a time-dependent prescribed displacement at the source I simulate a pressurisation of the source. As a source-time function I use a Gaussian function with a dominant frequency of 0.5 Hz. All of the following synthetic seismograms are obtained from a receiver at the surface, directly above the source (Figure 4.2).

Figure 4.3 shows the set-up validation for the elastic case. It shows a very good match, therefore my choice how to set up the boundary conditions, the Flux/Source option for a Neumann boundary condition for the free surface, and the choice of Dirichlet boundary conditions for the left, right, and bottom

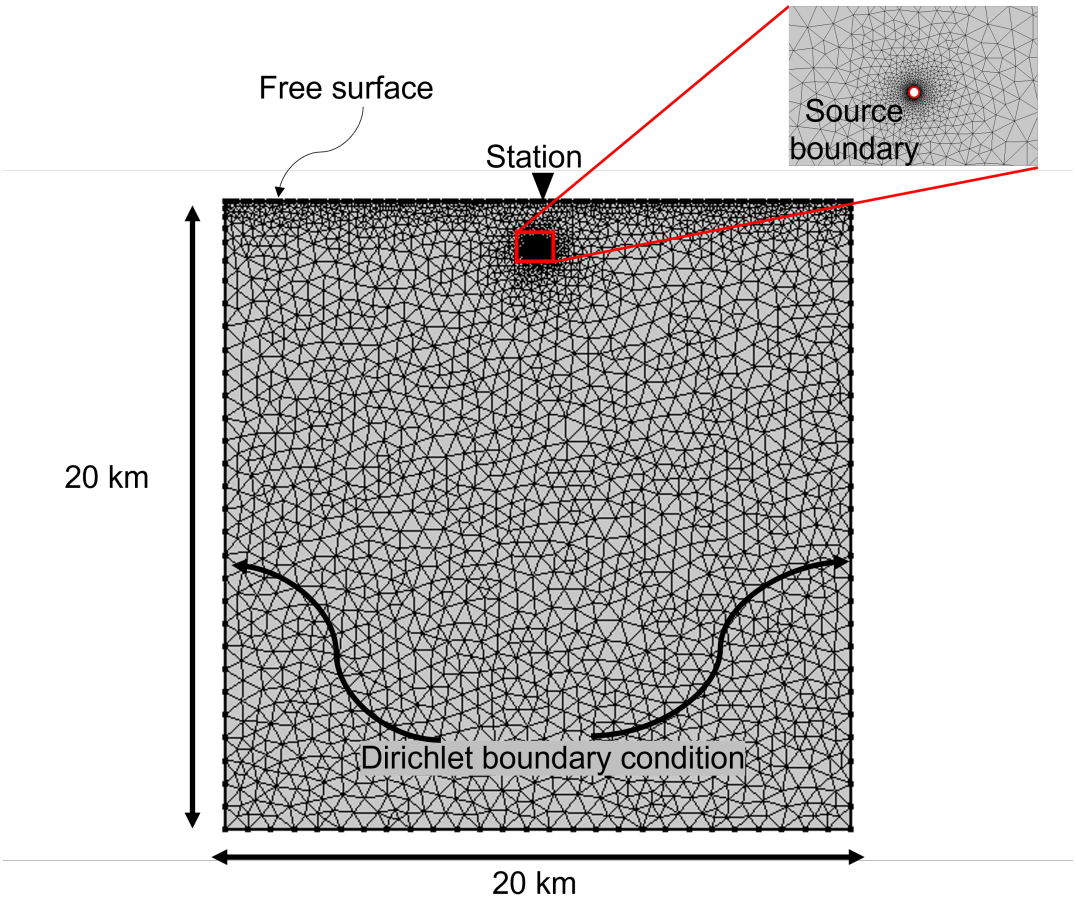

Figure 4.2. Mesh for the numerical domain of the models. The top boundary is a free surface and the Dirichlet boundary condition on the sides and bottom constrained the displacement in a direction normal o the boundary. The station is located at the free surface and is directly above the source

boundary of the model, which constrains the displacement in a direction normal to the boundary. The lack of absorbing or perfectly matched layers is a drawback of my models, however as the goal of my models is not in creating the best numerical scheme to study poroelastic waves, rather to see the effects of certain coefficients, the model set up is sufficient for the purpose.

The initial poroelastic modelling was done using values shown in Tables 4.2 and 4.3. The solid particle displacements of the poroelastic waves (equation (4.42)) where the medium is saturated either with H_2O or with CO_2 are compared with the purely elastic case (Figure 4.4). What we can observe is that the poroelastic waves travel faster than the purely elastic one and they have smaller amplitudes. The faster arrival can be explained as the saturated

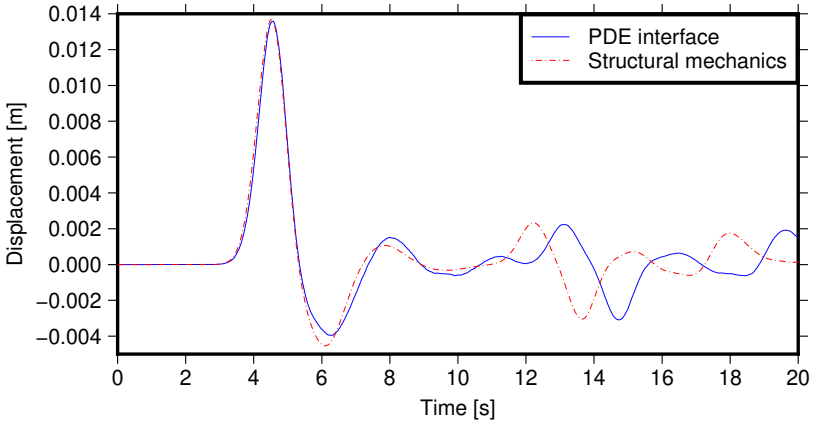

Figure 4.3. Displacement seismograms comparing the PDE interface (blue line) and Structural mechanics module (dashed red line). We can see that our models are set up properly.

porous rock is stiffer than non-saturated rock (e.g. Rice, 1975; Makhnenko and Labuz, 2016).

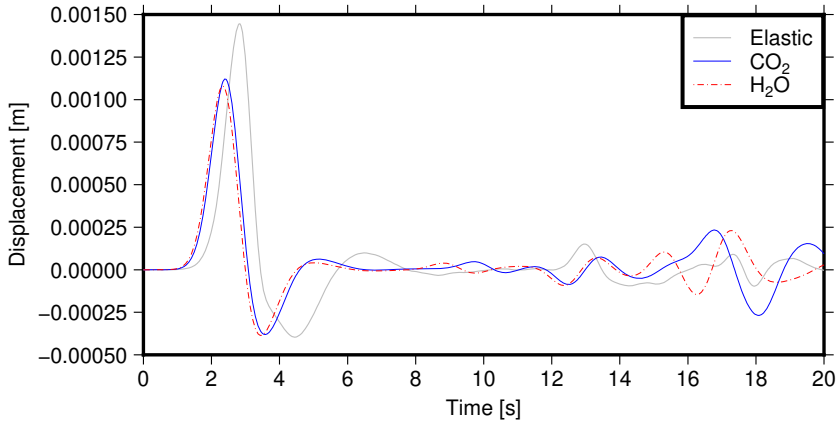

Figure 4.4. The solid particle vertical component displacement seismograms comparing the poroelastic and elastic waves. The fastest arrival is for the case where the pores are saturated with water (dashed red) then with CO_2 (blue), and the slowest arrival is for the elastic case (gray).

4.2.6 Influence of porosity and permeability

As mentioned before there is a large span of possible values for the permeability from $\sim 10^{-11}$ to 10^{-19} m^2 and porosity can vary from 1 % to 70 % (Heap et al., 2017). Equation 4.17 showed that the coefficient b, which influences the dissipation term, is the ratio of the product of fluid viscosity with porosity and the permeability of the porous rock. Therefore, it is of interest to examine

how it affects our waveforms. The models are run with different values for the permeability: 10^{-9}, 10^{-11}, 10^{-14}, and 10^{-19} m^2. The lowest value for the permeability, 2 orders of magnitude higher than the ones estimated by Heap et al. (2017), is chosen as a comparison to studies by Zhang et al. (2014) and Moradi et al. (2015) where they examined for which value of b the slow P-wave dissipates. The porosities used in these models are 10 %, 20 %, 30 %, and 40 %.

Figure 4.5 shows the results for models with different permeabilities and a constant porosity of 0.2 compared with the elastic case. We see that for the CO_2 case the change in permeability has a bigger effect than for the H_2O case. However, the slow-P wave is not seen even for the highest values of permeability.

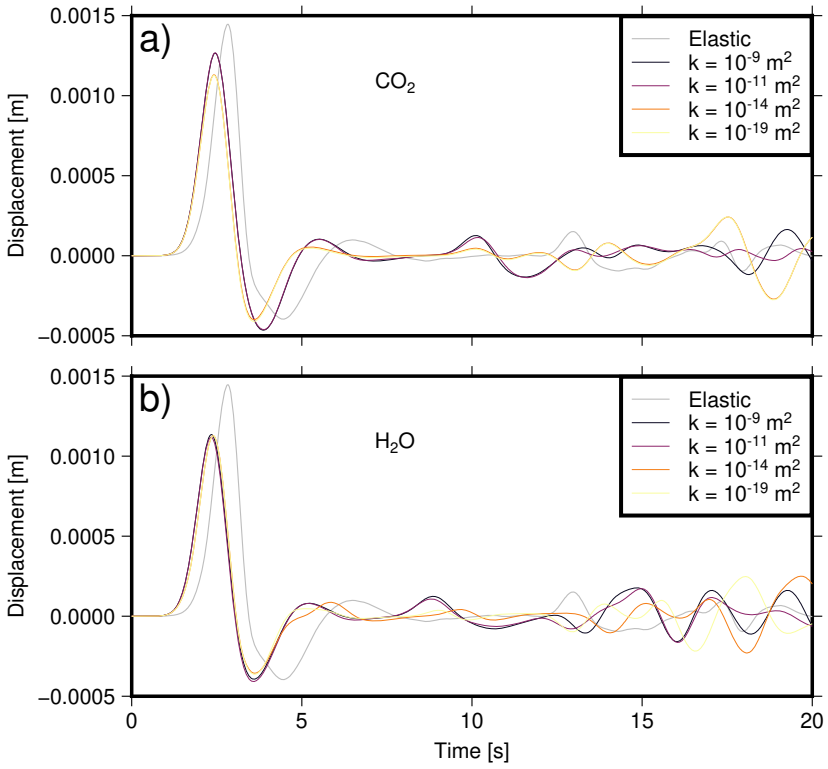

Figure 4.5. Solid particle displacement (vertical component) seismograms showing the effect of the permeability (k) on the poroelastic waves when the rock is saturated with (a) CO_2 or (b) H_2O. The porosity is constant and is set to 0.2. The oscillations after t=10s are due to reflections.

Further, to fully asses the effect of both porosity and permeability I ran models across the full range of possible porosity and permeability values (Figure 4.6). We notice that for the lowest values of permeability ($k = 10^{-14},\ 10^{-19}$ m^2) the

waveforms do not differ regardless of what the medium is saturated with, and porosity does not have any effect. They do however, differ from the elastic waveform where the amplitudes of the poroelastic waves become smaller with larger porosity values. For the largest value of permeability ($k = 10^{-11}$ m^2) all three waveforms differ from each other and the amplitudes for the CO_2 case equal the ones of the elastic waves (Figure 4.6).

Although we see the effect of porosity and permeability on our waveforms, the previously reported influence of coefficient b on the slow P-wave is not seen as we do not observe one. However, this can be explained by the dominant frequency of my input signal.

4.2.7 Frequency dependent input signal

A main aspect that separates my research from previous studies on the poroelastic wave propagation is the frequency content of my signal. I have mentioned already the assumption that the source frequency should be smaller than the critical frequency for the low-frequency Biot's case (equation (4.35)). While past studies of this problem usually focused on reservoir geophysics, where the input frequencies of the signal are often in the order of kHz, the volcano signals are less than 1 Hz. Therefore, it is of interest to look at the frequency dependence of the input signal and the observed slow Biot P-wave. To do this, I use the analytical solutions to the poroelastic wave equations (Dai et al., 1995). The source is a point explosion with time component described by a Gaussian function with 10 Hz, 5 Hz, 1 Hz, 0.5 Hz, 0.1 Hz, and 0.05 Hz dominant frequency, respectively. The station is positioned 1.5 km away from the source, resembling the source-receiver distance from the rest of the models. The characteristics of the medium (Biot coefficients) are the same as in the previous models in Section 4.2.5. Figure 4.7 shows the resulting traces of the solid particle velocities. For frequencies $f_0 = 10$ Hz and $f_0 = 5$ Hz we can clearly see the slow P-wave. The amplitudes of the slow P-wave for 'low' frequencies (1 - 10 Hz) are higher than for the fast P-wave (Karpfinger et al., 2009). We can see that when the source-receiver distance becomes closer to, and then smaller than one wavelength of the signal, the near field term becomes dominant, converging to elastic wave propagation.

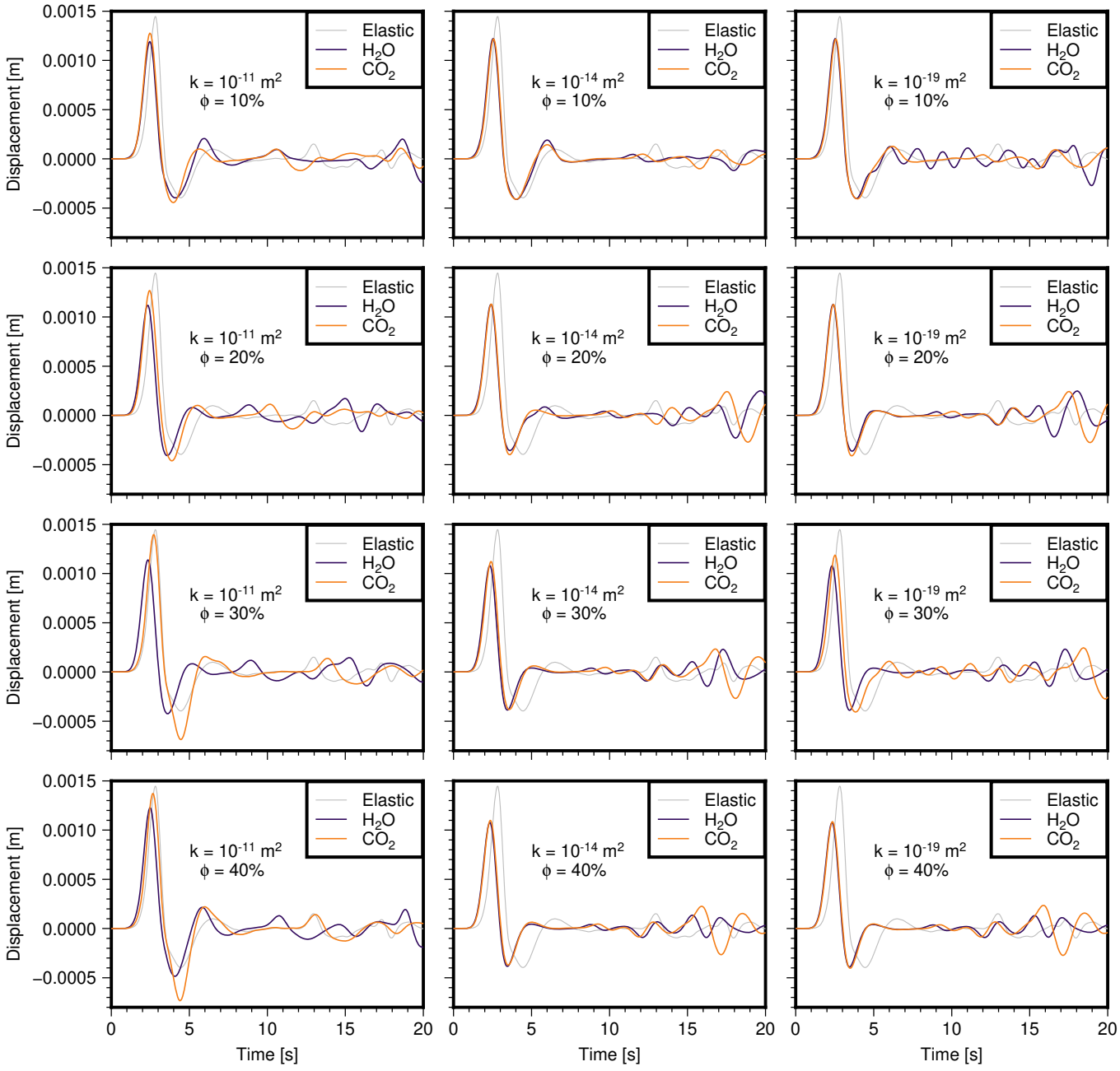

Figure 4.6. Solid particle displacement seismograms showing the influence of porosity and permeability on waveforms when the material is saturated with CO_2 (orange) and H_2O (blue). The values for the permeability are 10^{-11} m^2 (left column), 10^{-14} m^2 (centre column), and 10^{-19} m^2 (right column). The seismograms are shown for porosities of 10, 20, 30, and 40 %.

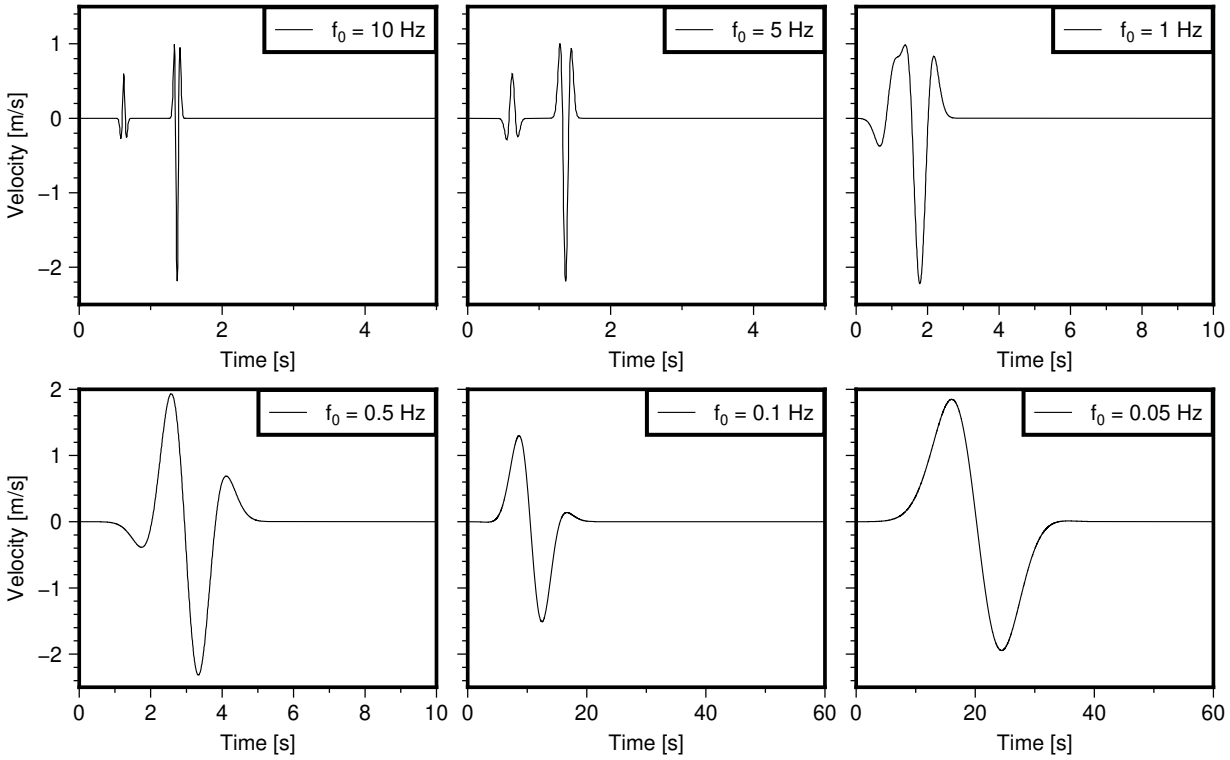

Figure 4.7. Influence of the dominant frequency on the poroelastic solid particle velocity waveform. I vary the source frequency between 10 Hz and 0.05 Hz. The slow P-wave is observable when the source-receiver distance is greater than one wavelength of the signal. For distances smaller than the signal wavelength, the near field dominates and we can observe only one P-wave arrival.

4.2.8 Two-layer model

Although we have now discarded the possibility that the slow P-wave can be an explanation for the observed VLP waveforms on Whakaari, we still need to investigate a more complex scenario of a two-layered model, with the poroelastic layer above the elastic one. The source depth is again at 1.5 km depth and the poroelastic layer is 1 km thick. The computational domain is again 20×20 km with the same external boundary conditions as in the previous models. A continuity condition is set on the boundary between elastic and poroelastic domains. The fluid in the poroelastic domain is again either CO_2 or H_2O with the same properties as in earlier examples. The results are compared with the case where both domains are either completely poroelastic or elastic. Figure 4.8 shows the results for the two scenarios. When the poroelastic domain is saturated with CO_2, there is no significant waveform change when compared

with the completely poroelastic case (Figure 4.8a). However, when the fluid used is H_2O, the waveform resembles the elastic one, apart from the amplitude which matches the purely poroelastic case.

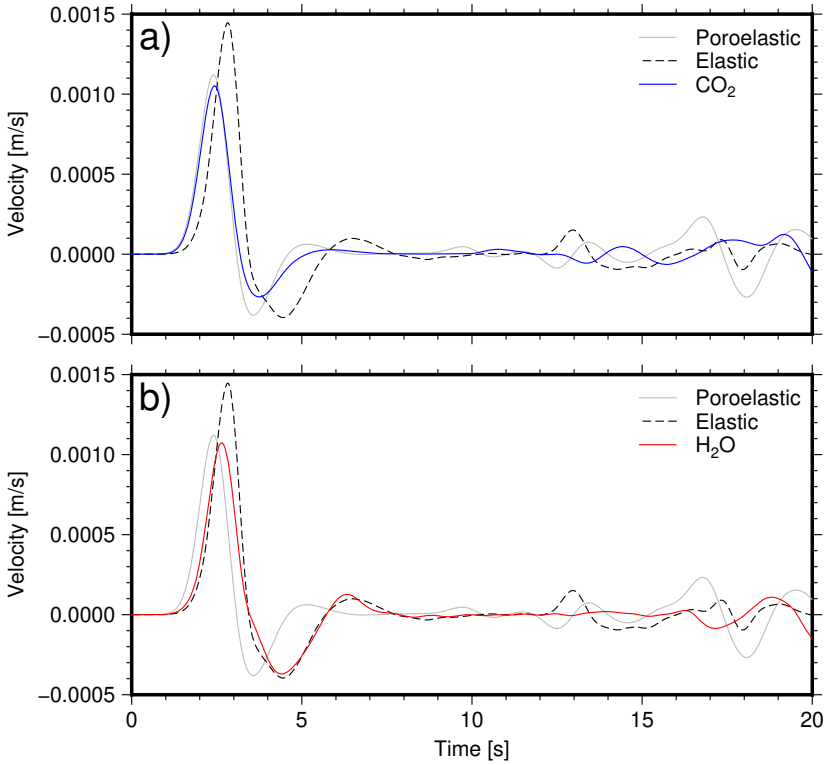

Figure 4.8. Two layered case - Poroelastic layer is on top of the elastic layer. The poroelastic layer is saturated with (a) CO_2 or (b) with water. The results are compared with purely poroelastic medium (grey line) and purely elastic case (black dashed line).

While in previous results the poroelastic wave was faster when the porous medium is saturated with water compared to CO_2, for the two layered case we have the opposite situation. It is also interesting that even though the wavelength of our signal is several kilometres and the width of the poroelastic layer is only 1 km, it considerably affects the waveforms, as well as the amplitudes.

4.3 Source oscillation

The second hypothesis is that the observed oscillatory behaviour of the displacements is an effect of the fluid-solid interaction. In this case, the source of the VLP signal is situated in a fluid domain which is surrounded by an elastic solid. I analyse the influence of the different fluid properties (CO_2 vs H_2O) as well as the influence of the fluid domain geometry. This modelling was again done using FEM software COMSOL Multiphysics, however this time I could use the built-in multiphysics named *Acoustic-Solid interaction, Time explicit interface*, which combines *Pressure Acoustics, Time Explicit* and *Elastic Waves, Time Explicit* together with the *Acoustic-Structure Boundary, Time Explicit* multiphysics coupling. This way we can solve a multiphysics phenomenon where the acoustic pressure causes a fluid load on the solid domain, and the structural acceleration acts on the fluid domain as a normal acceleration across the fluid-solid boundary.

4.3.1 Source excitation

Stix and de Moor (2018) define two end member types of phreatic eruptions: type 1, where a deep sealed hydrothermal system is fed by magmatic gasses and produces enough overpressure to force an explosive eruption, and type 2, where magmatic gasses are supplied through an open vent to the shallow hydrothermal system, vapourising the liquid which drives the phreatic eruption (Figure 4.9). Jolly et al. (2018) consider that the VLP seismicity is caused by the failure of the magmatic carapace. However, we can also speculate that the failure of the carapace is not the trigger for the VLP seismicity, rather, it releases the gasses into the hydrothermal system, which can then lead to the rapid and sudden vapourisation of water. Due to the explosive properties of water, a phase change between liquid water and vapour in the shallow region of volcanic system may produce a violent explosion. If there is a rapid pressure or temperature change it can bring the system beyond the liquid spinodal into the unstable field, resulting in a spinodal decomposition, a rapid and explosive phase separation (Thiery and Mercury, 2009a). For a pure water system, the source conditions at Whakaari do not allow for this violent phase transition (Figure 4.10a), however, if there is even a small mole fraction of dissolved gasses such as CO_2, the explosive potential of the system increases significantly

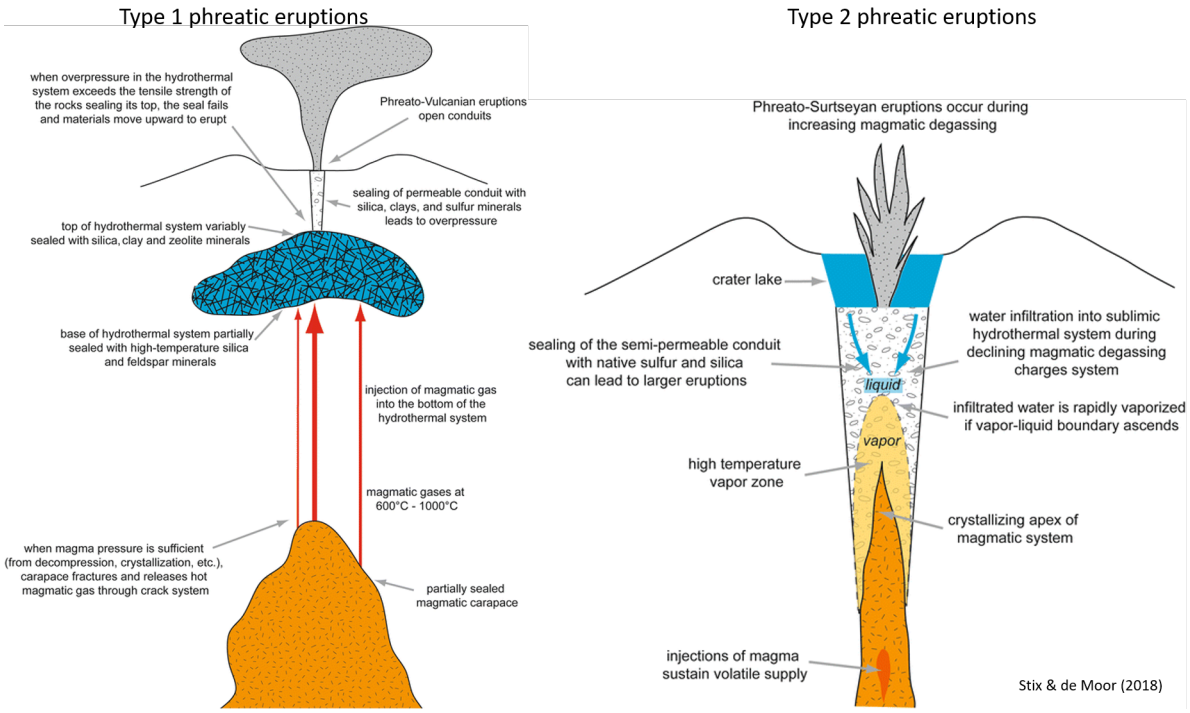

Figure 4.9. Type 1- when the magma pressure in a partially sealed magmatic carapace is sufficient, the carapace breaks and releases hot magmatic gasses injecting the bottom of the hydrothermal system. Type 2 - Increasing magmatic gas input into the lake raises the vapour–liquid boundary, resulting in vaporization of confined liquid water, generating volume change, pressurization, and eruption. Adapted from Stix and de Moor (2018).

(Thiery and Mercury, 2009b) meaning a smaller pressure drop can lead to a violent explosive phase changes (Chouet and Matoza, 2013b). Therefore, in this section I test whether the oscillatory behaviour of our observed VLP waveforms could be caused by the oscillations of the fluid source region post this violent phase transition (Figure 4.10b).

4.3.2 Numerical model

The computational domain is 10×20 km^2 with PML (Perfectly Matched Layer) boundary conditions on the sides and the bottom of the domain and free surface condition at the top. The fluid domain is a circle with a radius of 150 m and is centred at the depth of 1.5 km (Figure 4.11).

The governing equations for the fluid domain are formulated as a first order system, in terms of the linearised continuity equation and the linearised

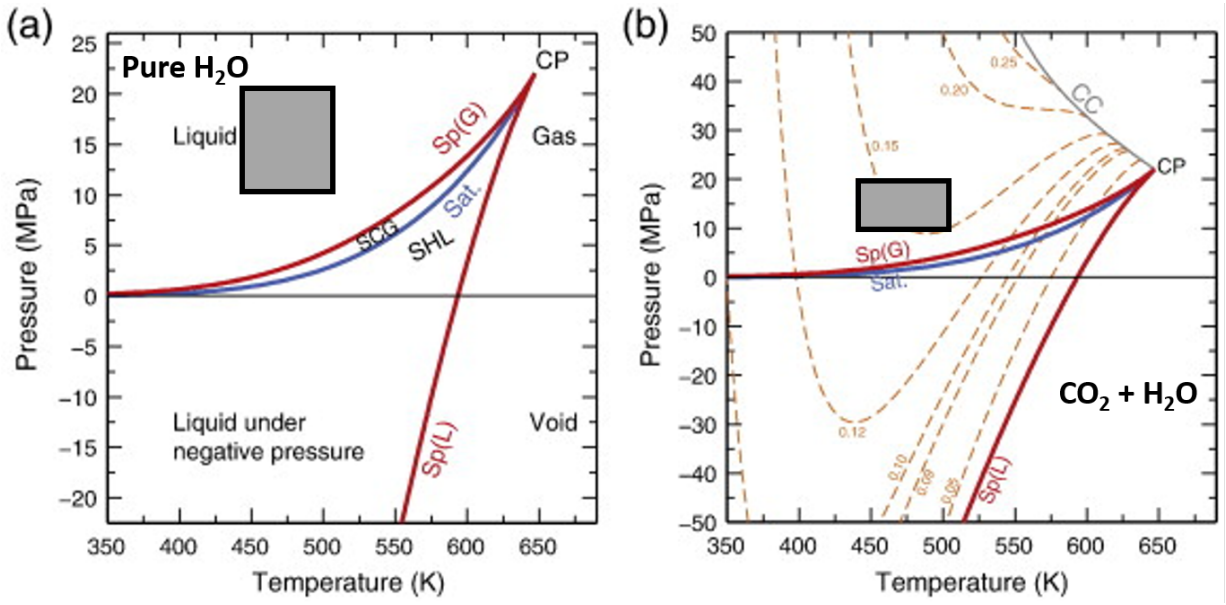

Figure 4.10. Stable, metastable and unstable regions of water in P-T space. a) pure H_2O system b) binary H_2O-CO_2 system. Blue lines represent saturation curve while the red lines are spinodals. Orange dashed lines in b) represent liquid spinodals(Sp(L)) for the H_2O-CO_2 binary system and numbers on the lines refer to the mole fraction x_{CO_2} of dissolved CO_2 in the aqueous solution Adapted from Chouet and Matoza (2013b).

momentum equation as:

$$\begin{aligned} \frac{1}{\rho_{\mathrm{f}} c^2}\frac{\partial p_{\mathrm{t}}}{\partial t} + \nabla \cdot \boldsymbol{v}_{\mathrm{f}} &= Q_{\mathrm{m}} \\ \rho\frac{\partial \boldsymbol{v}_{\mathrm{f}}}{\partial t} + \nabla \cdot (p_{\mathrm{t}}\boldsymbol{I}) &= q_{\mathrm{d}}, \end{aligned} \tag{4.54}$$

where p_{t} is the total acoustic pressure, $\boldsymbol{v}_{\mathrm{f}}$ is the total acoustic velocity field, ρ_{f} is the fluid density, and c is the speed of sound in the fluid. COMSOL defines the right hand sides (Q_{m} and q_{d}) of equation (4.54) in terms of a mass rate of change and volumetric force respectfully.

For the solid (linear elastic) domain, the governing equations are given in a velocity-strain formulation as:

$$\begin{aligned} \rho\frac{\partial \boldsymbol{v}_{\mathrm{s}}}{\partial t} - \nabla \cdot \boldsymbol{S} &= \boldsymbol{F}_v \\ \frac{\partial \boldsymbol{E}}{\partial t} - \frac{1}{2}\left[\nabla \boldsymbol{v}_{\mathrm{s}} + (\nabla \boldsymbol{v}_{\mathrm{s}})^T\right] &= 0 \\ \boldsymbol{S} &= \boldsymbol{C} : \boldsymbol{E}, \end{aligned} \tag{4.55}$$

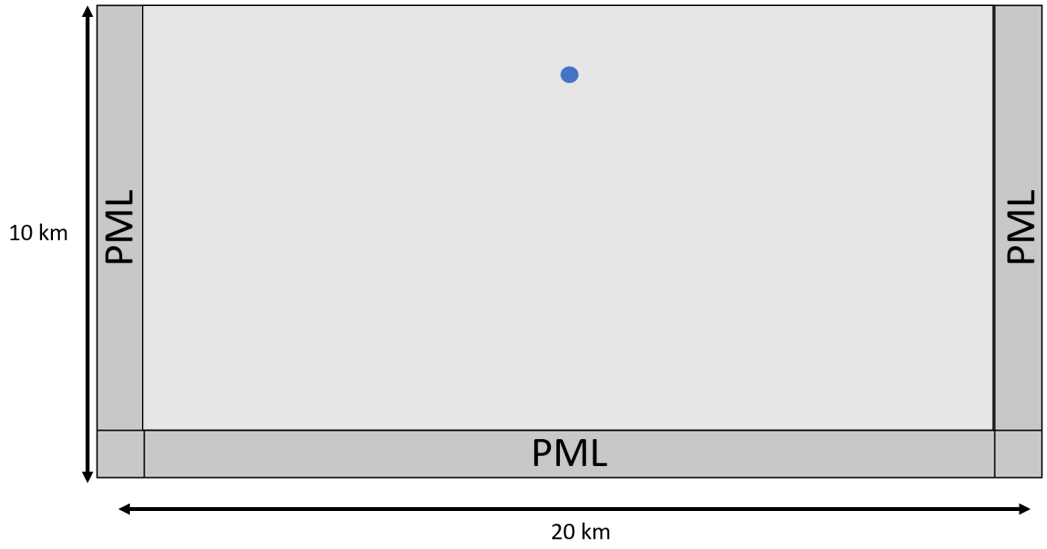

Figure 4.11. Model geometry for the fluid-solid interaction models. The computational domain is surrounded with PMLs on the sides and the bottom and has a free surface boundary condition at the top. The computational domain is divided into two parts, fluid domain (blue) of radius 150 m centred at depth 1.5 km and solid domain (light grey) surrounding it.

where $\boldsymbol{v}_\mathrm{s}$ is the velocity field in the solid, ρ_s is the density of the solid material, $\boldsymbol{S}$ is the stress tensor, $\boldsymbol{E}$ is the strain tensor, $\boldsymbol{C}$ is the elasticity tensor, and $\boldsymbol{F}_v$ is the optional body force (in my case = 0).

The boundary condition between the two media is defined as:

$$\begin{aligned} \boldsymbol{n} \cdot (v_\mathrm{s} - v_\mathrm{f}) &= 0 \\ \boldsymbol{n} \cdot (\boldsymbol{S} + p_\mathrm{t}\boldsymbol{I}) &= 0. \end{aligned} \tag{4.56}$$

The medium properties are given in Table 4.4.

Table 4.4. Values for the density, and P-wave velocity in fluid and solid domain. The values are obtained for temperature of 400 K and pressure of 20 MPa.

Variable/Domain	ρ ($\frac{\mathrm{kg}}{\mathrm{m}^3}$)	v_p ($\frac{\mathrm{m}}{\mathrm{s}}$)	Reference
Solid	2500	3100	
CO_2	481.55	347	Span and Wagner (1996)
H_2O	949.7	1567	Wagner and Kretzschmar (2008)

4.3.3 Sources

The source excitation (Figure 4.12) is modelled using a combination of a spatial 2D truncated Gaussian function centred at the point (x_0, y_0) with a source extent (S) of 100 $1/\mathrm{m}^2$ defined as

$$g(x,y) = \sqrt{\pi S}\exp\left\{\left[-(x-x_0)^2 + (y-y_0)^2\right]/S\right\} \tag{4.57}$$

and the time history described by a Ricker wavelet

$$f(t) = (1 - 2\pi f_0^2(t-t_c)^2)\exp\left[-\pi^2 f_0^2(t-t_c)^2\right], \tag{4.58}$$

where f_0 is the dominant frequency with a time-shift t_c. As I want to model a simple explosion, i.e. outward then inward displacement at the source, the choice of the Ricker wavelet is adequate, because for the input I use the volumetric force (q_d in equation (4.54)), i.e. acceleration at the source, and the Ricker wavelet is the twice differentiated Gaussian function. The dominant frequency of my input signal is 0.5 Hz and has a time shift of 2 s.

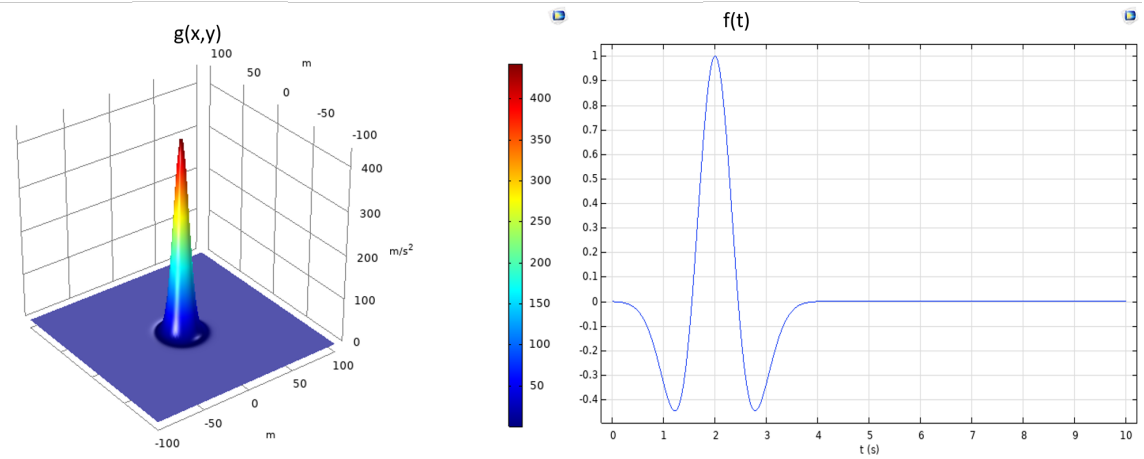

Figure 4.12. Spatial- and time-history of the source function

4.3.4 Discussion

The fluid domain in my models is representative of two end-members - purely CO_2 or purely H_2O. The difference in the results for these two end-members is obvious. Firstly, when the fluid domain is CO_2 we observe a 'non-damped' oscillatory behaviour, while when the fluid domain is filled with H_2O, there

are no oscillations (Figure 4.13a). If we look at the velocity inside the fluid domain, we can see that the oscillation itself is happening in the source region (Figure 4.13b).

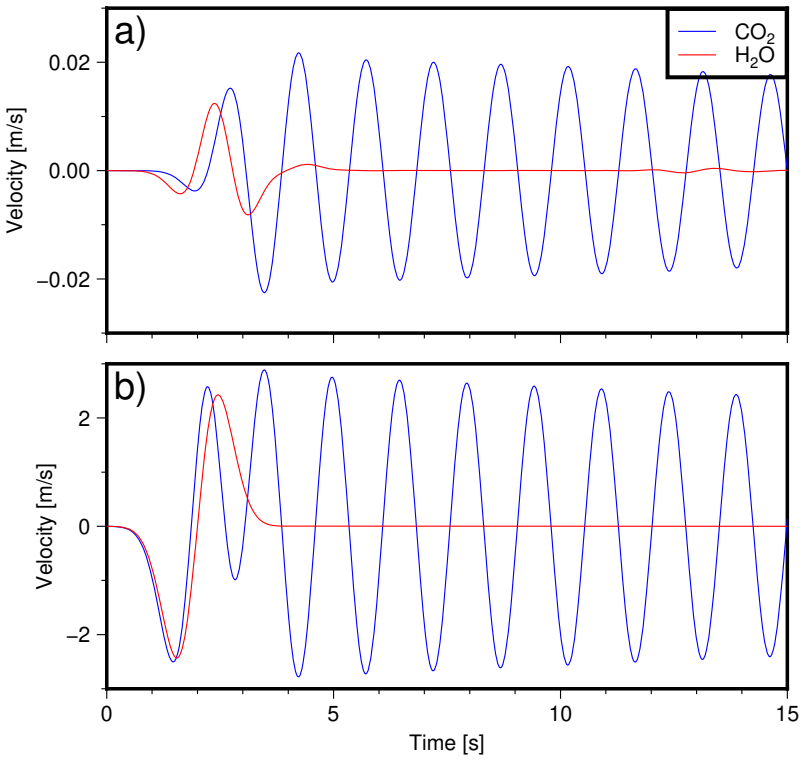

Figure 4.13. The vertical component of the particle velocity for the CO_2 (blue) and H_2O (red) case measured at the surface (a) and inside the fluid domain (b).

The explanation for this difference can be found either by looking at the difference in impedance between the two cases or by looking at the ratio between the signal wavelength and the fluid geometry. The reflection coefficient is defined as

$$RC = \frac{\rho_s v_s - \rho_f v_f}{\rho_s v_s + \rho_f v_f}, \tag{4.59}$$

and depending on the fluid they are:

$$\begin{aligned} RC_{CO_2} &= 0.96 \\ RC_{H_2O} &= 0.68. \end{aligned} \tag{4.60}$$

Hence, the fluid properties have a significant effect on whether the oscillation at the surface will be damped or not. The other explanation is in the ratio

between signal wavelength (λ) and radius of the fluid domain (R). Wavelength of the signal in the fluid domain is equal to:

$$\lambda_{\mathrm{f}} = \frac{v_{\mathrm{f}}}{f_0}. \tag{4.61}$$

Using the same ratio between the wavelength of the signal for the different fluid cases and the radius of the fluid domain

$$\frac{\lambda_{\mathrm{H_2O}}}{R_{\mathrm{new}}} = \frac{\lambda_{\mathrm{CO_2}}}{R}, \tag{4.62}$$

and keeping the initial radius for the fluid domain (R) at 150 m, the radius (R_{new}) of the fluid domain when it is filled with just water has to be 677 m. Figure 4.14 shows the vertical component of the surface velocity when the radius of the fluid (water) domain is larger. The system now oscillates and the damping of the signal is larger than in the case of fluid domain containing just CO_2 (Figure 4.13a) which can be attributed to the difference in the reflection coefficients.

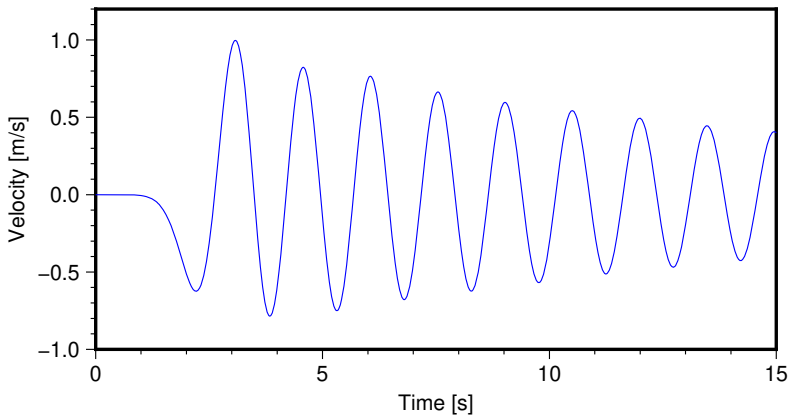

Figure 4.14. Influence of the radius of the fluid domain. Seismogram shows the vertical component of the surface velocity in a fluid(water)-solid coupled system.

However, the results shown in Figure 4.13 do support my hypothesis. The observed VLPs on Whakaari (Figure 1.3) show a waveform similar to a Ricker wavelet. Focusing now on the case where the fluid domain contains H_2O - keeping in mind that the results in Figure 4.13 show velocity seismograms - we can infer that for a Gaussian source displacement in the fluid domain, we obtain a time-differentiated Gaussian displacement at the surface. As we are in the near field, i.e. the source-receiver distance is less than one wavelength

of the signal, we should expect the same displacement at the surface as it is at the source. Therefore, this differentiation of the displacement waveform is caused by the fluid-solid coupling.

4.4 Conclusion

By testing the two hypotheses in this chapter we gained an interesting insight in how different characteristics of poroelastic media affect seismic waves in the frequency band typical in volcano seismology. Firstly, all of the poroelastic waveforms were faster and had smaller amplitudes than the elastic ones. This can have a direct influence on the moment tensor inversions as we would underestimate the volume change at the source if we were to compute synthetic seismograms assuming purely elastic medium. The resulting waveforms show no big difference between the two end members used for the fluid content which makes any future modelling easier as we can assume fluid densities with large uncertainty. In the second hypothesis we tried to get the source region to oscillate using a simple source excitation. This showed a clear contrast between the fluid domain end members - CO_2 and H_2O. While for the CO_2 case, a pulse like excitation causes a long lasting, undamped oscillation at the surface, in the H_2O case we observe the oscillating waveforms we could compare with the observed ones. This would make the concept of the violent explosive phase change in the fluid domain a plausible cause for source excitation; however, the two hypothetical models used in this chapter do not provide unique and exclusive explanations for the oscillatory behaviour and further investigations might find additional plausible models.

Chapter 5

Discussion and Conclusion

The observation of unique Montserrat VLP signals posed several questions triggering this research. Firstly, as the VLP signal was 'hidden' under a superimposed VT swarm, this event emphasises the importance to either look at the spectra of such events or to integrate the velocity seismograms in order to identify VLP signals. Secondly, it is another example of the absolute necessity to perform a proper restitution process. One has to consider spectral components of lowest possible signal frequencies, as the interpretation of the ground displacement, and therefore, the deformation at the source changes drastically (Figure 1.7). After we resolve the correct displacement time-histories of the VLP signal, we can start thinking about quantifying the source volume change and estimating the location of the seismic source.

Although we can look at VLP seismic signals as bridging the field of geodesy and seismology, the use of geodetic techniques in estimating the source characteristics proved to be unsuccessful due to its assumptions of source mechanics (Appendix A). Therefore the best way to estimate the source volume change and find its location is full waveform inversion.

This poses a new question - how well can we resolve MT components if we have a sparse seismic network configuration. To answer this question I developed the MT resolution tests (Chapter 2), using a real seismic network configuration from Montserrat. This work can be seen as an extension to Lanza and Waite (2018), who tested the influence of synthetic station configurations on the determination of several different types of source mechanisms while here we additionally looked at our ability to correctly resolve MT components in dependence on various source orientations.

The moment tensor inversions show remarkable new results which have to be taken into account when designing or upgrading seismic networks. Often the criteria for correctly resolved source parameters is seismogram fit between the observed and synthetic waveforms. In our tests we show that the seismogram fit appears to be acceptable even though a low number of stations with poor azimuthal coverage are used in the inversion (Section 2.4); however those results should not be trusted as they provide a non-unique solution.

Additionally, I examined (Section 2.5) the influence of the source orientation on our ability to correctly resolve MT components. The results show that the source strike orientation considerably influences the MTI results as for certain strike angles there was a leakage into diagonal components of the MT and for some angles, the input MT components were impossible to resolve. However, the introduction of the isotropic component to the input moment tensor (Section 2.6.3) improves our ability to correctly resolve source parameters as the isotropic components dominate the radiation pattern.

The outcomes of the moment tensor resolution study can be seen in the moment tensor inversion results in Chapter 3 for the VLP event at Montserrat for which two different MTI methods were employed: One where we invert for time histories and amplitudes of moment tensor and single force components, and the other where we assume the source time history of only moment tensor components based on simplified restituted displacement. These different methods do not agree with source location. This discrepancy demonstrates the influence of the sparsity of the seismic network and that of using additional single forces. Furthermore, the discrepancy reveals that the location and best source model are inferred from the 'waveform' fit at the surface, which, as demonstrated, is based on a non-unique solution.

Ideally, one should map the complete volumetric grid of possible source locations and source mechanisms, and couple it with the moment tensor inversion resolution tests. Such an approach would give us higher certainty of our results and would be an interesting future research topic.

The resolved downward single force component detected in Section 3.4.1 (Figure 3.10) can be explained to be due to removal of the "volcano lid" in this out-gassing event (Ohminato et al., 2006b). The ratio between MT and SF amplitudes suggests that the influence of single forces is negligible, however

if we model a finite source, single forces become more dominant (Ohminato, 2019). I will address this issue in future studies.

The necessity of the resolution tests described in Chapter 2 is quite clear. Several factors often impact the normal operations of seismic stations. Figure 5.1 shows the timeline when certain stations were operational between April and October 2020 at Montserrat (Stinton et al., 2020). We see that around May 1st, only 3 stations were operational (MSS1 is a GNSS station) which makes the scenarios in Chapter 2 very realistic. Another problem which might arise is the loss of power at relay stations through which the data from the stations are transferred to the observatory. These tests can also be performed in order to estimate which stations are more 'useful' for estimating correct moment tensor inversion results.

Figure 5.1. Timeline when certain stations were operational between April and September 2020 at Montserrat. Green depicts the stations that were operational (including those with outages lasting less than few hours), yellow depicts stations that were online but with significant issued and red depicts stations that were offline. Adopted from Stinton et al. (2020).

The main drawback of these tests is the computational power needed to calculate correct Green's functions for a grid of possible source locations as volcano observatories, in general, do not have such computational capability in-house. Therefore, we can look at this as another example why co-operation between observatories and research institutes, whether domestic or abroad can benefit both.

After performing a proper restitution process ensuring we extract the pure displacement signal, free from any effect of the instrument, the VLP signals at Whakaari show an oscillatory waveform (Figure 4.1) in contrast to the case of Montserrat where an oscillatory pattern would be due to the incomplete removal of the instrument response. This displacement has been previously modelled as inflation/deflation source mechanism (Jolly et al., 2018).

In Chapter 4, I tested a hypothesis that the observed waveforms could be due to poroelastic wave propagation. The modelling showed that the introduction of fluids inside the porous media greatly affects the medium characteristics and produces interesting effects such as differences in amplitudes and arrival times between waves propagating through poroelastic and elastic media (Figure 4.6), however the frequency content of our modelled seismic waves (typical for volcano seismology) impacts the existence of slow Biot P-wave (Figure 4.7). Including fluids in porous media helps us with modelling the source excitation as well. In case of Whakaari where we have a binary CO_2-H_2O system we can easily get to fluid properties where water becomes very explosive (Thiery and Mercury, 2009a). Although we speculate that the sudden vaporisation of water (explained as a step function or a Gaussian) could produce the oscillatory behaviour, the results suggest, that for a poroelastic medium, a re-inflation at the source is needed to explain the observed VLP waveforms.

We modelled this 're-inflation' at the source by resonance in the source region when we model the system as an interaction between solid and fluid. In such a system, the relationship between an impedance contrast, fluid and solid properties, and the geometry of the fluid domain plays a significant role (Section 4.3).

Although the two hypotheses did not provide a unique explanation for the observed waveforms, the poroelastic modelling and fluid-solid interactions should not be discarded from future considerations when studying seismic signals in hydrothermal areas. Considering neither of the two scenarios does add any computational expense we can take into a consideration more realistic scenarios. Unfortunately, the module codes for poroelastic modelling are not included in available, commonly used 3D wave propagation software. However, with increased demand to focus on the impact of a wide variety of medium properties these codes (e.g. Morency and Tromp, 2008; Carcione et al., 2010)

will become widely available. This would make the future studies more focused on the impact of different medium properties rather than just developing numerical schemes.

The work presented in this thesis sheds a light to previously understudied problems in volcano seismology - proper treatment of VLP signals, the influence of seismic network configuration on our ability to correctly resolve moment tensor components, and the influence of fluids in volcanic system have on the observed waveforms in the frequency band typical in volcano seismology. As a volcano-seismological community, we have to take special care when processing data and especially when we use techniques and softwares developed for tectonic seismology. As shown in this thesis, fluids in the system change the medium properties and have an effect on the shape of the waveforms, the station configuration on volcanoes should always be considered when interpreting results obtained by moment tensor inversion, and that the estimation of the location and best source model inferred solely from the 'waveform' fit at the surface can be based on a non-unique solution.

Chapter 6

Bibliography

Aki, K. and Richards, P. G. (2002). *Quantitative seismology.*

Aster, R., Zandomeneghi, D., Mah, S., McNamara, S., Henderson, D., Knox, H. and Jones, K. (2008). Moment tensor inversion of very long period seismic signals from strombolian eruptions of Erebus volcano. *Journal of Volcanology and Geothermal Research*, **177**(3), pp. 635–647.

Auger, E., D'Auria, L., Martini, M., Chouet, B. and Dawson, P. (2006). Real-time monitoring and massive inversion of source parameters of very long period seismic signals: An application to Stromboli volcano, Italy. *Geophysical Research Letters*, **33**(4), p. L04301.

Bagnardi, M. and Hooper, A. (2018). Inversion of surface deformation data for rapid estimates of source parameters and uncertainties: A bayesian approach. *Geochemistry, Geophysics, Geosystems*, **19**(7), pp. 2194–2211.

Bean, C. J., De Barros, L., Lokmer, I., Métaxian, J.-P., O'Brien, G. and Murphy, S. (2014). Long-period seismicity in the shallow volcanic edifice formed from slow-rupture earthquakes. *Nature Geoscience*, **7**(1), pp. 71–75.

Bean, C., Lokmer, I. and O'Brien, G. (2008). Influence of near-surface volcanic structure on long-period seismic signals and on moment tensor inversions: Simulated examples from Mount Etna. *Journal of Geophysical Research: Solid Earth*, **113**(B8).

Biot, M. A. (1955). Theory of elasticity and consolidation for a porous anisotropic solid. *Journal of applied physics*, **26**(2), pp. 182–185.

Biot, M. (1956a). Theory of elastic waves in a fluid-saturated porous solid. 1. low frequency range. *J. Acoust. Soc. Am.*, **28**, pp. 168–178.

Biot, M. A. (1956b). Theory of propagation of elastic waves in a fluid-saturated porous solid. ii. higher frequency range. *The Journal of the acoustical Society of america*, **28**(2), pp. 179–191.

Biot, M. A. (1962). Mechanics of deformation and acoustic propagation in porous media. *Journal of applied physics*, **33**(4), pp. 1482–1498.

Biot, M. A. and Willis, D. (1957). The elastic coefficients of the theory of consolidation. *J. appl. Mech*, **24**, pp. 594–601.

Brown, J. M., Angel, R. J. and Ross, N. L. (2016). Elasticity of plagioclase feldspars. *Journal of Geophysical Research: Solid Earth*, **121**(2), pp. 663–675.

Carcione, J. M., Morency, C. and Santos, J. E. (2010). Computational poroelasticity—a review. *Geophysics*, **75**(5), pp. 75A229–75A243.

Caricchi, L., Sheldrake, T. E. and Blundy, J. (2018). Modulation of magmatic processes by CO_2 flushing. *Earth and Planetary Science Letters*, **491**, pp. 160–171.

Caudron, C., Taisne, B., Neuberg, J., Jolly, A. D., Christenson, B., Lecocq, T., Suparjan, Syahbana, D. and Suantika, G. (2018). Anatomy of phreatic eruptions. *Earth, Planets and Space*, **70**(1), p. 168.

Cesca, S. and Dahm, T. (2008). A frequency domain inversion code to retrieve time-dependent parameters of very long period volcanic sources. *Computers & Geosciences*, **34**(3), pp. 235–246.

Chai, M., Brown, J. M. and Slutsky, L. J. (1997). The elastic constants of an aluminous orthopyroxene to 12.5 GPa. *Journal of Geophysical Research: Solid Earth*, **102**(B7), pp. 14779–14785.

Chandler, R. (1981). Transient streaming potential measurements on fluid-saturated porous structures: An experimental verification of Biot's slow wave in the quasi-static limit. *The Journal of the Acoustical Society of America*, **70**(1), pp. 116–121.

Chouet, B. (1988). Resonance of a fluid-driven crack: Radiation properties and implications for the source of long-period events and harmonic tremor. *Journal of Geophysical Research: Solid Earth*, **93**(B5), pp. 4375–4400.

Chouet, B. A. (1996a). Long-period volcano seismicity: its source and use in eruption forecasting. *Nature*, **380**(6572), pp. 309–316.

Chouet, B. A. (1996b). New methods and future trends in seismological volcano monitoring. In *Monitoring and mitigation of volcano hazards*. Springer, pp. 23–97.

Chouet, B. and Dawson, P. (2011). Shallow conduit system at Kilauea Volcano, Hawaii, revealed by seismic signals associated with degassing bursts. *Journal of Geophysical Research: Solid Earth*, **116**(B12).

Chouet, B., Dawson, P. and Arciniega-Ceballos, A. (2005). Source mechanism of vulcanian degassing at Popocatépetl Volcano, Mexico, determined from waveform inversions of very long period signals. *Journal of Geophysical Research - Solid Earth*, **110**(B7), p. B07301.

Chouet, B. A., Dawson, P. B., James, M. R. and Lane, S. J. (2010). Seismic source mechanism of degassing bursts at Kilauea Volcano, Hawaii: Results from waveform inversion in the 10–50 s band. *Journal of Geophysical Research: Solid Earth*, **115**(B9).

Chouet, B., Dawson, P. and Martini, M. (2008). Shallow-conduit dynamics at Stromboli Volcano, Italy, imaged from waveform inversions. *Geological Society, London, Special Publications*, **307**(1), pp. 57–84.

Chouet, B., Dawson, P., Ohminato, T., Martini, M., Saccorotti, G., Giudicepietro, F., De Luca, G., Milana, G. and Scarpa, R. (2003). Source mechanisms of explosions at Stromboli Volcano, Italy, determined from moment-tensor inversions of very-long-period data. *Journal of Geophysical Research: Solid Earth*, **108**(B1).

Chouet, B. and Matoza, R. (2013a). A multi-decadal view of seismic methods for detecting precursors of magma movement and eruption. *Journal of Volcanology and Geothermal Research*, **252**, pp. 108 – 175.

Chouet, B. A. and Matoza, R. S. (2013b). A multi-decadal view of seismic methods for detecting precursors of magma movement and eruption. *Journal of Volcanology and Geothermal Research*, **252**, pp. 108–175.

Cole, P., Bass, V., Christopher, T., Odbert, H., Smith, P., R., S., Stinton, A., Syers, R. and Williams, P. (2012). MVO scientific report for volcanic activity between 1 November 2011 and 30 April 2012.

Contreras-Arratia, R. and Neuberg, J. W. (2019). Complex seismic sources in volcanic environments: Radiation modelling and moment tensor inversions. *Journal of Volcanology and Geothermal Research*, **381**, pp. 262–272.

Dai, N., Vafidis, A. and Kanasewich, E. (1995). Wave propagation in heterogeneous, porous media: A velocity-stress, finite-difference method. *Geophysics*, **60**(2), pp. 327–340.

Dawson, P. B., Benitez, M., Chouet, B. A., Wilson, D. and Okubo, P. G. (2010). Monitoring very-long-period seismicity at Kilauea Volcano, Hawaii. *Geophysical Research Letters*, **37**(18).

Dawson, P. and Chouet, B. (2014). Characterization of very-long-period seismicity accompanying summit activity at Kilauea Volcano, Hawaii: 2007-2013. *Journal of Volcanology and Geothermal Research*, **278-279**, p. 59.

Dawson, P. B., Chouet, B. A. and Power, J. (2011). Determining the seismic source mechanism and location for an explosive eruption with limited observational data: Augustine Volcano, Alaska. *Geophysical Research Letters*, **38**(3).

Du, K.-L. and Swamy, M. N. S. (2016). *Simulated Annealing*. Cham: Springer International Publishing, pp. 29–36.

Dullien, F. A. (2012). *Porous media: fluid transport and pore structure*. Academic press.

Ferrazzini, V. and Aki, K. (1987). Slow waves trapped in a fluid-filled infinite crack: Implication for volcanic tremor. *Journal of Geophysical Research: Solid Earth*, **92**(B9), pp. 9215–9223.

Fujita, E., Ukawa, M. and Yamamoto, E. (2004). Subsurface cyclic magma sill expansions in the 2000 Miyakejima volcano eruption: Possibility of two-phase flow oscillation. *Journal of Geophysical Research: Solid Earth*, **109**(B4).

Green, D. N. and Neuberg, J. (2005). Seismic and infrasonic signals associated with an unusual collapse event at the Soufrière Hills volcano, Montserrat. *Geophysical Research Letters*, **32**(7), p. L07308.

Haney, M. M. (2010). Location and mechanism of very long period tremor during the 2008 eruption of Okmok volcano from interstation arrival times. *Journal of Geophysical Research: Solid Earth*, **115**(B10).

Hautmann, S., Witham, F., Christopher, T., Cole, P., Linde, A. T., Sacks, I. S. and Sparks, R. S. J. (2014). Strain field analysis on Montserrat (W.I.) as tool for assessing permeable flow paths in the magmatic system of Soufrière Hills volcano. *Geochemistry, Geophysics, Geosystems*, **15**(3), pp. 676–690.

Heap, M. J., Kennedy, B. M., Farquharson, J. I., Ashworth, J., Mayer, K., Letham-Brake, M., Reuschle, T., Gilg, H. A., Scheu, B., Lavallee, Y. et al. (2017). A multidisciplinary approach to quantify the permeability of the Whakaari/White Island volcanic hydrothermal system (Taupo Volcanic Zone, New Zealand). *Journal of Volcanology and Geothermal Research*, **332**, pp. 88–108.

Heap, M. J., Kennedy, B. M., Pernin, N., Jacquemard, L., Baud, P., Farquharson, J. I., Scheu, B., Lavallée, Y., Gilg, H. A., Letham-Brake, M. et al. (2015). Mechanical behaviour and failure modes in the Whakaari (White Island volcano) hydrothermal system, New Zealand. *Journal of Volcanology and Geothermal Research*, **295**, pp. 26–42.

Hidayat, D., Chouet, B., Voight, B., Dawson, P. and Ratdomopurbo, A. (2002). Source mechanism of very-long-period signals accompanying dome growth activity at Merapi Volcano, Indonesia. *Geophysical research letters*, **29**(23).

Hill, R. (1952). The elastic behaviour of a crystalline aggregate. *Proceedings of the Physical Society. Section A*, **65**(5), p. 349.

Hill, D. P., Dawson, P., Johnston, M. J., Pitt, A., Biasi, G. and Smith, K. (2002). Very-long-period volcanic earthquakes beneath Mammoth Mountain, California. *Geophysical Research Letters*, **29**(10).

James, M. R., Lane, S. J. and Chouet, B. A. (2006). Gas slug ascent through changes in conduit diameter: Laboratory insights into a volcano-seismic source process in low-viscosity magmas. *Journal of Geophysical Research - Solid Earth*, **111**(B5), pp. B05201–n/a.

Jolly, A., Chardot, L., Neuberg, J., Fournier, N., Scott, B. and Sherburn, S. (2012). High impact mass drops from helicopter: a new active seismic source method applied in an active volcanic setting. *Geophysical research letters*, **39**(12).

Jolly, A., Lokmer, I., Christenson, B. and Thun, J. (2018). Relating gas ascent to eruption triggering for the April 27, 2016, White Island (Whakaari), New Zealand eruption sequence. *Earth, Planets and Space*, **70**(1), pp. 1–15.

Jolly, A., Lokmer, I., Thun, J., Salichon, J., Fry, B. and Chardot, L. (2017). Insights into fluid transport mechanisms at White Island from analysis of coupled very long-period (VLP), long-period (LP) and high-frequency (HF) earthquakes. *Journal of Volcanology and Geothermal Research*.

Kaneshima, S., Kawakatsu, H., Matsubayashi, H., Sudo, Y., Tsutsui, T., Ohminato, T., Ito, H., Uhira, K., Yamasato, H., Oikawa, J. et al. (1996). Mechanism of phreatic eruptions at Aso volcano inferred from near-field broadband seismic observations. *SCIENCE*, pp. 642–644.

Karpfinger, F., Müller, T. M. and Gurevich, B. (2009). Green's functions and radiation patterns in poroelastic solids revisited. *Geophysical Journal International*, **178**(1), pp. 327–337.

Kawakatsu, H., Kaneshima, S., Matsubayashi, H., Ohminato, T., Sudo, Y., Tsutsui, T., Uhira, K., Yamasato, H., Ito, H. and Legrand, D. (2000). Aso94: Aso seismic observation with broadband instruments. *Journal of Volcanology and Geothermal Research*, **101**(1), pp. 129–154.

Kawakatsu, H., Ohminato, T. and Ito, H. (1994). 10s-period volcanic tremors observed over a wide area in southwestern japan. *Geophysical Research Letters*, **21**(18), pp. 1963–1966.

Kawakatsu, H., Ohminato, T., Ito, H., Kuwahara, Y., Kato, T., Tsuruga, K., Honda, S. and Yomogida, K. (1992). Broadband seismic observation at the Sakurajima volcano, Japan. *Geophysical Research Letters*, **19**(19), pp. 1959–1962.

Kazahaya, R., Mori, T., Takeo, M., Ohminato, T., Urabe, T. and Maeda, Y. (2011). Relation between single very-long-period pulses and volcanic gas emissions at Mt. Asama, Japan. *Geophysical Research Letters*, **38**(11).

Komatitsch, D., Vilotte, J.-P., Tromp, J., Ampuero, J.-P., Bai, K., Basini, P., Blitz, C., Bozdag, E., Casarotti, E., Charles, J., Chen, M., Galvez, P., Goddeke, D., Hjorleifsdottir, V., Labarta, J., Le Goff, N., Le Loher, P., Lefebvre, M., Liu, Q., Luo, Y., Maggi, A., Magnoni, F., Martin, R., Matzen, R., McRitchie, D., Meschede, M., Messmer, P., Michea, D., Nadh Somala, S., Nissen-Meyer, T., Peter, D., Rietmann, M., de Andrade, E., Savage, B., Schuberth, B., Sieminski, A., Strand, L., Tape, C., Xie, Z. and Zhu, H. (2012). Specfem3d cartesian v2.0.2 [software]. doi:http://doi.org/NoDOI.

Krischer, L., Megies, T., Barsch, R., Beyreuther, M., Lecocq, T., Caudron, C. and Wassermann, J. (2015). Obspy: a bridge for seismology into the scientific Python ecosystem. *Computational Science and Discovery*, **8**(1), p. 014003.

Kumagai, H. (2006). Temporal evolution of a magmatic dike system inferred from the complex frequencies of very long period seismic signals. *Journal of Geophysical Research: Solid Earth*, **111**(B6).

Kumagai, H., Miyakawa, K., Negishi, H., Inoue, H., Obara, K. and Suetsugu, D. (2003). Magmatic dike resonances inferred from very-long-period seismic signals. *Science*, **299**(5615), pp. 2058–2061.

Kumagai, H., Ohminato, T., Nakano, M., Ooi, M., Kubo, A., Inoue, H. and Oikawa, J. (2001a). Very-long-period seismic signals and caldera formation at Miyake Island, Japan. *Science*, **293**(5530), pp. 687–690.

Kumagai, H., Ohminato, T., Nakano, M., Ooi, M., Kubo, A., Inoue, H. and Oikawa, J. (2001b). Very-long-period seismic signals and caldera formation at Miyake island, Japan. *Science*, **293**(5530), pp. 687–690.

Lanza, F. and Waite, G. P. (2018). A nonlinear approach to assess network performance for moment-tensor studies of long-period signals in volcanic settings. *Geophysical Journal International*, **215**(2), pp. 1352–1367.

Legrand, D., Kaneshima, S. and Kawakatsu, H. (2000). Moment tensor analysis of near-field broadband waveforms observed at Aso Volcano, Japan. *Journal of volcanology and geothermal research*, **101**(1-2), pp. 155–169.

Legrand, D., Rouland, D., Frogneux, M., Carniel, R., Charley, D., Roult, G. and Robin, C. (2005). Interpretation of very long period tremors at Ambrym volcano, Vanuatu, as quasi-static displacement field related to two distinct magmatic sources. *Geophysical research letters*, **32**(6).

Maeda, Y., Kumagai, H., Lacson, R., Figueroa, M. S., Yamashina, T., Ohkura, T. and Baloloy, A. V. (2015). A phreatic explosion model inferred from a very long period seismic event at Mayon Volcano, Philippines. *Journal of Geophysical Research: Solid Earth*, **120**(1), pp. 226–242.

Maeda, Y. and Takeo, M. (2011). Very-long-period pulses at Asama volcano, central Japan, inferred from dense seismic observations. *Geophysical Journal International*, **185**(1), pp. 265–282.

Makhnenko, R. Y. and Labuz, J. F. (2016). Elastic and inelastic deformation of fluid-saturated rock. *Philosophical Transactions of the Royal Society A: Mathematical, Physical and Engineering Sciences*, **374**(2078), p. 20150422.

Michon, L., Villeneuve, N., Catry, T. and Merle, O. (2009). How summit calderas collapse on basaltic volcanoes: New insights from the April 2007 caldera collapse of Piton de la Fournaise volcano. *Journal of Volcanology and Geothermal Research*, **184**(1-2), pp. 138–151.

Miller, A., Stewart, R., White, R., Luckett, R., Baptie, B., Aspinall, W., Latchman, J., Lynch, L. and Voight, B. (1998). Seismicity associated with dome growth and collapse at the Soufriere Hills Volcano, Montserrat. *Geophysical Research Letters*, **25**(18), pp. 3401–3404.

Mogi, K. (1958). Relations between the eruption of various volcanoes and the deformations of the ground surfaces around them. *B. Earthq. Res. Inst. Univ. Tokyo*, **36**, pp. 99–134.

Moradi, S., Lawton, D. C. and Krebes, E. S. (2015). Finite difference modeling of the diffusive slow p-wave in poroelastic media. *CREWES Research Project*.

Morency, C. and Tromp, J. (2008). Spectral-element simulations of wave propagation in porous media. *Geophysical Journal International*, **175**(1), pp. 301–345.

Murase, T. and McBirney, A. R. (1973). Properties of some common igneous rocks and their melts at high temperatures. *Geological Society of America Bulletin*, **84**(11), pp. 3563–3592.

Nakamichi, H., Kumagai, H., Nakano, M., Okubo, M., Kimata, F., Ito, Y. and Obara, K. (2009). Source mechanism of a very-long-period event at Mt Ontake, central Japan: Response of a hydrothermal system to magma intrusion beneath the summit. *Journal of Volcanology and Geothermal Research*, **187**(3–4), pp. 167 – 177.

Neuberg, J. (2006). Multi-parameter monitoring and modelling of volcanic processes. *Statistics in Volcanology. London: Special publications of IAVCEI*, **1**, pp. 215–230.

Neuberg, J. W. (2021). *Earthquakes, Volcanogenic*. Cham: Springer International Publishing, pp. 329–338.

Neuberg, J., Barclay, J., Burton, M., Calder, E., Fournier, N. and Rivalta, E. (2018). Assessment of the hazards and risks associated with the Soufrière Hills Volcano, Montserrat. *22nd Report of the Scientific Advisory Committee on Montserrat Volcanic Activity (Full Report)*.

Neuberg, J. and Luckett, R. (1996a). Seismo-volcanic sources on Stromboli volcano. *Annals of Geophysics*, **39**(2).

Neuberg, J. and Luckett, R. (1996b). Seismo-volcanic sources on Stromboli volcano.

Neuberg, J., Luckett, R., Baptie, B. and Olsen, K. (2000). Models of tremor and low-frequency earthquake swarms on Montserrat. *Journal of Volcanology and Geothermal Research*, **101**(1–2), pp. 83 – 104.

Neuberg, J., Luckett, R., Ripepe, M. and Braun, T. (1994). Highlights from a seismic broadband array on Stromboli Volcano. *Geophysical Research Letters*, **21**(9), pp. 749–752.

Neuberg, J. and Pointer, T. (2000). Effects of volcano topography on seismic broad-band waveforms. *Geophysical Journal International*, **143**(1), pp. 239–248.

Nishimura, T., Nakamichi, H., Tanaka, S., Sato, M., Kobayashi, T., Ueki, S., Hamaguchi, H., Ohtake, M. and Sato, H. (2000). Source process of very long period seismic events associated with the 1998 activity of iwate volcano, northeastern japan. *Journal of Geophysical Research: Solid Earth*, **105**(B8), pp. 19135–19147.

Nishimura, T., Ueki, S., Yamawaki, T., Tanaka, S., Hashino, H., Sato, M., Nakamichi, H. and Hamaguchi, H. (2003). Broadband seismic signals associated with the 2000 volcanic unrest of Mount Bandai, northeastern Japan. *Journal of volcanology and geothermal research*, **119**(1), pp. 51–59.

O'Brien, G. and Bean, C. (2008). Seismicity on volcanoes generated by gas slug ascent. *Geophysical Research Letters*, **35**(16).

O'Brien, G. S. and Bean, C. J. (2009). Volcano topography, structure and intrinsic attenuation: Their relative influences on a simulated 3D visco-elastic wavefield. *Journal of Volcanology and Geothermal Research*, **183**(1-2), pp. 122–136.

Ohminato, T. (2006a). Characteristics and source modeling of broadband seismic signals associated with the hydrothermal system at Satsuma–Iwojima volcano, Japan. *Journal of volcanology and geothermal research*, **158**(3), pp. 467–490.

Ohminato, T. (2006b). Characteristics and source modeling of broadband seismic signals associated with the hydrothermal system at Satsuma–Iwojima

volcano, Japan. *Journal of volcanology and geothermal research*, **158**(3), pp. 467–490.

Ohminato, T. (2019). Re-examination of the contribution of single force component on vlp seismic signals associated with the 2000 eruption of Miyakejima Volcano, Japan.

Ohminato, T., Chouet, B. A., Dawson, P. and Kedar, S. (1998). Waveform inversion of very long period impulsive signals associated with magmatic injection beneath Kilauea volcano, Hawaii. *Journal of Geophysical Research: Solid Earth*, **103**(B10), pp. 23839–23862.

Ohminato, T. and Ereditato, D. (1997). Broadband seismic observations at Satsuma-Iwojima Volcano, Japan. *Geophysical research letters*, **24**(22), pp. 2845–2848.

Ohminato, T., Takeo, M., Kumagai, H., Yamashina, T., Oikawa, J., Koyama, E., Tsuji, H. and Urabe, T. (2006a). Vulcanian eruptions with dominant single force components observed during the Asama 2004 volcanic activity in Japan. *Earth, Planets and Space*, **58**(5), pp. 583–593.

Ohminato, T., Takeo, M., Kumagai, H., Yamashina, T., Oikawa, J., Koyama, E., Tsuji, H. and Urabe, T. (2006b). Vulcanian eruptions with dominant single force components observed during the Asama 2004 volcanic activity in Japan. *Earth, planets and space*, **58**(5), pp. 583–593.

Okada, Y. (1985). Surface deformation due to shear and tensile faults in a half-space. *Bulletin of the seismological society of America*, **75**(4), pp. 1135–1154.

Pabst, W. and Gregorová, E. (2013). Elastic properties of silica polymorphs–a review. *Ceramics-Silikaty*, **57**(3), pp. 167–184.

Park, I., Jolly, A., Lokmer, I. and Kennedy, B. (2020). Classification of long-term very long period (VLP) volcanic earthquakes at Whakaari/White Island volcano, New Zealand. *Earth, Planets and Space*, **72**(1), pp. 1–10.

Reuss, A. (1929). Calculation of the flow limits of mixed crystals on the basis of the plasticity of monocrystals. *Z. Angew. Math. Mech*, **9**, pp. 49–58.

Rice, J. R. (1975). On the stability of dilatant hardening for saturated rock masses. *Journal of Geophysical Research*, **80**(11), pp. 1531–1536.

Richards, F. J. (1959). A flexible growth function for empirical use. *Journal of Experimental Botany*, **10**(29), pp. 290–300.

Rowe, C. A., Aster, R. C., Kyle, P. R., Schlue, J. W. and Dibble, R. R. (1998). Broadband recording of strombolian explosions and associated very-long-period seismic signals on Mount Erebus volcano, Ross Island, Antarctica. *Geophysical Research Letters*, **25**(13), p. 2297.

Sanderson, R. W., Johnson, J. B. and Lees, J. M. (2010). Ultra-long period seismic signals and cyclic deflation coincident with eruptions at Santiaguito volcano, Guatemala. *Journal of Volcanology and Geothermal Research*, **198**(1), pp. 35–44.

Selvadurai, A. (2019). The Biot coefficient for a low permeability heterogeneous limestone. *Continuum Mechanics and Thermodynamics*, **31**(4), pp. 939–953.

Selvadurai, P., Selvadurai, P. A. and Nejati, M. (2019). A multi-phasic approach for estimating the biot coefficient for grimsel granite. *Solid Earth*, **10**(6), pp. 2001–2014.

Sindija, D., Neuberg, J. and Smith, P. (2021). The complex, static displacement of a very long period seismic signal observed at soufrière hills volcano, montserrat, wi. *Journal of Volcanology and Geothermal Research*, **413**, p. 107209. ISSN 0377-0273.

Smith, P. (2015). Volcano-tectonic seismicity of Soufriere Hills volcano, Montserrat. *Encyclopedia of Earthquake Engineering*, pp. 3907–3919.

Span, R. and Wagner, W. (1996). A new equation of state for carbon dioxide covering the fluid region from the triple-point temperature to 1100 k at pressures up to 800 mpa. *Journal of physical and chemical reference data*, **25**(6), pp. 1509–1596.

Stinton, A., Bass, V., Christopher, C., Fergus, M., Howe, T., James, D., Miller, V., Pascal, K., Retourne, K., , Ryan, G., Stewart, R., Syers, R. and Williams, P. (2020). MVO scientific report for volcanic activity between 1 April 2020 and 30 September 2020.

Stix, J. and de Moor, J. M. (2018). Understanding and forecasting phreatic eruptions driven by magmatic degassing. *Earth, Planets and Space*, **70**(1), pp. 1–19.

Thiery, R. and Mercury, L. (2009a). Explosive properties of water in volcanic and hydrothermal systems. *Journal of Geophysical Research: Solid Earth*, **114**(B5).

Thiery, R. and Mercury, L. (2009b). Explosivity conditions of aqueous solutions. *Journal of solution chemistry*, **38**(7), pp. 893–905.

Trovato, C., Lokmer, I., De Martin, F. and Aochi, H. (2016). Long period (LP) events on Mt Etna volcano (Italy): the influence of velocity structures on moment tensor inversion. *Geophysical Supplements to the Monthly Notices of the Royal Astronomical Society*, **207**(2), pp. 785–810.

Uhira, K. and Takeo, M. (1994). The source of explosive eruptions of Sakura-jima volcano, Japan. *Journal of Geophysical Research: Solid Earth*, **99**(B9), pp. 17775–17789.

Uhira, K., Yamasato, H. and Takeo, M. (1994). Source mechanism of seismic waves excited by pyroclastic flows observed at Unzen volcano, Japan. *Journal of Geophysical Research: Solid Earth*, **99**(B9), pp. 17757–17773.

Van Der Grinten, J. G., Van Dongen, M. E. and Van Der Kogel, H. (1985). A shock-tube technique for studying pore-pressure propagation in a dry and water-saturated porous medium. *Journal of applied physics*, **58**(8), pp. 2937–2942.

Vavryčuk, V. (2001). Inversion for parameters of tensile earthquakes. *Journal of Geophysical Research: Solid Earth*, **106**(B8), pp. 16339–16355. ISSN 2156-2202. doi:10.1029/2001JB000372.
URL: *http://dx.doi.org/10.1029/2001JB000372*

Vilarrasa, V., Bolster, D., Dentz, M., Olivella, S. and Carrera, J. (2010). Effects of CO_2 compressibility on CO_2 storage in deep saline aquifers. *Transport in porous media*, **85**(2), pp. 619–639.

Voight, W. (1928). Lehrbuch der kristallphysik. *Teubner, Leipzig*.

Wagner, W. and Kretzschmar, H. (2008). Properties of water and steam based on the industrial formulation iapws-if97.

Waite, G. P. (2014). Very-long-period seismicity at active volcanoes: Source mechanisms. *Encyclopedia of Earthquake Engineering*, pp. 1–12.

Waite, G. P., Chouet, B. A. and Dawson, P. B. (2008). Eruption dynamics at Mount St. Helens imaged from broadband seismic waveforms: Interaction of the shallow magmatic and hydrothermal systems. *Journal of Geophysical Research: Solid Earth*, **113**(B2). ISSN 2156-2202. B02305.

Watt, J. P. (1979). Hashin-shtrikman bounds on the effective elastic moduli of polycrystals with orthorhombic symmetry. *Journal of Applied Physics*, **50**(10), pp. 6290–6295.

Wielandt, E. and Forbriger, T. (1999). Near-field seismic displacement and tilt associated with the explosive activity of Stromboli. *Annals of Geophysics*, **42**(3).

Xu, H., Zhao, Y., Zhang, J., Wang, Y., Hickmott, D. D., Daemen, L. L., Hartl, M. A. and Wang, L. (2010). Anisotropic elasticity of jarosite: A high-p synchrotron xrd study. *American Mineralogist*, **95**(1), pp. 19–23.

Yamamoto, M., Kawakatsu, H., Yomogida, K. and Koyama, J. (2002). Long-period (12 sec) volcanic tremor observed at Usu 2000 eruption: Seismological detection of a deep magma plumbing system. *Geophysical research letters*, **29**(9).

Zhang, C., Li, L., Yuan, Z., Xu, X., Song, Z. and Zhang, Y. R. (2020). Mechanical properties of siderite and hematite from dft calculation. *Minerals Engineering*, **146**, p. 106107.

Zhang, S., Yang, F., Xu, D. and Wang, Y. (2014). Seismic wave simulation by velocity–stress wave equations in two-phase anisotropic media. *Journal of Geophysics and Engineering*, **11**(1), p. 015008.

Appendix A

Appendix A - Using geodetic technique for source inversion

VLP signals close the gap between short-period seismology and geodesy, we use a method developed for geodetic observational data (e.g. GNSS/InSAR), namely the Geodetic Bayesian Inversion Software (GBIS, Bagnardi and Hooper, 2018), to invert our seismic data. This way, employing several different models like a point source (Mogi, 1958) or a dipping dike with uniform opening (Okada, 1985), the source volume change can be estimated and the posterior probability distribution of the different source parameters can be obtained. As our displacement data we use the maximum amplitudes of the restituted or modelled step functions (Figure A.1). For our example, we assume a Mogi point source and calculate a volume change of $(1.33 \pm 0.15) \times 10^4$ m^3 for a source at depth 120 ± 30 m (Figure A.2).

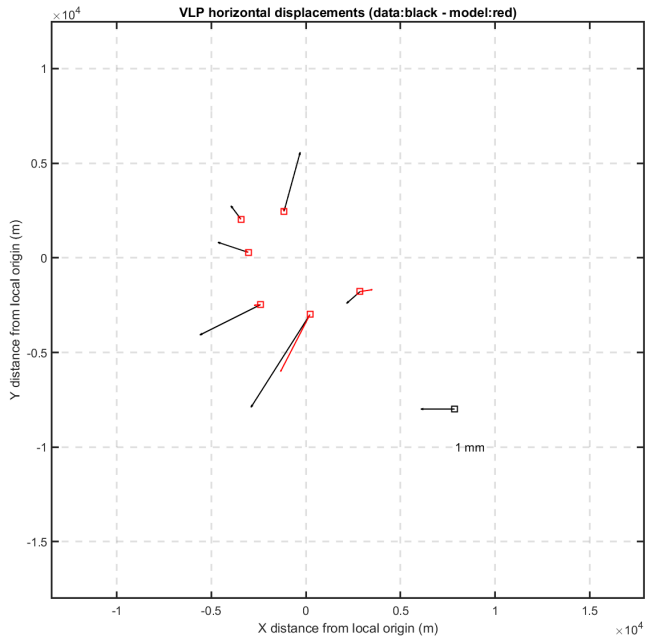

Figure A.1. Horizontal displacements of the VLP signal (black) and horizontal displacements assuming Mogi model (red).

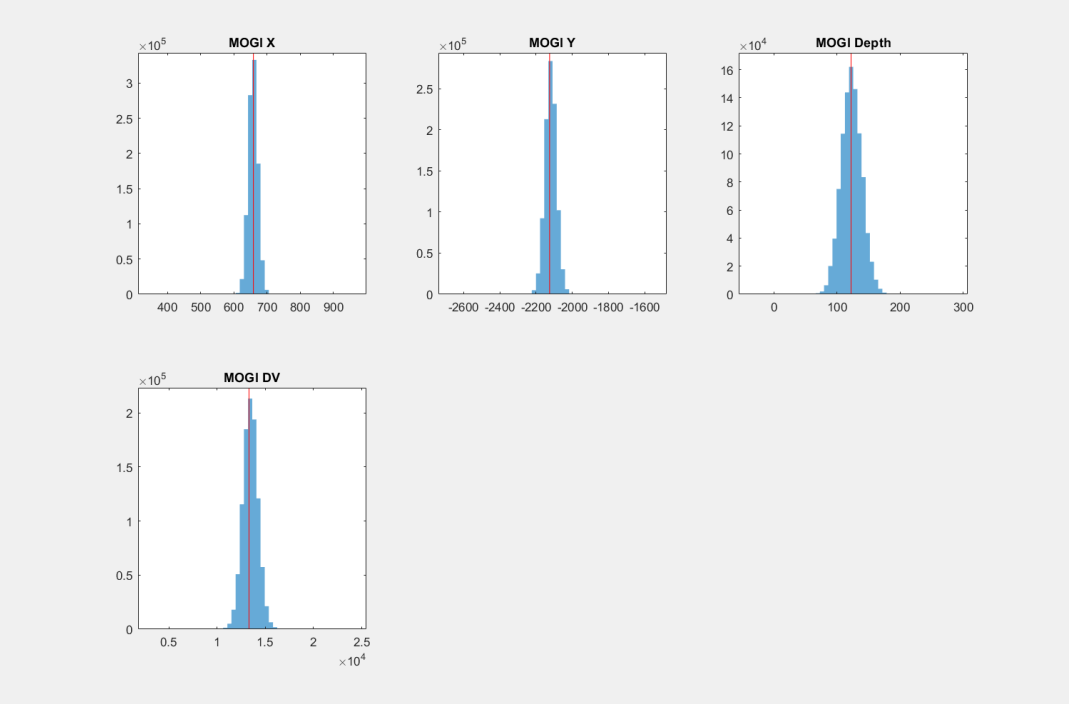

Figure A.2. Posterior probability distributions for the location and the source volume change assuming a Mogi model. The x-direction (east) and y-direction (north) of the source represent the offset in meters relative to the summit of the volcano (positive in east and north directions). Red line indicates the optimal value.

Appendix B

Appendix B - COMSOL set-up for poroelastic wave propagation modelling

The COMSOL general form PDE interface requires the equations to be written in the form of:

$$e_a \frac{\partial^2 \boldsymbol{u}}{\partial t^2} + d_a \frac{\partial \boldsymbol{u}}{\partial t} + \nabla \cdot \Gamma = f, \tag{B.1}$$

where $\boldsymbol{u}$ is a vector with our solid and fluid displacements, e_a is mass coefficient, d_a is damping coefficient and $\nabla \cdot \Gamma$ is the conservative flux. Equation 4.42 shows the expression for the four particle displacement components (u_x, u_y, U_x, U_y):

$$\begin{aligned}
&\frac{\partial^2 u_x}{\partial t^2} + b\left(D_{22} + D_{12}\right)\left(\frac{\partial u_x}{\partial t} - \frac{\partial U_x}{\partial t}\right) - D_{22}\left(\frac{\partial \sigma_{xx}}{\partial x} + \frac{\partial \sigma_{xy}}{\partial y}\right) + D_{12}\frac{\partial s}{\partial x} = 0 \\
&\frac{\partial^2 u_y}{\partial t^2} + b\left(D_{22} + D_{12}\right)\left(\frac{\partial u_x}{\partial t} - \frac{\partial U_x}{\partial t}\right) - D_{22}\left(\frac{\partial \sigma_{xy}}{\partial x} + \frac{\partial \sigma_{yy}}{\partial y}\right) + D_{12}\frac{\partial s}{\partial x} = 0 \\
&\frac{\partial^2 U_x}{\partial t^2} - b\left(D_{11} + D_{12}\right)\left(\frac{\partial u_x}{\partial t} - \frac{\partial U_x}{\partial t}\right) + D_{12}\left(\frac{\partial \sigma_{xx}}{\partial x} + \frac{\partial \sigma_{xy}}{\partial y}\right) - D_{11}\frac{\partial s}{\partial x} = 0 \\
&\frac{\partial^2 U_y}{\partial t^2} - \underbrace{b\left(D_{11} + D_{12}\right)}_{d_a}\left(\frac{\partial u_y}{\partial t} - \frac{\partial U_y}{\partial t}\right) + \underbrace{D_{12}\left(\frac{\partial \sigma_{xy}}{\partial x} + \frac{\partial \sigma_{yy}}{\partial y}\right) - D_{11}\frac{\partial s}{\partial x}}_{\nabla \cdot \Gamma} = 0.
\end{aligned} \tag{B.2}$$

Figure B.1 shows how I set-up these equations in the COMSOL interface.

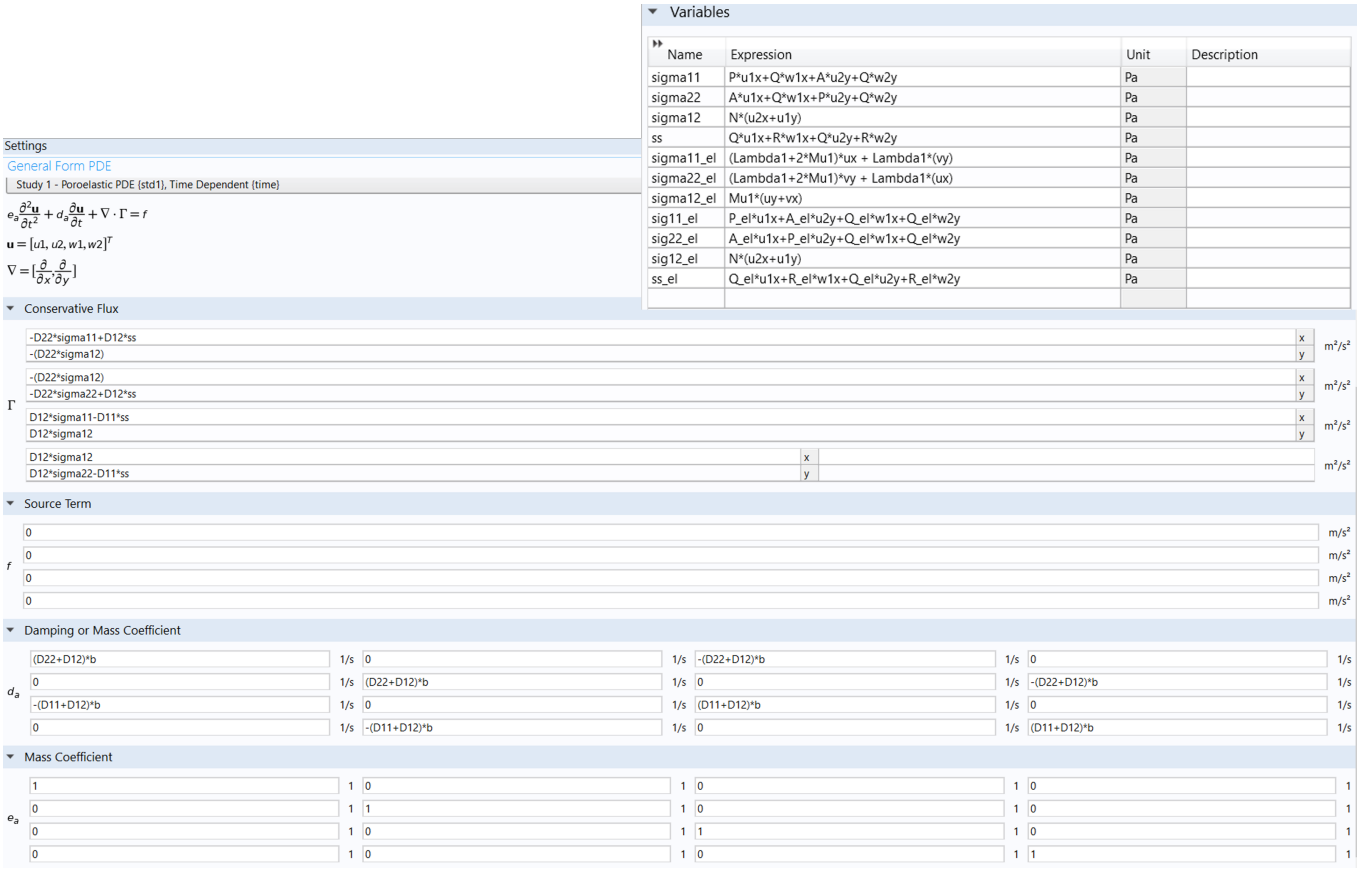

Variables

Name	Expression	Unit	Description
sigma11	P*u1x+Q*w1x+A*u2y+Q*w2y	Pa	
sigma22	A*u1x+Q*w1x+P*u2y+Q*w2y	Pa	
sigma12	N*(u2x+u1y)	Pa	
ss	Q*u1x+R*w1x+Q*u2y+R*w2y	Pa	
sigma11_el	(Lambda1+2*Mu1)*ux + Lambda1*(vy)	Pa	
sigma22_el	(Lambda1+2*Mu1)*vy + Lambda1*(ux)	Pa	
sigma12_el	Mu1*(uy+vx)	Pa	
sig11_el	P_el*u1x+A_el*u2y+Q_el*w1x+Q_el*w2y	Pa	
sig22_el	A_el*u1x+P_el*u2y+Q_el*w1x+Q_el*w2y	Pa	
sig12_el	N*(u2x+u1y)	Pa	
ss_el	Q_el*u1x+R_el*w1x+Q_el*u2y+R_el*w2y	Pa	

Settings

General Form PDE

Study 1 - Poroelastic PDE (std1), Time Dependent (time)

$e_a\frac{\partial^2\mathbf{u}}{\partial t^2}+d_a\frac{\partial\mathbf{u}}{\partial t}+\nabla\cdot\Gamma=f$

$\mathbf{u}=[u1,u2,w1,w2]^T$

$\nabla=[\frac{\partial}{\partial x},\frac{\partial}{\partial y}]$

Conservative Flux

Γ

-D22*sigma11+D12*ss	x		m²/s²
-(D22*sigma12)	y		
-(D22*sigma12)	x		m²/s²
-D22*sigma22+D12*ss	y		
D12*sigma11-D11*ss	x		m²/s²
D12*sigma12	y		
D12*sigma12	x		m²/s²
D12*sigma22-D11*ss	y		

Source Term

f

0	m/s²
0	m/s²
0	m/s²
0	m/s²

Damping or Mass Coefficient

d_a

(D22+D12)*b	1/s	0	1/s	-(D22+D12)*b	1/s	0	1/s
0	1/s	(D22+D12)*b	1/s	0	1/s	-(D22+D12)*b	1/s
-(D11+D12)*b	1/s	0	1/s	(D11+D12)*b	1/s	0	1/s
0	1/s	-(D11+D12)*b	1/s	0	1/s	(D11+D12)*b	1/s

Mass Coefficient

e_a

1	1	0	1	0	1	0	1
0	1	1	1	0	1	0	1
0	1	0	1	1	1	0	1
0	1	0	1	0	1	1	1

Figure B.1. COMSOL set-up for poroelastic wave propagation